Effects of Potential Modulations on Optical Gain Properties in InGaN-based Green Laser Diodes

Yoon Seok Kim

2014

Effects of Potential Modulations on Optical Gain Properties in InGaN-based Green Laser Diodes

Table of contents

Chapter 4. Optical Gain Properties of Polar (0001) Green InGaN Laser Diodes

Chapter 5. Carrier Dynamics and Nanoscopic Optical Properties of Semipolar $\{20\bar{2}1\}$ Green InGaN QWs

Chapter 6. Optical Gain Properties of Semipolar $\{20\bar{2}1\}$ Green InGaN Laser Diodes

Preface

In recent times, the demand for green laser diodes (LDs) has increased remarkably due to their use in several applications such as full color display, medical applications, and anti-piracy systems (APS). Up until 2008, it was difficult to fabricate green laser diodes using III-nitrides since their threshold current densities increase significantly due to strain induced piezoelectric polarization and inhomogeneous broadening (σ) by tail states in the InGaN layer. Pure green LDs grown on semipolar $\{20\bar{2}1\}$ GaN substrates were demonstrated by Sumitomo electric industry for the first time in 2009. This was followed by the fabrication of 515 nm green LDs grown on polar (0001) planes by Nichia Corporation. Then, several groups with slightly varying approaches succeeded in developing green LDs on the polar (0001). The success of green LDs based on the semipolar substrates is due to the reduced internal electric fields for their crystal angles. On the other hand, epitaxial improvement played a key role for the (0001) LDs because high internal electric fields are inevitable in the polar (0001) system.

Here we provide a brief summary of this thesis and its structure. In Chapter 2, a theoretical understanding of the physical limitations of III-nitrides light emitters such as internal electric field and inhomogeneity is developed. The chapter also discusses gain formation and the effects of material parameters on the gain. There are several factors contributing to the optical gain, such as dipole transition moment, the square of the overlap integral, effective mass and line width function. The dipole transition moment is of particular importance in semipolar or nonpolar systems due to the anisotropic character of the valence bands. Since the square of the overlap integral is associated with the tilted crystal angle, the semipolar or nonpolar systems benefit from a higher overlap integral. The effective mass, which is related to the density of states (DOS), can be smaller for semipolar/nonpolar systems due to their smaller DOS. This contributes towards population inversion in these systems.

In Chapter 3, nanoscopic PL mapping results of LD structures on the polar (0001) planes are compared with conventional green emitting QWs grown on epitaxially laterally overgrown GaN (ELOG) templates. The green LD structure shows improved in-plane uniformity, such that the wavelength distribution is as small as 2 nm in comparison to the

conventional green QW with distributions larger than 20 nm. Furthermore the intensity distribution in this LD structure is also superior to conventional QWs. Comparing PL temperature dependence and calculation further supports above homogeneity with σ of 25 meV while conventional one reveals 180 meV. As confirmed by carrier recombination lifetime (τ) measured by time resolved PL, the overlap integral of these LD structure is about 2.1 times higher than that of the conventional QWs. From this finding, the In composition and InGaN thickness are evaluated to be 28% and 2.5 nm, respectively. Compared with the conventional QW, a thinner InGaN QW with a higher In composition is used in the current green LDs.

In Chapter 4, results of the optical gain measurements are discussed. The internal loss of the green LD on the polar (0001) plane is estimated to be ~10 cm^{-1}. Owing to the improvement in epitaxy, this is significantly lower than the loss of ~25 cm^{-1} in conventional shorter wavelength LDs. However, even though this LD has low internal loss, its differential mode gain is lower than those of the shorter wavelength LDs. There are two possible reasons for the low differential gain. First is the limited net volume of InGaN well layers; well layers are slightly thinner for better in-plane homogeneity, as revealed in Chap. 3. The second is the difficulty in taking the difference of refractive indices between InGaN guiding and AlGaN cladding layer. This results in a smaller confinement factor for the green LD. However, even though the differential gain is small, the gain shows high linearity with respect to the carrier density. This suggests the suppression of potential inhomogeneity, which has been reported to suppress a gain increase.

In Chapter 5, the results of nanoscopic PL mapping of green LD structure on the semipolar $\{20\bar{2}1\}$ GaN substrates, performed by scanning near field optical microscope (SNOM) is discussed. The spatial resolution is better than 150 nm, and resolution of the fine structures in the active layer of the LD is possible. Different luminescence properties along the $[\bar{1}014]$ and $[\bar{1}2\bar{1}0]$ directions were investigated by the comparison between SNOM-PL mapping and atomic force microscopy (AFM) measurements. More uniform luminescence was confirmed by the SNOM-PL result along $[\bar{1}2\bar{1}0]$. Carrier diffusion length along each orientation was also obtained by comparison between illumination-collection (I-C) and illumination (I) mode measurements. Wavelength differences were analyzed by comparing with AFM images. The spatial variation of the emission wavelength may be attributed to the difference in the In incorporation probability caused by the small difference in the plane

directions. Although such a variation of the emission wavelength exists, the quantified variations, in terms of standard deviation, are as small as 4.2 meV along the $[\bar{1}014]$ and $[\bar{1}2\bar{1}0]$ directions.

In Chapter 6, results of optical gain measurements for semipolar $\{20\bar{2}1\}$ green InGaN LDs are discussed. The internal loss of the green LD on the semipolar $\{20\bar{2}1\}$ plane is estimated to be ~20±5 cm^{-1}, and is comparable to those of conventional shorter wavelength LDs (~25 cm^{-1}). The green LD on the $\{20\bar{2}1\}$ plane shows gain suppression due to the injection current similar to 440 and 470 nm LDs on (0001) plane. However, maximum gains increase linearly when they are plotted as functions of current density. Decrease in the current injection efficiency and recombination lifetime affects the relation between the current and the carrier density. Current injection plays a critical role in both of light emitting diodes (LEDs) and LDs. The results of the comparison between calculation and measured results for electroluminescence (EL) and gain peak are reasonably explained based on the quantum confinement Stark effect (QCSE) caused by the *pn* built-in potential, state filling, and screening of polarization-induced electric fields.

In Chapter 7, summarized detailed summary of the thesis is presented and proposals for future work are discussed.

Chapter 1.

Introduction

1.1 Research background- Historical stories of green laser diodes

Blue light emitting diodes (LEDs) have had a major impact on our daily lives [1]. Especially, light emitters used in displays, mobile devices, etc., have become an integral part of our lives and are the subject of intensive research and development. White LEDs, which have heavily influenced major industries such as general illumination, were realized by combining blue LEDs and yellow phosphorous [2]. Soon after, the same group (Nichia corp.) also developed purple laser diodes (LDs) [3]. We expect that the incandescent lamps currently in use will be gradually replaced by LED-based systems since these have higher efficiency and environmentally friendly.

LEDs based on III-nitrides also have high wall-plug efficiency and can be made to emit any wavelength in the visible spectrum by bandgap engineering of the InGaN material. Therefore, III-nitrides based light emitters are widely used and have superior merits as compared with conventional emitters such as incandescent lamps, InGaAlP based LEDs, and SiC-based LEDs. Further, due to environmental concerns, the use of heavy metals or hazardous materials is limited, and this has increased the demand for III-nitrides based opto-electronic devices.

One of the most important devices based on III-nitrides materials is the LD. Diode type lasers have many merits such as high WPE and relatively simple system as compared with other lasers. Until recently, the wavelength of LDs was restricted in infrared to 630 nm, but the use of III-nitrides has allowed for wavelength in the near UV spectral region (370 nm). Although several industrial applications require lasers, conventional lasers with their complex physical process and technical issues result in large structures, which are difficult to integrate.

LDs provide a small sized alternative for industries such as ‘blu-ray’, optical pick-up, and communications industry.

By 2008, LDs based on III-nitrides, emitting in the range 370 to 490 nm had been developed [4]. However, to increase their wavelengths, the In composition in InGaN active layer needs to be increased. This leads to an increase in the threshold current density resulting in the deterioration of the performance of LD. The next section provides a detailed explanation of the issues that hinder the development of longer wavelength LDs. However, as mentioned before the wavelengths of these LDs have vacant spots. This is known as ‘green-gap’ problem. Many research groups, including leading companies, are working on solving this problem.

Visible LDs are of great interest since they are useful in several applications such as full color display, visual communications, military applications, and general illumination. Further, LDs may surpass our expectations, and find many other applications in the future. Polar (0001) LDs with a performance of 50 mW at a wavelength of 520-532 nm, have become available in the market. [5]

1.2 Research background- Physical obstacles forward green laser diodes

Nitrides based LDs emitting 400 nm are easily fabricated as the In composition is low. However, as the In composition in the InGaN active layer increases, undesired phenomena such as increase of internal electric field along the growth direction (c-axis) and inhomogeneity of InGaN layer occur. Most LEDs and LDs are fabricated on the (0001) plane called the c-plane. In this crystal orientation, piezoelectric polarization along the growth direction is generated by the strain originating from lattice mismatch between InGaN and GaN in the multiple quantum well (QW) layers [10, 11]. A recent approach used in fabricating green LDs is to avoid the above effects by using semi- or non-polar plane substrates [12-14]. However, these GaN substrates are expensive and not commercially viable. Therefore, the optimization of conventional c-plane fabrication is preferred for manufacturing green LDs, and these two different approaches are now in competition.

Another physical obstacle plaguing the fabrication of green LDs is the in-plane inhomogeneity caused by the immiscibility gap between InN and GaN [13]. This inhomogeneity leads to carrier localization in the InGaN layer. This effect is severe in longer

wavelength LDs, since longer wavelengths require an In composition larger than 30 % in the InGaN layers. Recent reports on green LDs indicate that the improvement of this in-plane inhomogeneity plays a major role in their development [14].

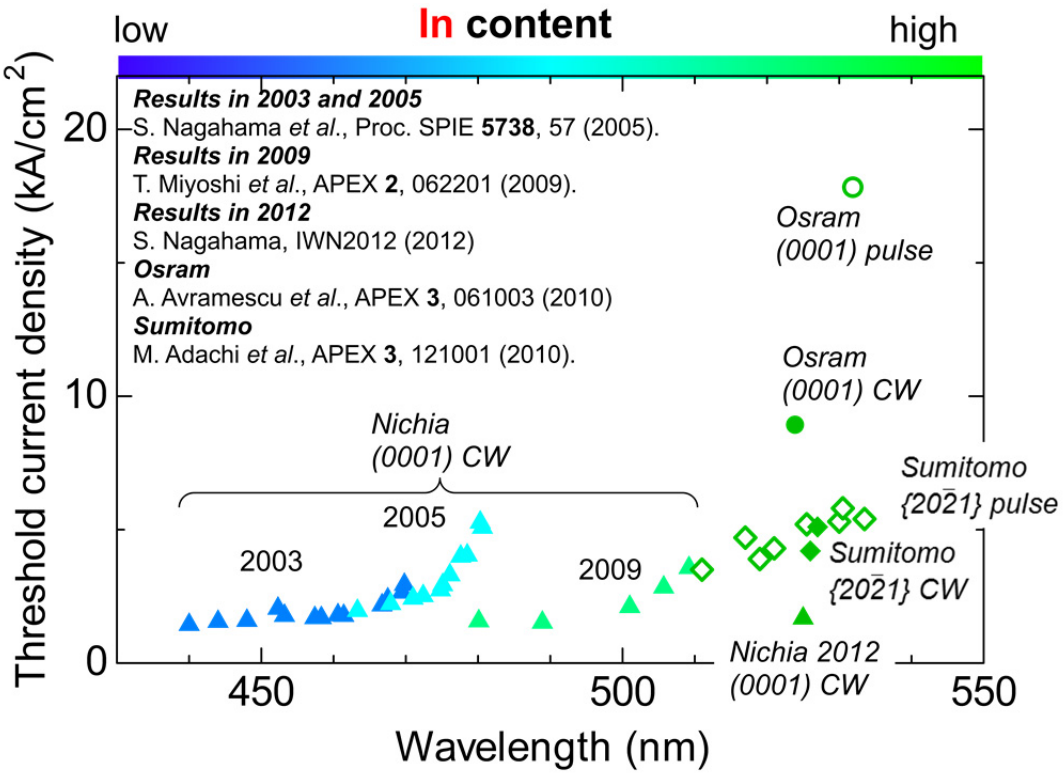

Figure 1.1 Lasing wavelength dependence of threshold current density of III-nitrides LDs.

Threshold current densities with respect to the lasing wavelength are plotted in Fig. 1.1. Until 2008, it seemed very difficult to fabricate LDs beyond 490 nm [4]. However in 2009, Sumitomo electric demonstrated the first pure green LD on the {20$\bar{2}$1} semipolar GaN substrate [6] and this was followed by a 515 nm LD on the (0001) plane by Nichia Corporation [7]. The former LD on the semipolar plane had a low internal electric field and good homogeneity, and latter was assessed by its excellent homogeneity owing to advanced epitaxial growth. Some companies have released green LDs but their performance needs improvement.

1.3 Construction of this thesis

The objective of this thesis is optical characterization and analysis of green LDs fabricated on (0001) polar plane and $\{20\bar{2}1\}$ semipolar plane. The contents of the thesis are illustrated in the flow-chart of Fig. 1.2.

Chapter 2 provides the theoretical background on the optical gain and factors that can influence it.

Then, Chapter 3 discusses carrier dynamics and nanoscopic optical properties of polar (0001) green InGaN QWs. The experimental procedure and analysis of the inhomogeneous broadenings are discussed in detail.

Chapter 4 discusses optical gain properties of polar (0001) green InGaN LDs.

Chapter 5 discusses the carrier dynamics and nanoscopic optical properties of semipolar $\{20\bar{2}1\}$ green InGaN QWs. Then Chapter 6 presents experimental results on the green LDs fabricated on the $\{20\bar{2}1\}$ semipolar plane.

Chapter 7 summarizes all the results and discusses future prospects for green LDs.

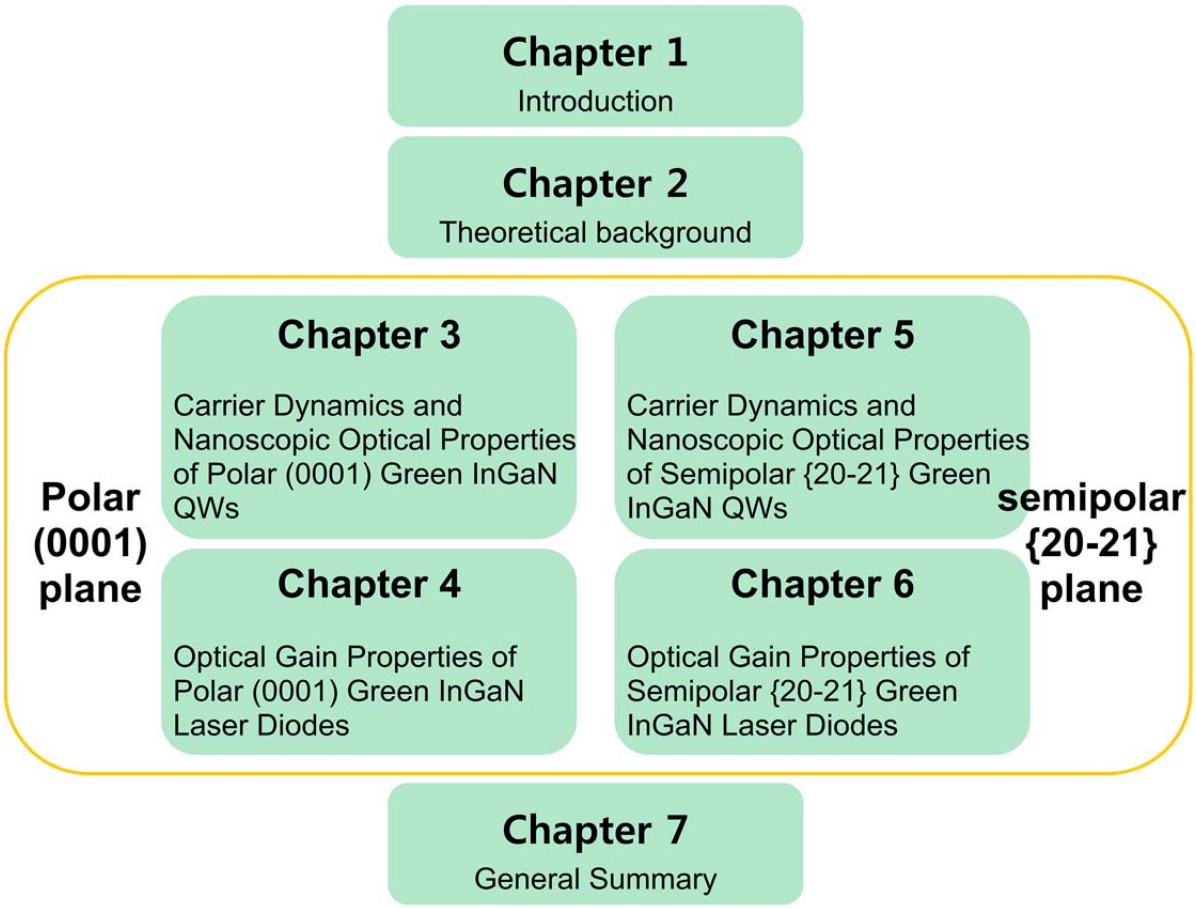

Figure 1.2 Flow chart of doctoral thesis.

References

1) S. Nakamura, M. Senoh, and T. Mukai, *Appl. Phys. Lett.* **62**, 2390 (1993).

2) S. Nakamura, S. Pearton, and G. Fasol, The Blue Laser Diode, 2nd ed. (Springer-Verlag, Heidelberg, 2000).

3) S. Nakamura, M. S. Nagahama, N. Iwasa, T. Yamada, T. Matsushita, H. Kiyoku and Y. Sugimoto, *Jpn. J. Appl. Phys.* **35**, L74 (1996).

4) S. Nagahama, Y. Sugimoto, T. Kozaki, and T. Mukai, *Proceeding of SPIE*, **5738**, 57 (2005).

5) OSRAM 510nm 515nm 520nm 532nm 30mw Green Laser Diode LD PL515 TO38 3.8mm New, http://www.ebay.com/itm/OSRAM-510nm-515nm-520nm-532nm-30mw-Green-Laser-Diode-LD-PL515-TO38-3-8mm-New-/111073607448.

6) Y. Enya, Y. Yoshizumi, T. Kyono, K. Akita, M. Ueno, M. Adachi, T. Sumitomo, S. Tokuyama, T. Ikegami, K. Katayama, and T. Nakamura, *Appl. Phys. Exp.* **2**, 082101 (2009).

7) T. Miyoshi, S. Masui, T. Okada, T. Yanamoto, T. Kozaki, S. Nagahama, and T. Mukai, *Appl. Phys. Exp.* **2**, 062201 (2009).

8) A. Avramescu, T. Lermer, J. Muller, C. Eichler, G. Bruederl, M. Sabathil, S. Lutgen, and U. Strauss, *Appl. Phys. Exp.* **3**, 061003 (2010).

9) M. Adachi, Y. Yoshizumi, Y. Enya, T. Kyono, T. Sumitomo, S. Tokuyama, S. Takagi, K. Sumiyoshi, N. Saga, T. Ikegami, M. Ueno, K. Katayama, and T. Nakamura, *Appl. Phys. Exp.* **3**, 12001 (2010).

10) T. Takeuchi, H. Amano, and I. Akasaki, *Jpn. J. Appl. Phys.* **39**, 413 (2000).

11) S. H. Park and S L. Chuang, *Phys. Rev. B* **59**, 4725 (1999).

12) T. Melo, Y-L Hu, C. Weisbuch, M. C. Schmidt, A. David, B. Ellis, C. Poblenz, Y. –D. Lin, M. R. Krames, and J. W. Raring, *Semicond. Sci. Technol.* **27**, 024015 (2012).

13) D. Sizov, R. Bhat, K. Song, D. Allen, B. Paddock, S. Coleman, L. C. Hughes, and C. Zah, *Appl. Phys. Exp.* 4, 102103 (2011).

14) K. Okamoto, J. Kashiwagi, T. Tanaka, and M. Kubota, *Appl. Phys. Lett.* **94**, 071105 (2009).

15) I. Ho and G. B. Stringfellow, *Appl. Phys. Lett.* **69**, 2701 (1996).

16) A. Avramescu, T. Lermer, J. Muller, S. Tautz, D. Queren, S. Lutgen, and U. Strauss, *Appl. Phys. Lett.* **95**, 071103 (2009).

Chapter 2.

Theoretical Background and Literature Survey

2.1 Potential modulations

As discussed in Chapter 1, light emitters based on III-nitrides suffer from large internal electric fields and inhomogeneous broadening caused by tail states. Before discussing properties of the InGaN layer, it is important to define and understand potential modulations that influence the InGaN QW. Two phenomena are the major contributors and are referred to as potential modulations in this study, as shown in Fig. 2.1. The first contribution is from exciton/carrier localization in the InGaN layers due to fluctuation of the In composition in the lateral direction. This fluctuation is caused by the immiscibility between GaN and InN. Sometimes this in-plane modulation makes the device efficient by exciton localization in low carrier density region, but it also deteriorates the device performance such as spectral broadening. The other contribution is from the internal electric fields caused by piezoelectric polarization along the growth direction, as illustrated in Fig. 2.1.

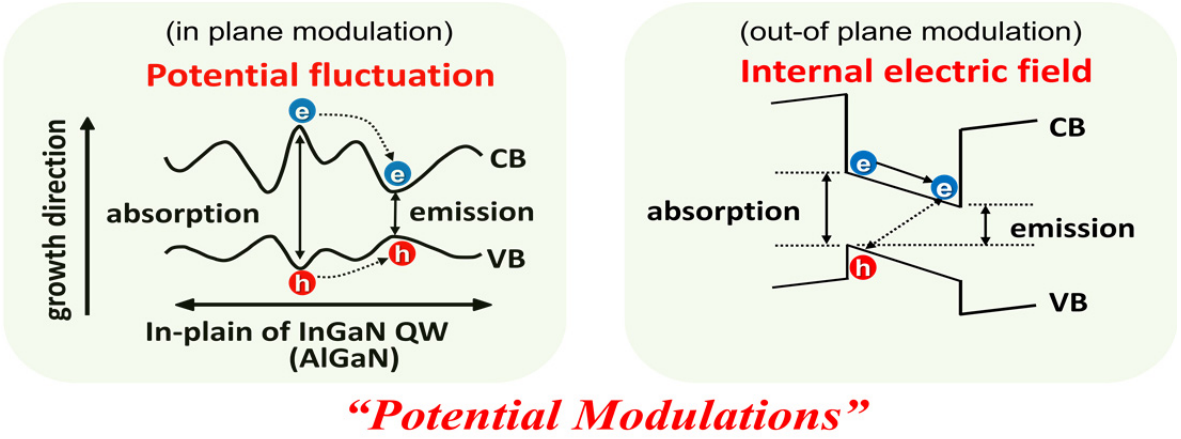

Figure 2.1 Definitions of potential modulations.

2.1.1 Potential fluctuation: in-plane modulation

Numerous efforts have been made to understand the potential fluctuations in III-nitrides. Inhomogeneous broadening of InGaN caused by carrier/exciton localization is of great interest. This potential fluctuation occurs naturally due to the non-uniform formation of InGaN layer, which causes carriers to preferentially flow towards lower potential energy regions called localization centers. Spatial localization of carriers restrains the mobility in the in-plane direction of the QW. This, in turn, either interferes with the capturing of the carriers at non-radiative recombination centers [1, 2], or results in the reduction of recombination probability by decrease of effective area [3]. The former effect increases the internal quantum efficiency in low carrier density regions, as it is mainly governed by localized carriers. This explains the high internal quantum efficiency (IQE) achieved even in III-nitrides systems that have a threading dislocation density of greater than $10^8/cm^2$.

To express the potential fluctuation mathematically, we assume that it follows a Gaussian distribution with standard deviation σ,

$$G(E,\sigma) = \frac{1}{\sqrt{2\pi}\sigma} \exp\left\{ \frac{(E - E_{g0})^2}{2\sigma^2} \right\}, \tag{2.1}$$

where E_{g0} is the average bandgap.

To study the optical properties of the system, we need to calculate the density of states (DOS, ρ). Since the potential fluctuation is given by Eq. (2.1), we can determine modified DOS ρ' by convoluting the DOS ρ with the Gaussian distribution *G*. The DOS ρ is a step function for a QW. This gives

$$\rho'(E) = \int_{-\infty}^{+\infty} dE' \, \rho(E') G(E - E', \sigma), \tag{2.2}$$

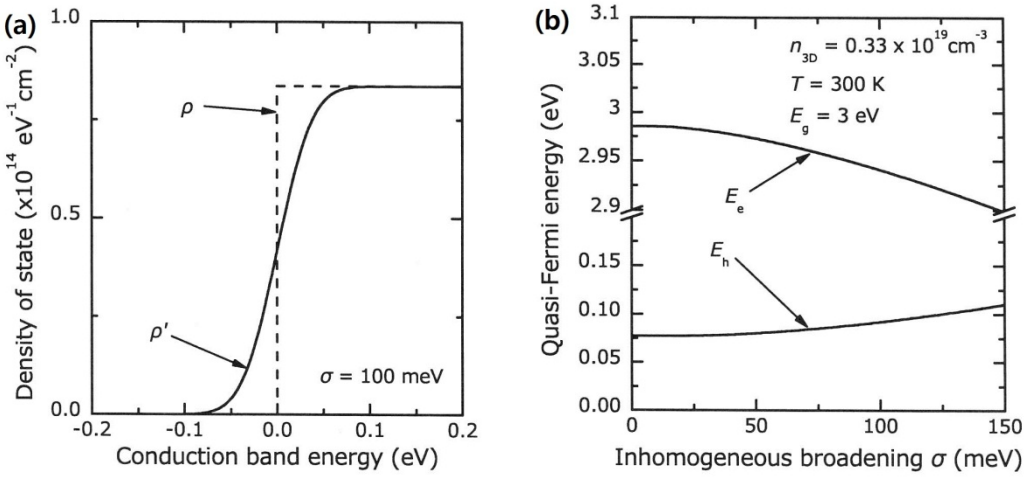

Figure 2.2 (a) DOS with inhomogeneously broadened tail states and (b) variation of quasi-Fermi levels due to inhomogeneous broadening. (reprinted from Ref. [10].)

Figure 2.2(a) displays plots of the functions ρ and inhomogeneously broadened DOS ρ' with respect to the conduction band energy. Furthermore, the energy distribution of the carriers $f(E)$, is a function of E_e and E_h, and follows a Fermi-Dirac distribution governed by the carrier temperature T and Fermi energy. The energy distributions for the electrons and holes are given by the following equations:

$$f_c(\omega) = f_e(\omega) = (1+\exp[\beta(\hbar\omega - E_e)])^{-1}, \tag{2.3}$$

$$1 - f_v = f_h(\omega) = (1+\exp[\beta(\hbar\omega - E_h)])^{-1}, \tag{2.4}$$

where $\beta = (k_B T)^{-1}$, k_B is the Boltzmann constant, E_e is the conduction band energy, and E_h is the valence band energy. Figure 2.2(b) shows the change in the quasi-Fermi levels with respect to the inhomogeneous broadening.

2.1.2 Internal electric field: out-of plane modulation

The other important physics in III-nitrides is piezoelectric polarization. Polarized charges are created in the strained hetero-interfacial area by piezoelectric polarization since nitrides are strongly piezoelectric crystals. There is also some contribution from spontaneous polarization. Therefore, quantum confinement Stark effect (QCSE) typically occurs along the growth direction in hetero-QW structures [4]. In light emitters based on interband transition, QCSE is an undesirable effect. In the following subsections, spontaneous and piezoelectric polarizations are discussed in detail.

2.1.2.1 Spontaneous polarization, P^{sp}

Spontaneous polarization indicates natural polarization, which is not induced by any strain. We assume a simple model for spontaneous polarization, as shown in Fig. 2.3(a). The dipole moments are compensated by each other in this configuration where the N atoms are positioned at each edge of a regular tetrahedron surrounding the Ga atom. Therefore, in this configuration no piezoelectric field is generated. However, in reality, the atom position is displaced from the ideal tetrahedron due to the iconicity. This displacement breaks the symmetry and causes the spontaneous polarization.

The spontaneous polarization directs along the [0001] direction. Note, spontaneous polarization is not dependent on the nature of the atomic bonding and is only influenced by the atomic configuration.

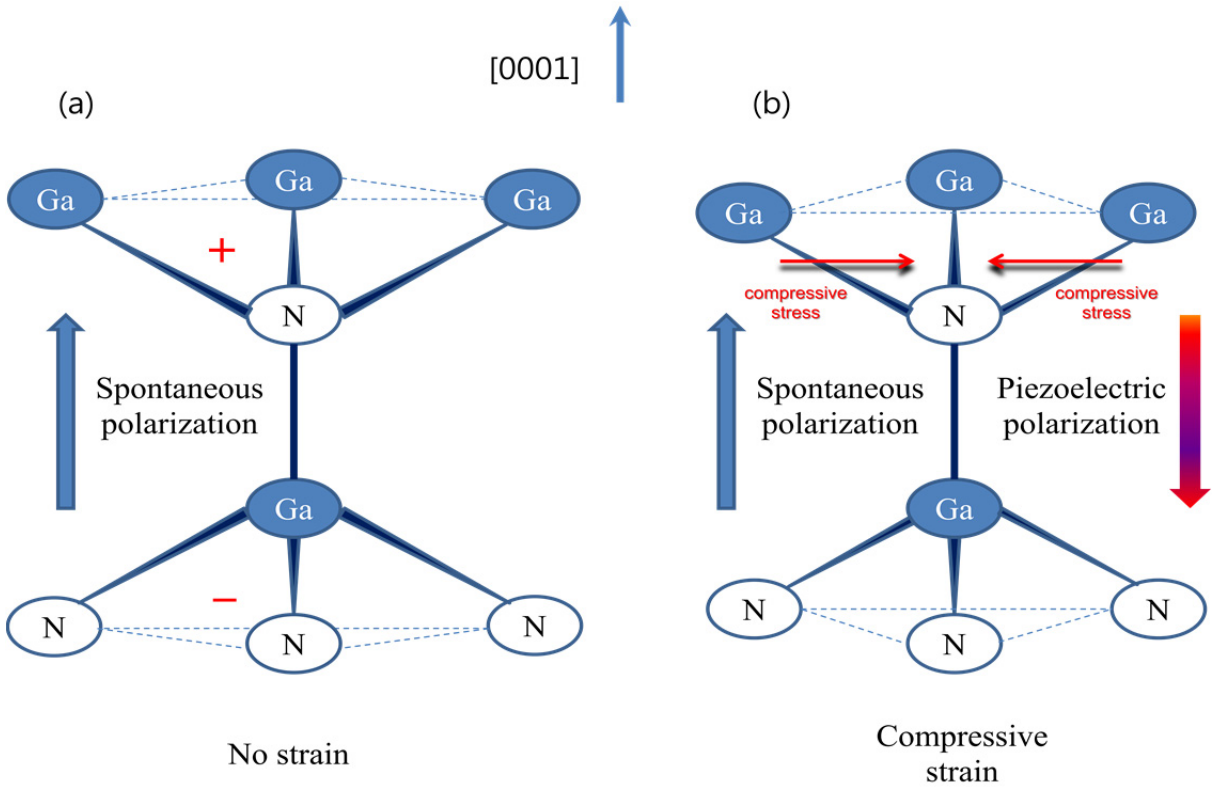

Figure 2.3 (a) Spontaneous and (b) piezoelectric polarizations in crystal.

2.1.2.2 Piezoelectric polarization, P^{pz}

The internal electric field in the InGaN system is the sum of spontaneous and piezoelectric fields. However, the piezoelectric gives the dominant contribution with increase in In composition. Piezoelectric polarization is strongly related to the strain in the active layer. Most InGaN base devices consist of a hetero-structure. Such hetero-systems are inevitably subject to strain because of the mismatch in lattice parameters between the active and surrounding layers. The dipole moments do not compensate each other when a strain, caused by the lattice mismatch between GaN and InGaN, exists. This leads to piezoelectric polarization, as shown in Fig. 2.3(b). Electrons and holes are separated in space by the electric field induced by the polarization effect, and are likely to move towards the opposite barrier sides. Consequently the overlap integral of the wavefunctions of electrons and holes

becomes smaller resulting in a reduction in radiative recombination probability. This phenomenon plays major role in deterioration of IQE of LEDs and LDs.

Strain can be expressed by the degenerated tensor,

$$. \quad \varepsilon_{ij} = (\varepsilon_{xx}\varepsilon_{yy}\varepsilon_{zz}2\varepsilon_{yz}2\varepsilon_{zx}2\varepsilon_{xy})^{T}. \tag{2.5}$$

To define the orientation of materials, the orthogonal coordinates are defined and are represented as lower letters. z represents the direction parallel to the growth direction and x, y are orthogonal to each other and lie in the basal plane.

General Hooke's law relates the piezoelectric polarization P^{pz} to the strain ε_{ij} through piezoelectric tensor e_{ij} or d_{ij}. The relation between strain ε_{ij} and piezoelectric polarization P^{pz} can be simplified by using the elasticity constants c_{ij} with respect to a wurztite structure [4, 5];

$$P^{pz} = \begin{pmatrix} 0 & 0 & 0 & 0 & e_{15} & 0 \\ 0 & 0 & 0 & e_{15} & 0 & 0 \\ e_{31} & e_{31} & e_{33} & 0 & 0 & 0 \end{pmatrix} \begin{pmatrix} \varepsilon_{xx} \\ \varepsilon_{yy} \\ \varepsilon_{zz} \\ 2\varepsilon_{yz} \\ 2\varepsilon_{zx} \\ 2\varepsilon_{xy} \end{pmatrix} \tag{2.6}$$

$$= \begin{pmatrix} 0 & 0 & 0 & 0 & d_{15} & 0 \\ 0 & 0 & 0 & d_{15} & 0 & 0 \\ d_{31} & d_{31} & d_{33} & 0 & 0 & 0 \end{pmatrix} \begin{pmatrix} c_{11} & c_{12} & c_{13} & 0 & 0 & 0 \\ c_{12} & c_{12} & c_{13} & 0 & 0 & 0 \\ c_{13} & c_{13} & c_{33} & 0 & 0 & 0 \\ 0 & 0 & 0 & c_{44} & 0 & 0 \\ 0 & 0 & 0 & 0 & c_{44} & 0 \\ 0 & 0 & 0 & 0 & 0 & c_{66} \end{pmatrix} \begin{pmatrix} \varepsilon_{xx} \\ \varepsilon_{yy} \\ \varepsilon_{zz} \\ 2\varepsilon_{yz} \\ 2\varepsilon_{zx} \\ 2\varepsilon_{xy} \end{pmatrix}. \tag{2.7}$$

Consequently piezoelectric polarization for each orientation is given by

$$P_x^{pz} = 2d_{15}c_{44}\varepsilon_{xz}, \tag{2.8}$$

$$P_y^{pz} = 2d_{15}c_{44}\varepsilon_{yz}, (P_y^{pz} = 0 \text{ when, } \varepsilon_{yz} = 0) \tag{2.9}$$

$$P_z^{pz} = \{d_{31}(c_{11} + c_{12}) + d_{33}c_{13}\}(\varepsilon_{xx} + \varepsilon_{yy}) + (2d_{31}c_{13} + d_{33}c_{33})\varepsilon_{zz}. \tag{2.10}$$

Here, we consider P_z^{pz} to be the component along the growth orientation. The internal electric fields $E_{\text{int}}^{well}, E_{\text{int}}^{bar}$ are given by summation of P^{pz} and P^{sp}.

$$E_{\text{int}}^{well} = \frac{P_z^{sp,bar} + P_z^{pz,bar} - P_z^{sp,well} - P_z^{pz,well}}{\varepsilon_{well} + \varepsilon_{bar}(L_{well} / L_{bar})}, \tag{2.11}$$

$$E_{\text{int}}^{bar} = -\frac{L_{well}}{L_{bar}} E_{\text{int}}^{well}, \tag{2.12}$$

where the subscript/superscript "bar" indicates barrier, and ε_i (i = *well* or *bar*) is the dielectric constant. The internal electric fields in single QW (SQW) are

$$L_{\text{bar}} = \infty, P_z^{pz,bar} = 0 \text{ in SQW} \tag{2.13}$$

$$E_{\text{int}}^{well} = \frac{E_z^{sp,bar} - P_z^{sp,well} - p_z^{pz,well}}{\varepsilon_{well}}, \tag{2.14}$$

$$E_{\text{int}}^{bar} = 0. \tag{2.15}$$

Particularly when the growth is on the (0001) plane, stress on the (0001) polar plane is 0, and the strain becomes

$$\varepsilon_{zz} = -\frac{2c_{13}}{c_{33}}\varepsilon_{xx} = -\frac{2c_{12}}{c_{33}}\varepsilon_{yy}. \tag{2.16}$$

Thus, there is just one independent variable.

As derived above, the piezoelectric polarization increases linearly with strain. This implies that as the In composition in InGaN well layer increases, the polarization also increases. Consequently, an increased piezoelectric polarization induces higher internal electric field. Note, in such system, the electric field contribution from *pn* built-in or spontaneous polarization is relatively smaller than the contribution from piezoelectric polarization.

2.1.2.3 Crystal angle dependence of internal electric field

In the last section, we derived a mathematical expression for piezoelectric polarization and explained the relationship with the spontaneous polarization and built-in electric field, for the polar (0001) plane. In this section, we will explore these relations for other crystal planes. For this, it is necessary to derive the conversion base matrix in hexagonal system. The crystal angle between a random (*hkil*) plane and (0001) plane, θ, is given by

$$\theta = \arccos \frac{\frac{3a^2}{4c^2} l}{\left\{ \frac{3a^2}{4c^2} \left(h^2 + k^2 + hk + \frac{3a^2}{4c^2} \right) \right\}^{\frac{1}{2}}}, \tag{2.17}$$

where, *a* and *c* are lattice parameters of wurtzite crystal. A representative crystal orientation is shown in Fig. 2.4.

x and *y* correspond to the base axis in the (0001) plane, and *z* is the axis perpendicular to the (0001) plane. We set *x* and *y* as $<11\bar{2}0>$ and $<10\bar{1}0>$, respectively. To derive a general relation for any tilted angle, the following rotation matrix is used to transform the coordinates.

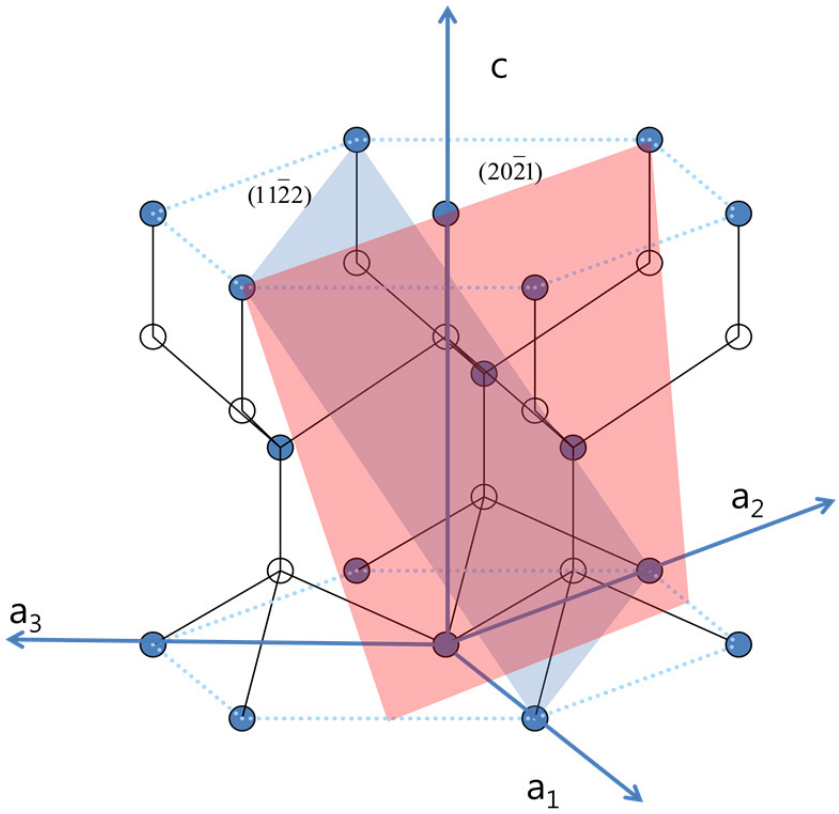

Figure 2.4 Representative crystal planes and axes.

$$U = \begin{pmatrix} \cos\theta\cos\phi & \cos\theta\sin\phi & -\sin\theta \\ -\sin\theta & \cos\phi & 0 \\ \sin\theta\cos\phi & \sin\theta\sin\phi & \cos\theta \end{pmatrix}, \tag{2.18}$$

$$\begin{pmatrix} x' \\ y' \\ z' \end{pmatrix} = U \begin{pmatrix} x \\ y \\ z \end{pmatrix}. \tag{2.19}$$

Here the letters having upper prime x', y', and z' are the new coordinates obtained by applying the rotation matrix U to the original coordinates x, y, and z.

The expression for piezoelectric polarization in the new coordinate *x'*, *y'*, and *z'* can be generalized by multiplying Eqs. (2.6) or (2.7) with the rotation matrix *U*. ϕ is the angle between *y* and *y'*, but we take the *y* axis as the rotational axis. Therefore, *y* always coincides with *y'*, and therefore, ϕ is zero, which provides following expressions:

$$P_{x'}^{pz} = P_x^{pz}\cos\theta - P_z^{pz}\sin\theta, \tag{2.20}$$

$$P_{y'}^{pz} = -P_x^{pz}\sin\theta + P_y, \tag{2.21}$$

$$P_{z'}^{pz} = P_x^{pz}\sin\theta + P_z^{pz}\cos\theta. \tag{2.22}$$

The tilted crystal angle dependence of the piezoelectric polarization and internal electric field are shown in Fig. 2.5 for an In composition of 30 %.

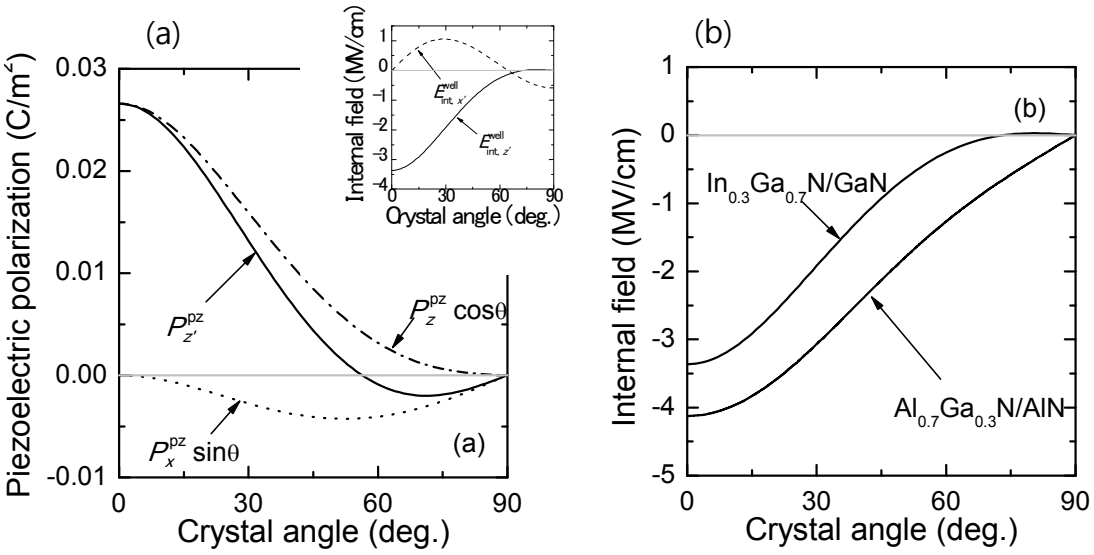

Figure 2.5 (a) Piezoelectric polarization in $In_{0.3}Ga_{0.7}N$/GaN QW, and (b) internal electric field with respect to tilted crystal angle. (reprinted from ref. [10].)

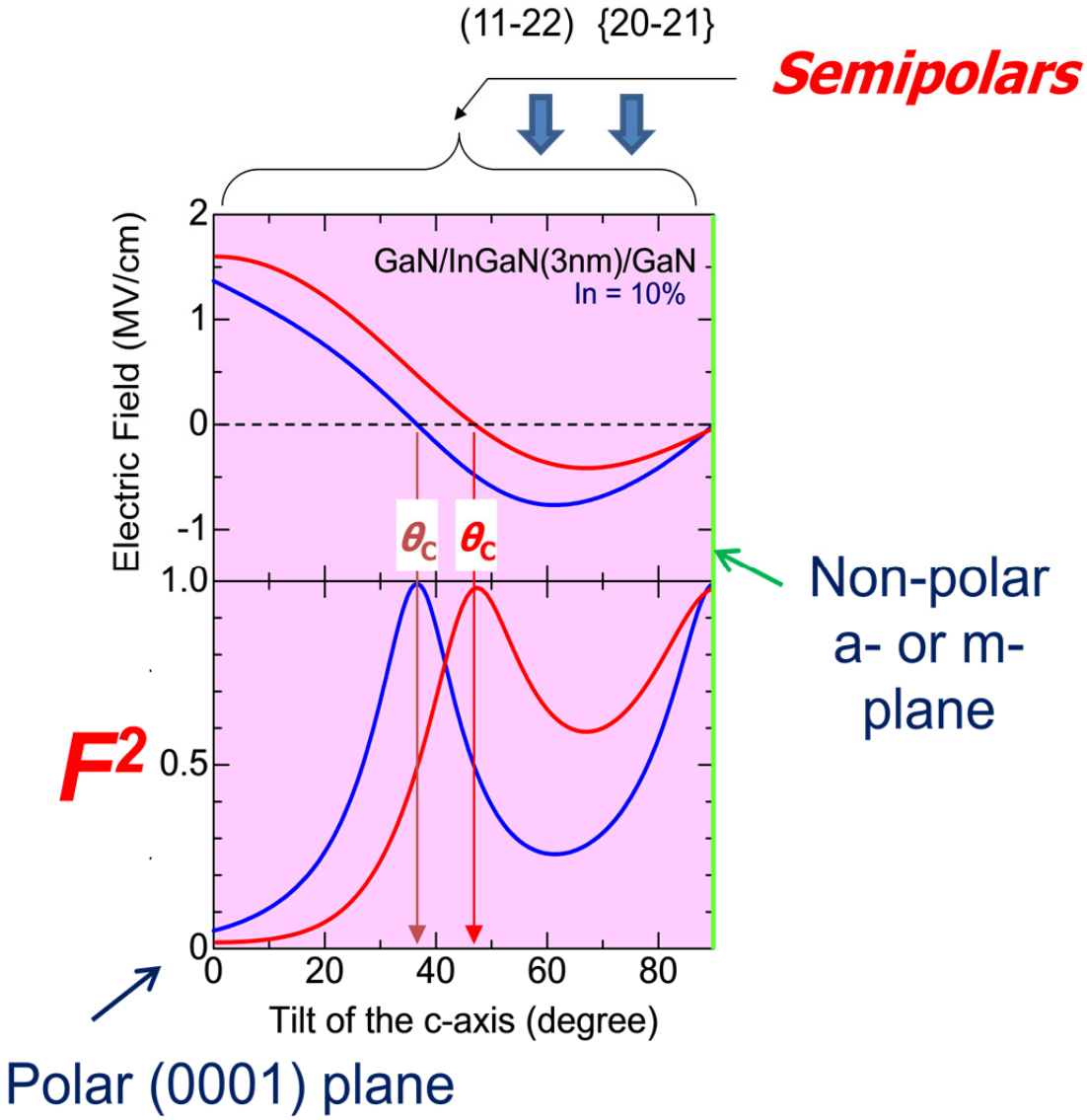

Figure 2.6 Tilt crystal angle dependence of internal electric field and square of overlap integral. In composition is 10 % in InGaN well layer.

It is interesting to note that there are two angles at which the piezoelectric fields and internal electric fields are 0. One is 90° of non-polar plane and the other is a certain angle (dependent on material parameters used for the calculation) known as the semipolar plane. This encourages us to research semipolar-plane based devices. Another important parameter for light emitters is the square of the overlap integral between hole and electron wavefunctions. This is directly related to the recombination probability. Figure 2.6 shows tilted angle dependence of the electric field and the square of the overlap integral in InGaN QW with 10% In composition.

2.2 Optical gain

2.2.1 Formula of gain contributed by material parameters

The optical gain of a laser in a homogeneous system can be expressed as

$$G_{\text{homo}}(\omega) = g_0 \int_0^\infty dk \left|M_{cv}(k)\right|^2 \left\langle \varphi_c \middle| \varphi_v \right\rangle^2 DOS(k)F(k)L(k) \tag{2.23}$$

$$= \frac{C}{\sqrt{2\hbar\omega\pi\gamma_h}} \int_0^\infty dk \left|M_{cv}(k)\right|^2 (f_c + f_v - 1)L(\omega'(k) - \omega), \tag{2.24}$$

where $|M_{cv}(k)^2|$, $|\varphi_c \cdot \varphi_v|$, *DOS(k)F(k)*, and *L(k)* are transition dipole moment, overlap integral between electron and hole wavefunctions, product of density of states and distribution which is related to the effective mass, and homogeneous line width function, respectively. Homogeneous broadening is treated as a constant (25 meV), which is included as a hyperbolic secant function (sech). In this section, those parameters are investigated for the contribution on gain formation. To calculate absolute value of gain the constant *C* is defined as

$$C = \frac{e_0^2}{2\hbar c_0 L_w m_0^2 n_r \varepsilon_0}, \tag{2.25}$$

where, $\hbar$, c_0, e_0, and m_0 is degenerated Plank constant, light velocity in vacuum, electronic charge, and mass. L_w is the thickness of QWs, and n_r is the refractive index. By the modulation of In content in the QWs, peak energy of the gain spectrum can vary dramatically. When inhomogeneous broadening is accounted for by the Gaussian distribution, the mean energy of the distribution is re-defined as average bandgap, E_{g0}. The gain for an inhomogeneous system (G_{inh}) is expressed by convoluting the gain for a homogeneous system with the Gaussian distribution G.

$$G_{inh} = \frac{1}{\sqrt{\pi}\sigma}\int d\omega' G_{\text{homo}}(\omega - \omega')G(E - E'). \tag{2.26}$$

The mode gain (g), which determines the laser characteristics, has the following relation with G_{inh}:

$$g = \Gamma G_{\text{inh}} - \alpha_i(1 - \Gamma), \tag{2.27}$$

where, α_i is internal loss, and Γ is the light confinement factor. Γ is determined by the analysis of light propagation, based on the LD structure. The internal loss of the diodes can be evaluated from the gain spectra obtained experimentally.

2.2.2 In-plane potential modulation

Since the infancy of nitrides research, in-plane potential modulation has been studied extensively as it leads to carrier localization. Early research mainly focused on the internal quantum efficiency, while the optical gain of nitrides laser diodes was not investigated. As in-

plane potential modulation becomes larger, maximum gain decreases around the peak photon energy. Interestingly, the lower energy side of the gain spectra shows gain generation in low carrier density region as shown in Fig. 2.7. Equation (2.26) mathematically represents the influence of inhomogeneous broadening on optical gain. In this work, the effects of inhomogeneous broadenings known as in-plane potential modulation on the luminescent spectra including EL, PL, and gain have been studied extensively. We note that large In content in the InGaN layer causes several severe problems in green LDs such as spectral broadening, and suppression of gain.

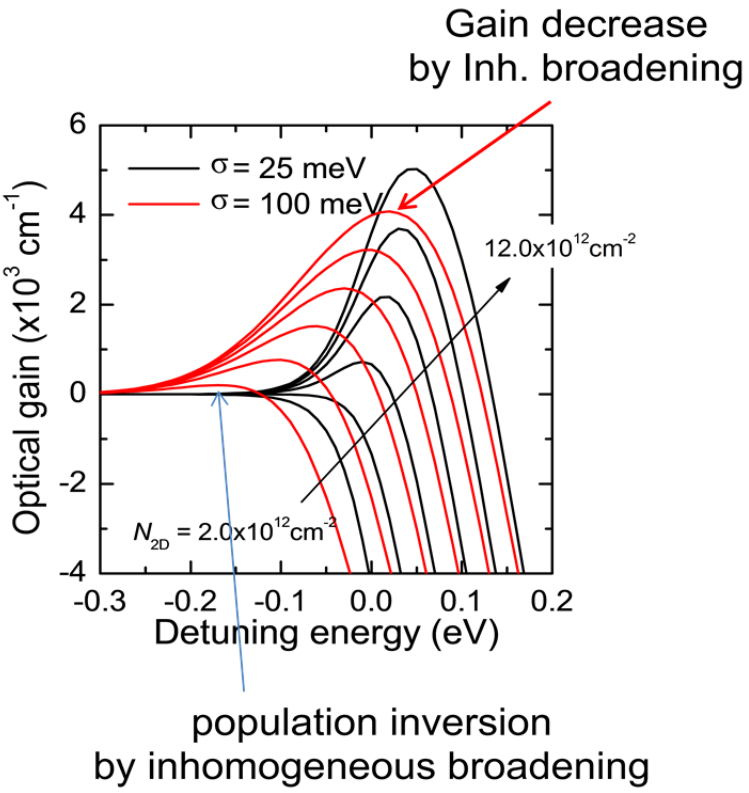

Figure 2.7 Calculation of optical gain spectra with in-plane potential modulation of 25 or 100 meV. (reproduced from Ref. [10].)

2.3 Summary

In this chapter, we defined potential modulation and described the components of the optical gain. To explain in-plane modulation we needed to quantify inhomogeneous broadening. Next, the internal electric field also known as out-of plane modulation was described in terms of spontaneous and piezoelectric polarization. Methods to reduce this internal electric field are the topic of intense research. Amongst these methods, the use of semipolar plane of GaN substrate has been developed. The tilt angle dependency is quantified by applying a rotation matrix on the coordinate system.

There are several terms that influence the optical gain such as transition dipole moment of oscillator, product of density of states and distribution, and line width function. We have explained these affect the optical gain.

References

1) S. Chichibu, T. Azuhata, and S. Nakamura, *Appl. Phys. Lett.* **69**, 4188 (1996).

2) Y. Narukawa, Y. Kawakami, M. Funato, Sz. Fujita, Sg. Fujita, and S. Nakamura, *Appl. Phys. Lett.* **70**, 981 (1997).

3) M. Sugawara, *Phys. Rev. B* **51**, 10743 (1995).

4) T. Takeuchi, S. Sota, M. Katsuragawa, M. Komori, H. Takeuchi, H. Amano, and I. Akasaki, *Jpn. J. Appl. Phys.* **36**, L382 (1997).

5) S. H. Park and S. L. Chuang, *Phys. Rev. B* **59**, 4725 (1999).

6) W. W. Chow and S. W. Koch, Semiconductor-Laser Fundamentals (Springer, Berlin, 1999).

7) B. Witzigmann, V. Laino, M. Luisier, U. T. Schwartz, H. Fischer, G. Feicht, W. Wegscheider, C. Rumbolz, A. Lell, and V. Härle, *IEEE Phot. Tech. Lett.* **18**, 1600 (2006).

8) D. Ahn, S. L. Chuang, and Y. C. Chang, *J. Appl. Phys.* **64**, 4056 (1988).

9) S.H. Park, S. L. Chuang, J. Minch, and D. Ahn, *Semicond. Sci. Technol.* **15**, 1 (2000).

10) K. Kojima, Dissertation of Ph. D, Kyoto University (2008)

Chapter 3.

Carrier Dynamics and Nanoscopic Optical Properties of Polar (0001) Green InGaN QWs

3.1 Introduction

Green LDs based on InGaN QWs are an important technological target, since they are expected to have various applications including laser display [1]. There are two major factors that hamper their practical application; the first concerns the crystal qualities of In-rich InGaN, which are necessary for green emission, and the second is polarization-induced internal electric fields. Both these are related to the large lattice mismatch between InN and GaN. A key factor in circumventing these issues is the crystallographic orientation along which the device structures are fabricated. Semipolar planes such as $(11\bar{2}2)$ [2] and $\{20\bar{2}1\}$ [3] show a promising reduction in polarization effects [4, 5]. Furthermore, the optical anisotropy due to their low crystal symmetry may lower the threshold current density (J_{th}) [6]. Note, that the room temperature (RT) CW operation of pure-green LDs has been realized by InGaN QWs on $\{20\bar{2}1\}$ GaN substrates [7, 8]. On the other hand, effort has been dedicated to improve the quality of the epilayers on the conventional polar (0001) planes, for realizing green LDs [9, 10]. Recently, impressive progress has been reported for (0001) LDs emitting at 525 nm; a J_{th} of 1.68 kA/cm^2, an output power of 1.01 W, and a wall plug efficiency of 14.1 % [11]. Although the semipolar planes seem better suited for green LDs in terms of physics, the conventional polar (0001) plane has vast amounts of accumulated technological resources. Therefore, it is still an open question as to which plane will be commercially feasible.

Optical characterization is indispensable to the recent remarkable progress in InGaN-based LDs. In literature, the gain properties of the (0001) LDs emitting in the near ultra-violet to green spectral range [12-15] and green $\{20\bar{2}1\}$ LDs [16] have been reported. These

previous studies indicate that as the In composition is increased to obtain a longer wavelength range, potential fluctuations become pronounced and cause gain suppression. In this study, we investigate the optical properties of state-of-the-art green LDs fabricated on the (0001) GaN substrates with particular focus on potential fluctuations.

3.2. Experiments

The laser structures with and without doping were grown by metalorganic vapor phase epitaxy on the (0001) GaN substrates. (Except for doping, the structures are identical.) The former (doped) was processed into 800 × 2 μm^2 ridge waveguide LDs, whereas the latter was used to assess fundamental optical properties. Optical characterization for the LDs, including gain properties, is discussed in Chapter 4.

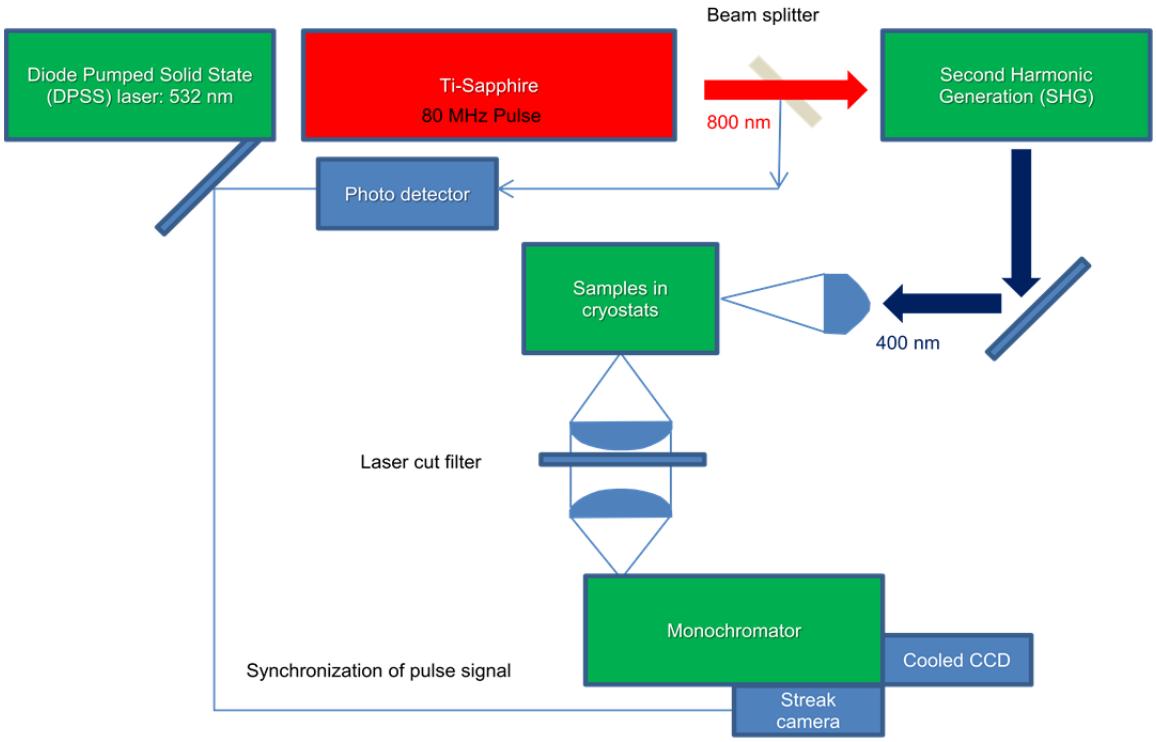

Figure 3.1 Schematic diagram of optical measurement system.

3.2.1 Macroscopic optical measurement system

The excitation source for optical assessment was a frequency doubled Ti-sapphire laser. The Ti-sapphire is excited by an 8 W diode pumped solid state laser that continuously emits 532 nm, and it emits 800 nm at a 2 W output power with a frequency of 80 MHz. To excite InGaN layer, 400 nm is achieved by using second harmonic generation (SHG) with nonlinear crystal optics. We measure the temperature dependence of the luminescence, by loading the sample in a cryostats cooled by the closed cycled compression of He gas. The luminescence is detected by proper convex achromatic lenses to direct the light into a monochromator where a grating disperses the light, and the signal is detected by a charge coupled detector (CCD). For time resolved PL systems, the excitation source is nearly the same, but the luminescence is detected by proper units such as a streak camera, time co-related single photon detector, or EM-photon multiplier tube (PMT). Figure 3.1 illustrates a pico-second pulse width laser system in which the sample temperature is adjusted by closed cycled cryostats.

3.2.2 Nanoscopic optical measurement system

To visualize optical characteristic in the range of a few micrometer, high spatial resolution measurements are necessary. These measurements are restricted by the diffraction limit when using conventional microscopy. The Rayleigh criterion provides a definition of spatial resolution. According to this criterion, we can resolve the spectrum when given a sufficiently small excitation beam size. The spatial resolution is given by

$$\Delta x = 0.61 \times \frac{\lambda}{\text{number of N.A.}}, \tag{3.1}$$

where N.A. is the numerical aperture of objective lens. One of representative ways to resolve the luminescence spatially is confocal micro(nano-)scopic PL measurements. Our set-up at Kyoto University provides about 360 nm spatial resolution when the excitation source

wavelength is 400 nm. This 360 nm resolution is sufficient to assess the local homogeneity distribution of InGaN materials in the green spectral region. The schematic set-up of our confocal microscope PL system is shown in Fig. 3.2. The system is installed on an anti-vibration optical table and in a constant temperature booth to avoid external influences.

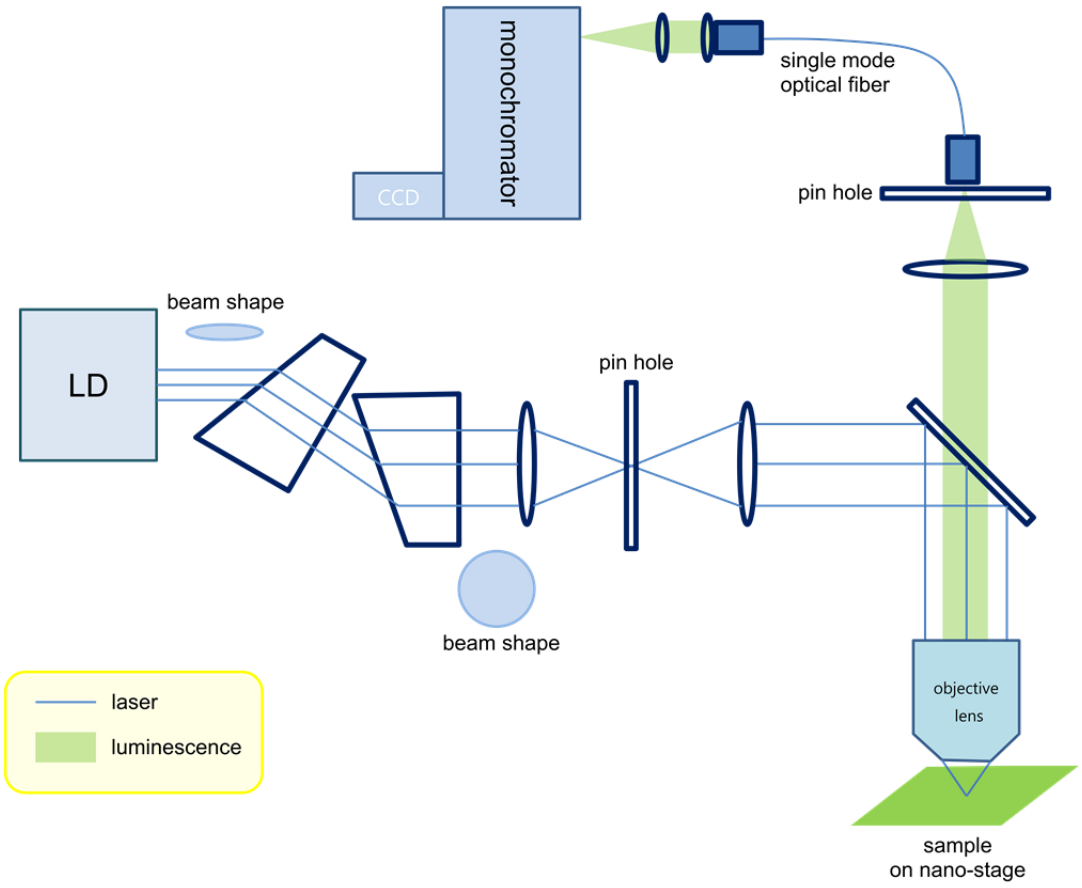

Figure 3.2 Schematic diagram of confocal micro(nano-)scope PL mapping measurement system.

Our set-up uses a 400 nm laser diode as excitation source and an objective lens with a numerical aperture of 0.95. Therefore, theoretically we should obtain ~260 nm resolution from output beam. However, there are several interfering factors such as divergence, and symmetry of the laser beam, which hinder the realization of the theoretical value. The best spatial resolution we obtained was 360 nm, as evaluated by the knife-edge method using atomically cleaved semiconductor substrates. Figure 3.3 shows a schematic of the knife edge method to evaluate spatial resolution.

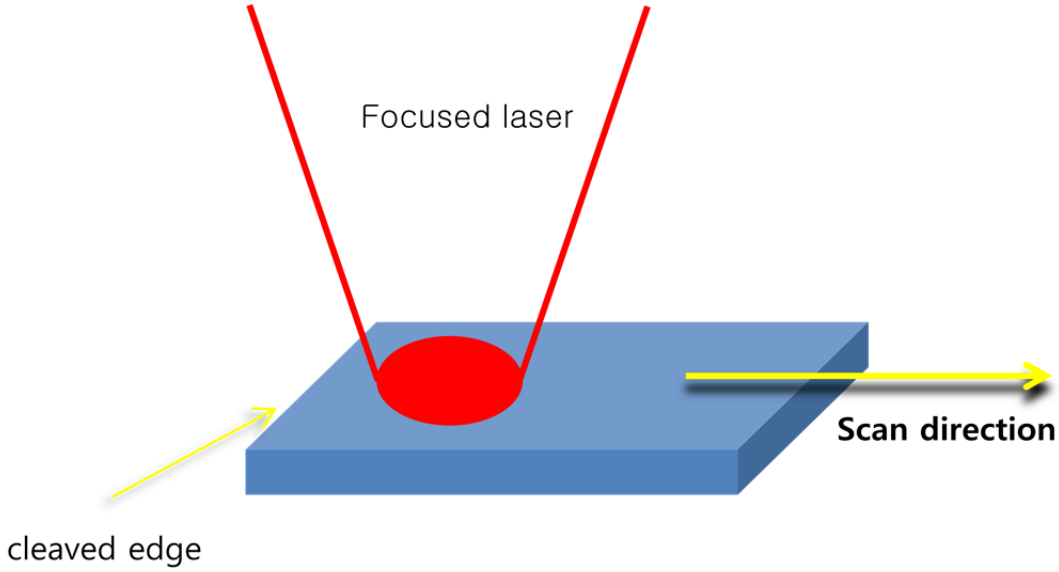

Figure 3.3 Schematic illustration of knife-edge method.

If we assume that the intensity profile of the laser follows a Gaussian distribution, the real position of the full width at half maximum of the intensity corresponds to the spatial resolution of the measurement system. This assumption is illustrated in Fig. 3.4.

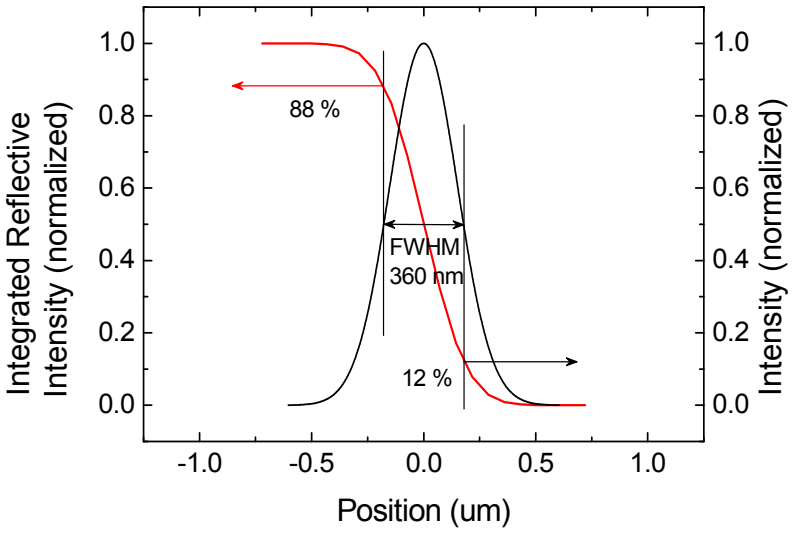

Figure 3.4 Calculation of spatial resolution when the laser shows Gaussian distribution.

3.3. Fundamental optical properties

3.3.1 Inhomogeneous broadening

Figure 3.5 indicates the results of photoluminescence for the undoped laser structures. The IQE evaluated from the PL intensity ratio between 7 and 295 K is 27.5 %. As quantified in Fig. 3.5(b), the full width at half maximum (FWHM) is as narrow as 70 meV at low temperatures and 116 meV at RT. Consequently, LO-phonon replicas are well resolved in the PL spectra [Fig. 3.5(a)]. The PL peak energy exhibits a clear S-shape behavior, suggesting carrier/exciton redistribution within potential fluctuations. Assuming a Gaussian distribution of the density of state, the temperature (T) dependence of the PL peak [$E(T)$] can be fitted with

$$E(T) = E_g(0) - \alpha T^2 / (T + \beta - \sigma^2 / kT), \tag{3.2}$$

where $E_g(0)$ is the band gap at 0 K, α and β are Varshni's fitting parameters, k is the Boltzman constant, and σ is a standard deviation of the Gaussian distribution [17]. The result of the fit is indicated by solid line in Fig. 3.5(b), providing $E_g(0)$=2.377 eV and σ ~20 meV. The energy difference between $E_g(0)$ and the PL emission peak corresponds to the Stokes shift at a low temperature, which is evaluated to be 60 meV. The σ value of 20 meV corresponds to an FWHM of 50 meV, represents potential fluctuations that excitons can feel during their motion. The difference from the PL FWHM at low temperatures can be attributed to the long-range potential fluctuations, as discussed below. The presence of such short-range and long-range fluctuations has already been discussed [18]. All the quantities (σ =20meV, PL FWHM=70 meV, and a Stokes shift of 60 meV) indicate remarkable suppression of inhomogeneous broadening in the current laser structure, compared with conventional QWs [19]. This is quite advantageous to achieve better differential gain properties [13].

Let us discuss the effects of the inhomogeneous broadening on spatial distribution of PL at RT. A confocal microscope was used for microscopic PL measurements of the undoped green laser structure. In this particular case, the excitation source was an InGaN LD emitting

at 405 nm, and the detection was through a spectrometer. As shown in Fig. 3.6(c), the PL intensity is spatially distributed with island-like structures.

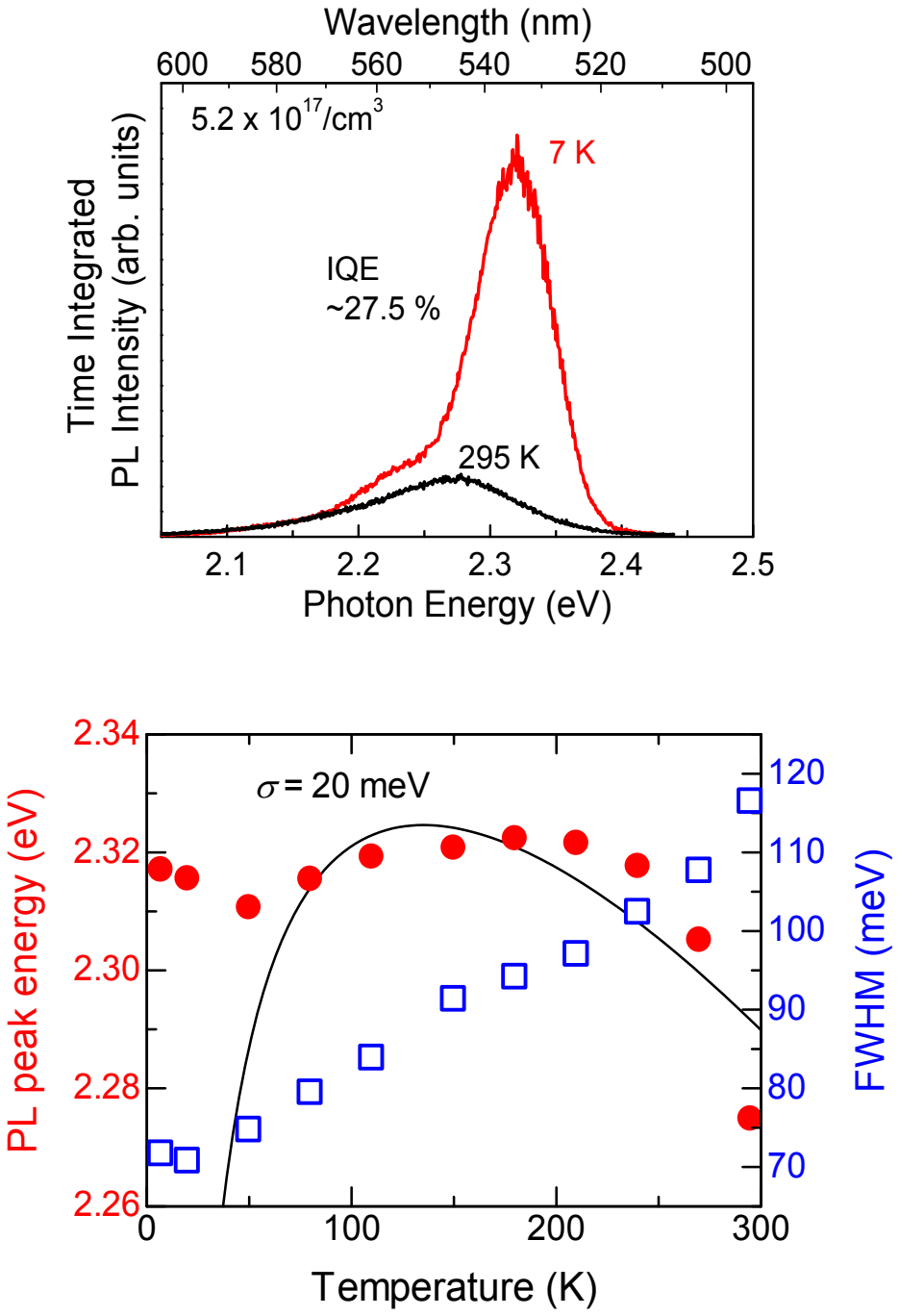

Figure 3.5. (a) Time-integrated PL spectra of undoped green laser structures acquired at 7 and 295 K. The photoexcited carrier density is 5 × 10^{17}/cm^3. (b) Temperature dependence of the emission peak energy and FWHM. The solid curve is the result of fit.

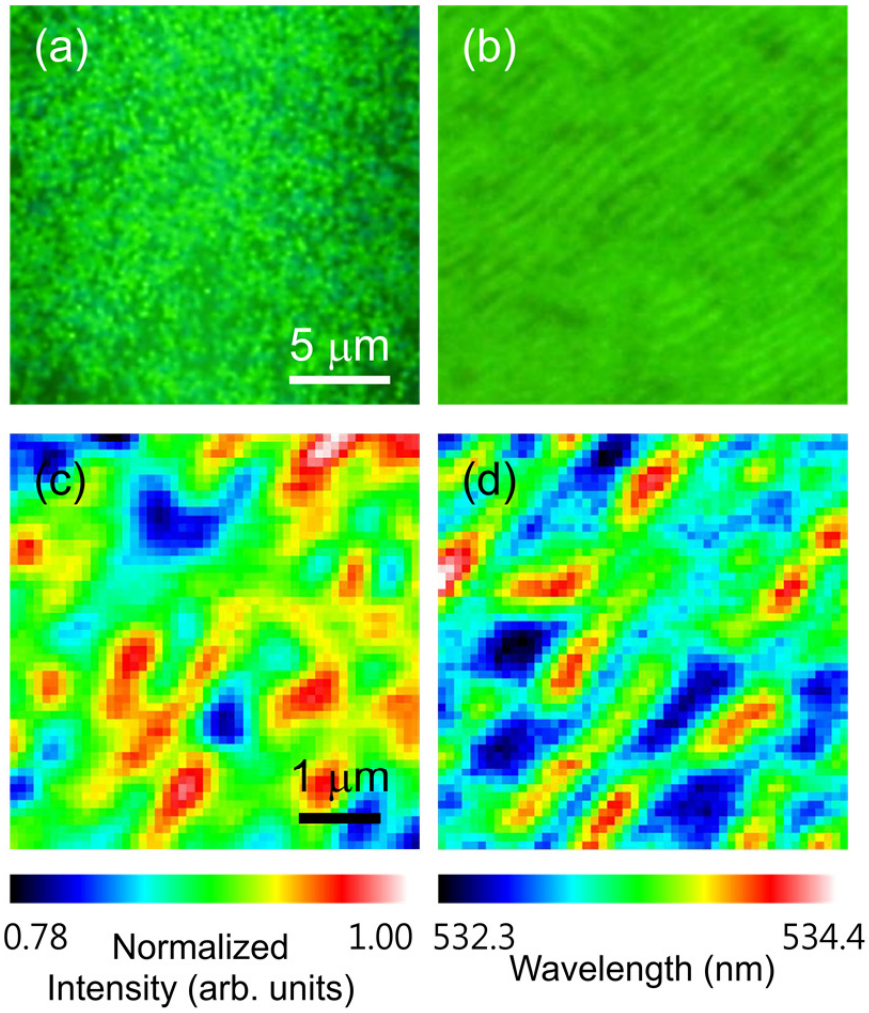

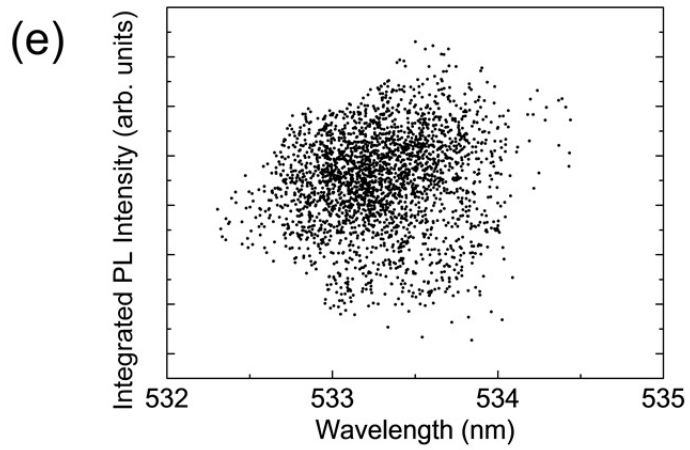

Figure 3.6 Fluorescence images of (a) green QW on ELOG GaN template, and (b) green laser structure on GaN substrate. Nanoscopic confocal PL mapping of green laser structure (c) intensity mapping, and (d) wavelength mapping. (e) Relation between intensity and wavelength.

However, the distribution is in the range of 78 to 100 % and makes a striking difference from the conventional green QW which showed an intensity fluctuation of more than 90 % [20]. The PL peak energy also fluctuates from 2.320 eV (534.4 nm) to 2.330 eV (532.3 nm), as shown in Fig. 3.6(e). Figures 3.6(c) and 3.6(d) indicate that the long range potential fluctuations suggested in Fig. 3.5 are responsible for an energy variation of 10 meV (2.330-2.320 eV) within the spatial resolution of the confocal microscopy.

The spatial distribution revealed in Fig. 3.6 supports the aforementioned argument that the inhomogeneous broadening is well suppressed in the state-of-the-art green laser structure.

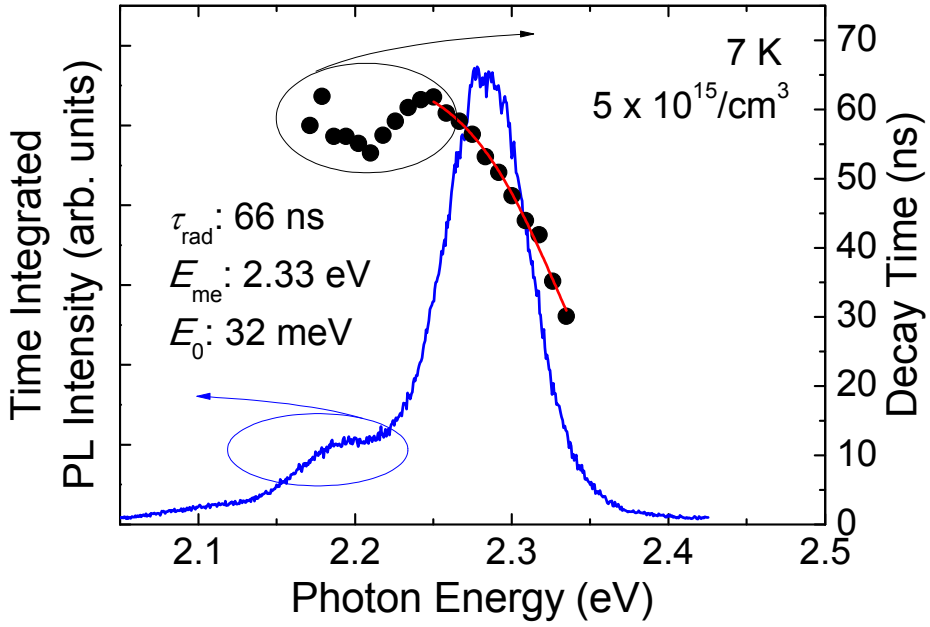

Figure 3.7 Time-integrated PL spectrum and recombination lifetimes (closed circles) at 7 K. The photoexcited initial carrier density is 5 x 1015/cm3. Weakly localized exciton model (solid line) provides a radiative lifetime of 66 ns.

3.3.2 Exciton/carrier dynamics

To assess exciton/carrier dynamics in the undoped green laser structures, time-resolved PL measurements (TRPL) were performed at 7 K with low carrier density to avoid many body effects, and 5 x 10^{15}/cm^3 is low enough to do so.

Figure 3.7 shows time-integrated PL spectrum and recombination lifetimes. The estimated lifetimes plotted in Fig. 3.7 are affected solely by radiative recombination processes, particularly at low temperatures such as 7 K. Using a weakly localized exciton model [21], the estimated radiative recombination lifetime is 66 ns (solid line in the Fig. 3.7). It is noteworthy that a conventional 3-nm-thick green QW with an In composition of 25 % exhibits a radiative recombination lifetime of 138 ns [22]. Therefore, the current green laser structure is likely to adopt thinner QWs to avoid the influence from the polarization field.

3.3.3 In composition and well width

From the experimental data presented in section 3.3.1 and 3.3.2, an In composition and a well width in the green laser structure can be deduced. The important parameters are $E_g(0)$ = 2.337 eV and the radiative recombination lifetime of 66 ns. Figure 3.8 indicates the calculated transition energy at 0 K, square of the overlap integral of the electron and hole wavefunctions, and internal electric field as functions of In composition. The longitudinal broken line in the bottom panel of Fig. 3.8 represents the experimentally obtained transition energy, $E_g(0)$. The experimentally determined radiative lifetime in the undoped green laser structure is 66 ns, whereas that in the conventional green QW (In=25%, well width=3nm) is 138 ns, as commented above. Because the square overlap integral is inversely proportional to the radiative recombination lifetime, that in the undoped green laser structure should be 138/66 times larger, which is designed by the broken line in the middle panel of Fig. 3.8. Our green laser structure must satisfy both the conditions simultaneously. Thus, an In composition of 28+2% and a well width of 2.5+0.27 nm (9+1 monolayers) were derived. The errors were evaluated from the PL line width. Using those quantities, the magnitude of the internal electric field was estimated to be ~2.7 MV/cm. those quantities are indicated by open circles in the Fig. 3.8.

It is noteworthy that the optimization of the epilayer structure for green LDs is directed toward thinner QWs with higher In composition, though the crystal growth becomes difficult due to high In compositions.

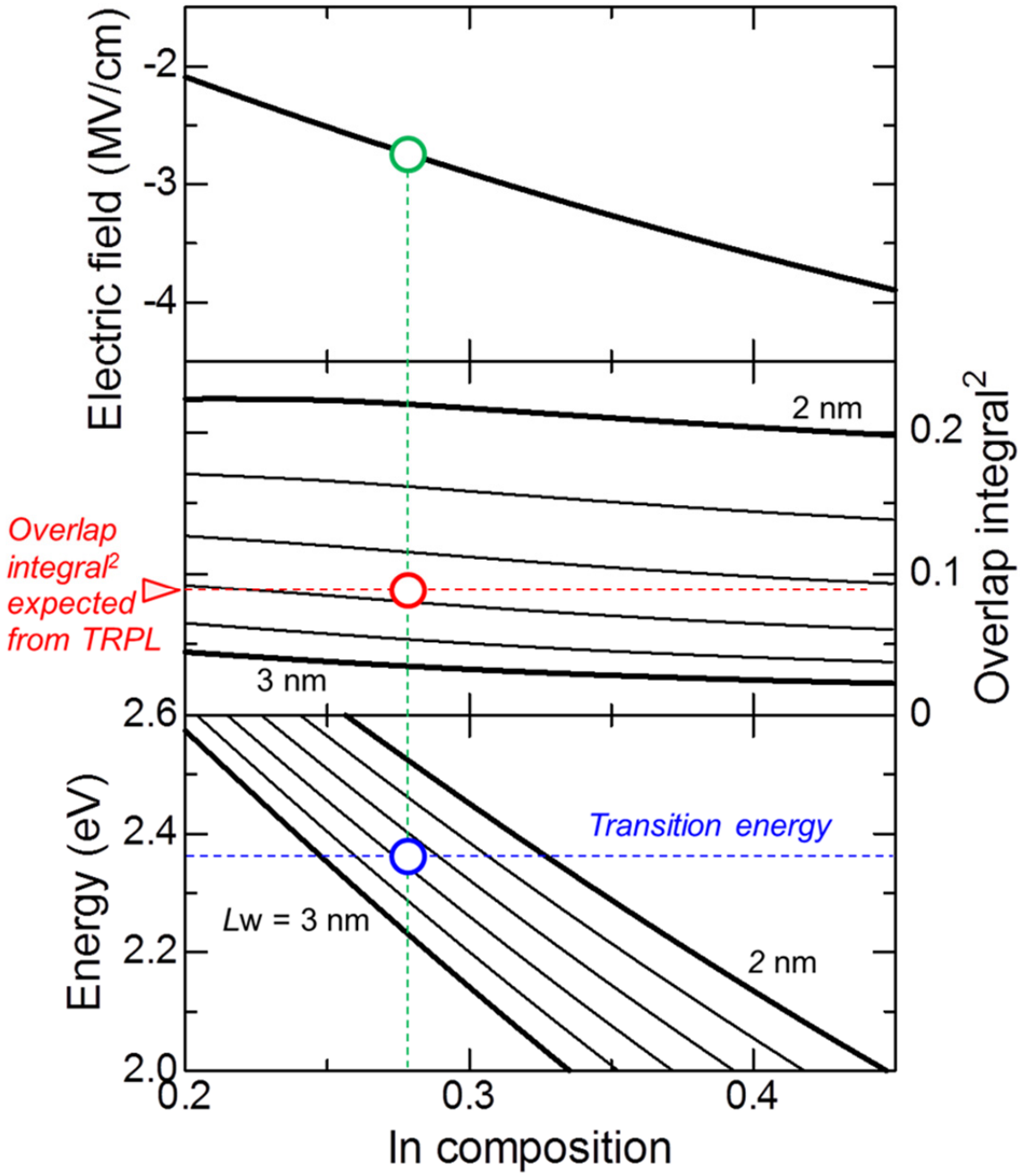

Figure 3.8 Transition energy at 0 K, square of the overlap integral of electron and hole wavefunctions, and internal electric field as functions of In composition. The well width (L_w) is a parameter and is varied between 2 and 3 nm with a step of 0.2 nm.

3.4 Summary

It is investigated the optical properties of the state-of-the-art green LD structure fabricated on (0001) GaN substrates, with the particular interest in PL inhomogeneity. The inhomogeneous potential fluctuations were drastically suppressed, compared with conventional QWs. In addition, thinner QWs with higher In compositions were used to improve radiative recombination probability. Those efforts have paid off to lower the threshold current densities in the recent (0001) green LDs.

References

1) M. Funato, M. Ueda, Y. Kawakami, Y. Narukawa, T. Kosugi, M. Takahashi, and T. Mukai, *Jpn. J. Appl. Phys.* **45**, L659 (2006).

2) Y. Enya, Y. Yoshizumi, T. Kyono, K. Akita, M. Ueno, M. Adachi, T. Sumitomo, S. Tokuyama, T. Ikegami, K. Katayama, and T. Nakamura, *Appl. Phys. Exp.* **2**, 082101 (2009).

3) T. Takeuchi, H. Amano, and I. Akasaki, *Jpn. J. Appl. Phys.* **39**, 413 (2000).

4) S.-H. Park and S. L. Chuang, *Phys. Rev. B* **59**, 4725 (1999).

5) S.-H. Park, *Jpn. J. Appl. Phys.* **42**, L170 (2003).

6) Y. Yoshizumi, M. Adachi, Y. Enya, T. Kyono, S. Tokuyama, T. Sumitomo, K. Akita, T. Ikegami, M. Ueno, K. Katayama, and T. Nakamura, *Appl. Phys. Exp.* **2**, 092101 (2009).

7) S. Takagi, Y. Enya, T. Kyno, M. Adachi, Y. Yoshizumi, T. Sumitomo, Y. Yamanaka, T. Kumano, S. Tokuyama, K. Sumiyoshi, N. Saga, M. Ueno, K. Katayama, T. Ikegami, T. Nakamura, K. Yanashima, H. Nakajima, K. Tasai, K. Naganuma, N. Fuutagawa, Y. Takiguchi, T. Hamaguchi, and M. Ikeda, *Appl. Phys. Exp.* 5, 082102 (2012).

8) T. Miyoshi, S. Masui, T. Okada, T. Yanamoto, T. Kozaki, S. Nagahama, and T. Mukai, *Appl. Phys. Exp.* **2**, 062201 (2009).

9) A. Avramescu, T. Lermer, J. Muller, C. Eichler, G. Bruederl, M. Sabathil, S. Lutgen, and U. Strauss, *Appl. Phys. Exp.* **3**, 061003 (2010).

10) S. Nagahama, Intern. Workshop on Nitride Semiconductor 2012, PL4, Sapporo, Japan (2012).

11) K. Kojima, M. Funato, Y. Kawakami, S. Nagahama, T. Mukai, H. Braun, and U. T. Schwarz, *Appl. Phys. Lett.* **89**, 241127 (2006).

12) K. Kojima, M. Funato, Y. Kawakami, S. Nagahama, and T. Mukai, *Opt. Exp.* **15**, 7330 (2007).

13) W. G. Scheibenzuber, U. T. Schwarz, T. Lermer, S. Lutgen, and U. Strauss, *Appl, Phys. Lett.* **97**, 021102 (2010).

14) T. Lermer, A. Gomez-Iglesias, M. Sabathil, J. Muller, S. Lutgen, U. Strauss, B. Pasenow, J. Hader, J. V. Moloney, S. W. Koch, W. Scheibenzuber, and U. T. Schwarz, *Appl. Phys. Lett.* **98**, 021115 (2011).

15) Y. S. Kim, A. Kaneta, M. Funato, Y. Kawakami, T. Kyono, M. Ueno, and T. Nakamura. *Appl. Phys. Exp.* **4**, 052103 (2011).

16) P. G. Eliseev, P. Perlin, J. Lee, and M. Osinski, *Appl. Phys. Lett.* **71**, 569 (1997).

17) K. Kazlauskas, G. Tamulaitis, P. Pobedinskas, A. Zukauskas, M. Springs, C.-F. Huang, Y.-C. Cheng, and C. C. Yang, *Phys. Rev. B* **71**, 085306 (2005).

18) K. P. O'Donnell, R. W. Martin, and P. G. Middleton, *Phys. Rev. Lett.* **82**, 237 (1999).

19) A. Kaneta, M. Funato, and Y. Kawakami, *Phys. Rev. B* **78**, 125317 (2008).

20) C. Gourdon and P. Lavallard, *Phys. Stat. Sol. B* **153**, 641 (1989).

21) Y. Kawakami, A. Kaneta, and M. Funato, *Mater. Sci. Forum,* **590**, 249 (2008).

22) B. W. Hakki and T. L. Paoli, *J. Appl. Phys.* **44**, 4113 (1973).

23) E. Kioupakis, P. Rinke, and C. G. Van de Walle, *Appl. Phys. Exp.* **3**, 082101 (2010).

24) K, Okamoto, T. Tanaka. M. Kubota, and H. Ohta, *Jpn. J. Appl. Phys.* **46**, L820 (2007).

Chapter 4.

Optical Gain Properties of Polar (0001) Green InGaN Laser Diodes

In the previous chapter we discussed the fundamental optical properties of a green laser structured sample fabricated on the (0001) GaN substrate. We understood that inhomogeneous broadening and piezoelectric polarization induced internal electric field play significant roles in high In concentration green LDs. Using EL, we can evaluate the optical mode gain by analyzing the intensity ratio between the maximum and minimum values of each longitudinal mode. Optical mode gain properties of LDs from the violet to cyan spectral region were thoroughly investigated [1]. It is noteworthy that gain suppression becomes severe as In composition in the InGaN well layers increases. Inhomogeneous broadening as appears to be the major reason for the suppression. Similar to LEDs, current injection is also an important issue for green LDs, and leads to efficiency droop. As for light confinement, the difference in the refractive indices of the InGaN guiding and AlGaN cladding layers becomes smaller as the wavelength increases. Therefore, the confinement factor of green laser diodes is smaller than that of shorter wavelength laser diodes.

4.1. Optical mode gain

4.1.1 Stimulated emission by optical pumping

Optical pumping was performed by a nano-second pulsed laser of YAG. The sample structure is identical to a laser diode device without doping and lacks mirror facets for the cavity. The excitation energy of optical pumping in the range of 0.5 to 20 mJ/cm^2 was

examined. As seen in Fig. 4.1(a), sharp stimulated emission is observed for over 10 mJ/cm^2. PL is collected by the 50 cm focal length monochromator and then dispersed by 150 gr/mm. Even though the sample does not have any cavity mirrors TE mode is clearly observed as shown in Fig. 4.1(a). Since a sharp lasing-like spectrum is observable even though the emission is stimulated. We infer that the confinement along the vertical growth direction is very strong.

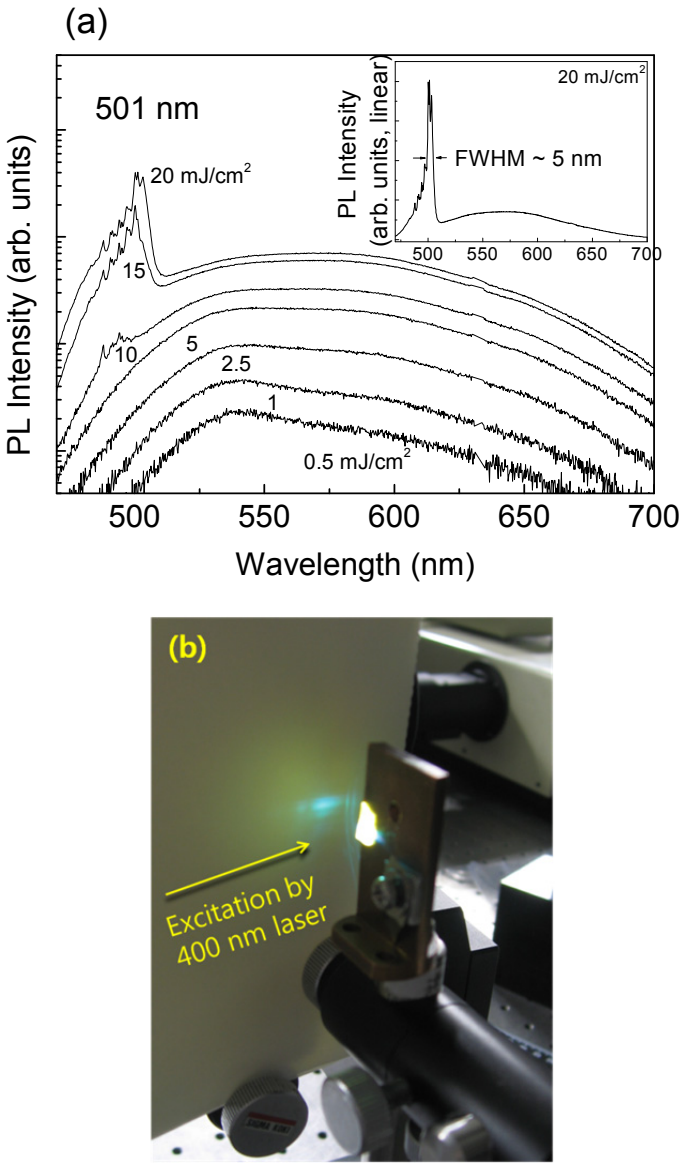

Figure 4.1 (a) Excitation power dependent PL spectra of stimulated emission. (b) Far-field pattern image from the sample.

4.1.2 Spontaneous and stimulated emission spectra

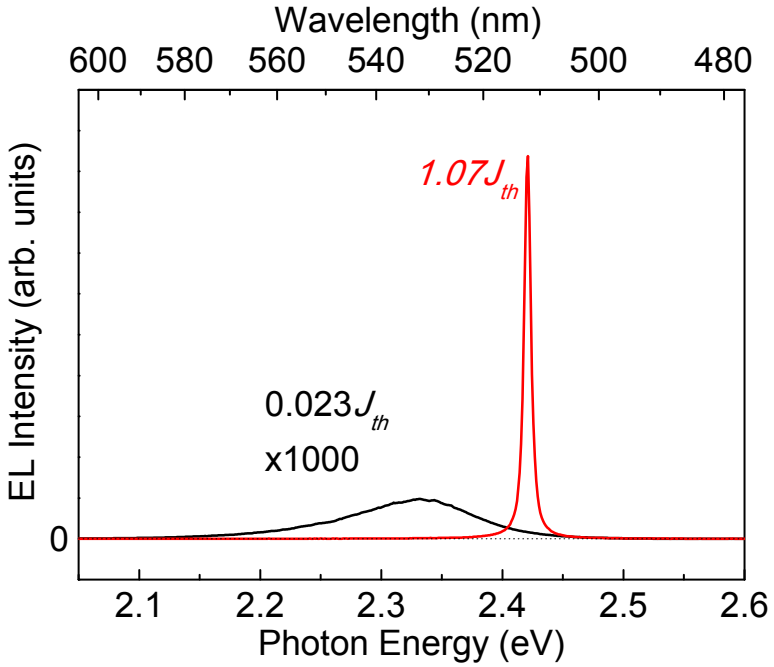

Figure 4. 2 EL spectra of spontaneous ($0.023J_{th}$) and stimulated ($1.07J_{th}$) emissions for the (0001) green LD.

Figure 4.2 compares the EL spectra of the green LD operated below and above the threshold current density (J_{th}) of 2.75 kA/cm^2 (note that because a low-resolution spectrometer was used for these measurements, the longitudinal modes cannot be resolved). The resultant power efficiency is 6.8% with a driving current density, applied voltage, and output power of 7.63 kA/cm^2, 6.0 V, and 50 mW, respectively. The peak energy difference between the spectra below and above the threshold (i.e., $0.023J_{th}$ and $1.07J_{th}$, respectively) is 86 meV. This energy shift is almost one-third of that for a conventional blue-green LD used in Refs. [12] and [1] (data not shown).

4.1.3. Hakki and Paoli's scheme

In early 1970s, Hakki and Paoli measured the optical mode gain under current injection condition [2]. They noticed that the absorption coefficient of the materials in the cavity is related to the modulation depth of longitudinal modes by the interference of Fabry-Perot etalon. Emitted light from the side edge of the sample travels inside the cavity, and so the longitudinal modes are modulated by the cavity. The spacing between these modes is related to the cavity length and wavelength. The green LDs that have a cavity of 600 μm long have ~80 pm mode space at 525 nm. To resolve such a narrow space, a high resolution monochromator is necessary. Therefore, the EL was dispersed by a 1 m monochromator with a resolution of 4 pm. This measurement scheme is illustrated in Fig. 4.3.

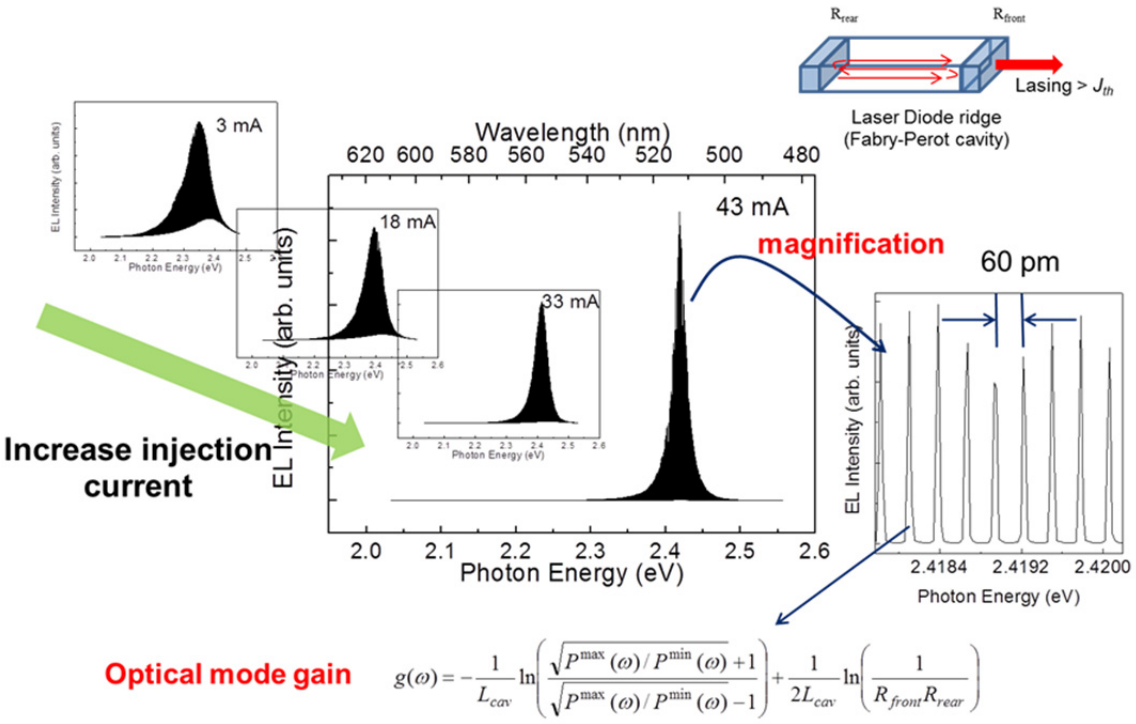

Figure 4.3 Schematic procedures for Hakki-Paoli measurement.

Let us derive the relation for the optical mode gain measurement proposed by Hakki-Paoli. To this end, we define a damping factor α with respect to the power of the light mode [$P(\omega)$]. Therefore, the damping factor for the electric field amplitude becomes α/2, which is the imaginary part of the propagation parameter. The reflectance coefficients at both the mirrors are R_1 and R_2. Then electric field amplitude is given by

$$E_n(\omega) = (R_1R_2)^{1/2} \exp\{(\alpha + j\theta)L_{cav}\}E_{n-1}(\omega) \tag{4.1}$$

$$= x(\theta)E_{n-1}(\omega), \tag{4.2}$$

where E_n, L_{cav}, θ represent electric field amplitude, length of cavity, and phase of the electric field, respectively. When light with frequency ω and mode m travels n times, $\theta = 2\pi m$, and $\theta = (2m+1)\pi$ give the condition for maximum and minimum transmission in the Fabry-Perot cavity. Therefore, electric field satisfying the multiple resonance condition can be expressed in terms of the initial electric field E_0 as

$$E^{\max}(\omega) = \sum_{n=0}^{\infty} x^n(2\pi m) = \frac{E_0}{1-(R_1R_2)^{1/2}\exp\{\alpha(\omega)L_{cav}\}}. \tag{4.3}$$

While electric field satisfying the anti-resonance condition can be expressed as

$$E^{\min}(\omega) = \sum_{n=0}^{\infty} x^n((2m+1)\pi) = \frac{E_0}{1+(R_1R_2)^{1/2}\exp\{\alpha(\omega)L_{cav}\}}. \tag{4.4}$$

Then, we can eliminate E_0 from both equations and rewrite with respect to α,

$$\alpha(\omega) = -\frac{1}{L_{cav}}\ln\left(\frac{E^{\max}(\omega)/E^{\min}(\omega)+1}{E^{\max}(\omega)/E^{\min}(\omega)-1}\right) + \frac{1}{2L_{cav}}\ln\left(\frac{1}{R_1R_2}\right) \tag{4.5}$$

$$= -\frac{1}{L_{cav}}\ln\left(\frac{\sqrt{P^{\max}(\omega)/P^{\min}(\omega)}+1}{\sqrt{P^{\max}(\omega)/P^{\min}(\omega)}+1}\right) + \frac{1}{2L_{cav}}\ln\left(\frac{1}{R_1R_2}\right). \tag{4.6}$$

Therefore, using the equation above, we can obtain the absorption spectrum $\alpha(\omega)$ from the measured light intensity or luminescence $P(\omega)$. Note, in the equation above, the first left term on the right hand side is an experimentally measured value and consequently, it becomes 0 just below the threshold current density. The second term on the right side is the compensation of mirror loss designed value. We call the first term the internal total loss and $\alpha(\omega)$ the mode gain (or loss).

4.1.4. Injection current density dependent mode gain

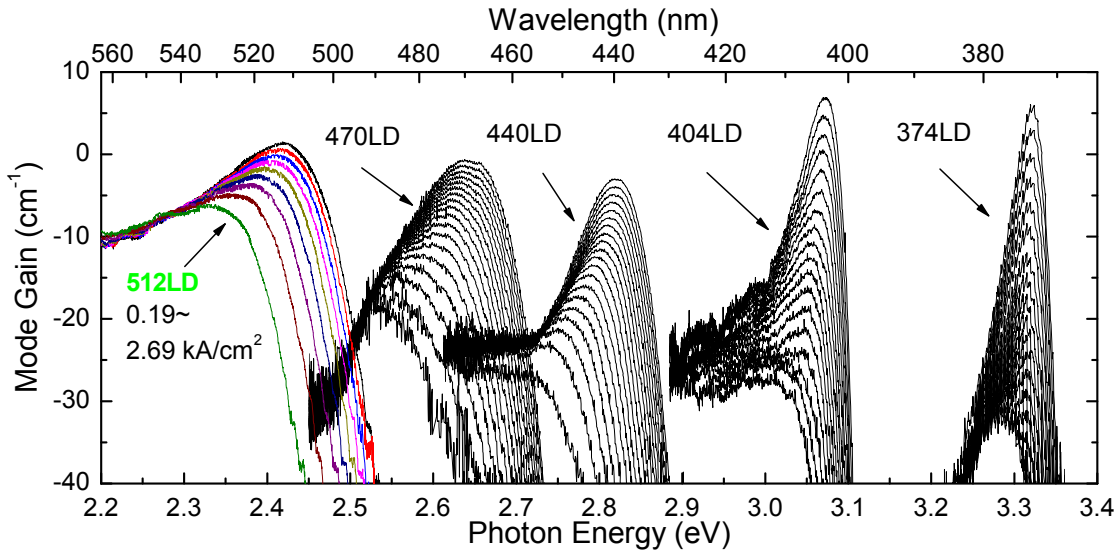

Figure 4.4 optical mode gains of a green LD in comparison with shorter wavelength LDs on polar (0001) plane

Dependence of the optical mode gain spectra of the green LD on the injection current density is plotted in Fig. 4.4, in comparison with shorter wavelength LDs. In each LD, the gain value saturates on the lower energy side regardless of the injection current density. These values correspond to the internal loss of the LDs. Interestingly, in Fig. 4.4, the internal loss of the green LD shows the lowest value among the LDs in comparison. This indicates that the sources of internal loss are restricted in the green LD. According to a previous calculation [3] internal loss of green LDs is about 16.5 cm^{-1}. The maximum contribution is from Mg dopant,

which is approximately 9.7 cm^{-1}. Thus, it is implied that the Mg doped p-(Al)GaN layers are changed significantly in the state-of-the-art green LD.

4.1.5 Fitting results of gain spectra and inhomogeneous broadenings

Figure 4.5 shows fitting results onto the gain spectra of the green LD presented in Fig. 4.4.

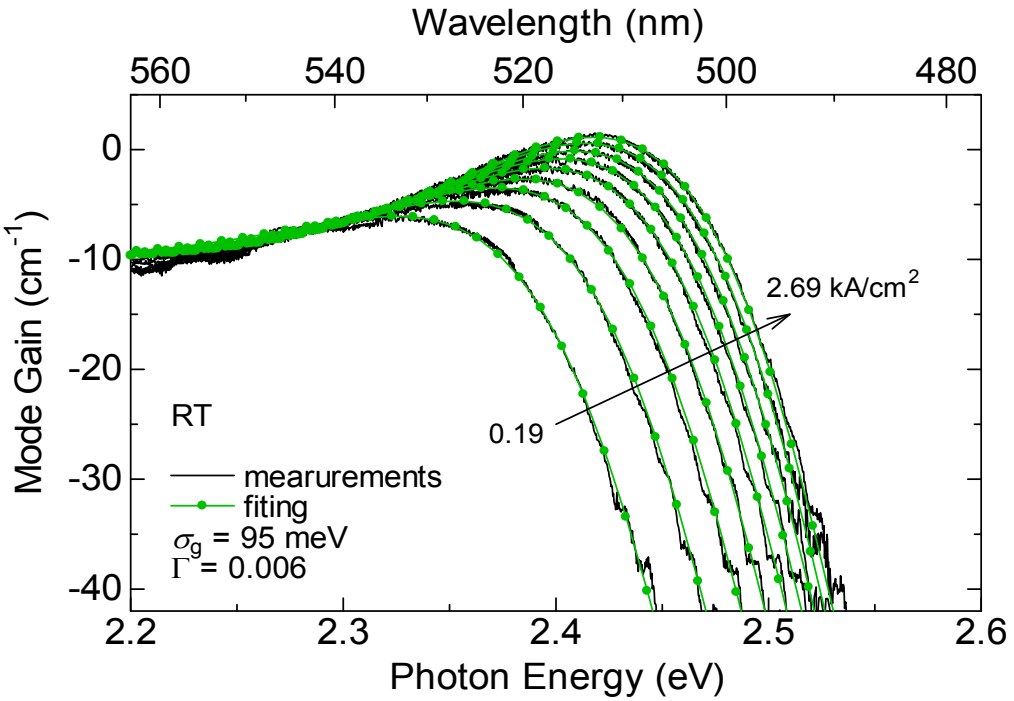

Figure 4.5 Measured gain spectra under different injection current density ranging from 0.19 to 2.69 kA/cm^2. The gain spectra were theoretically fitted, and the circles represent the best fit.

The theoretical gain spectra were calculated with the free carrier, single-band effective mass approximation. Homogeneous broadening is treated as a constant (25 meV), which is included in a form of a hyperbolic secant function (sech) [4]. The inhomogeneous broadening due to potential fluctuations is expressed by DOS with a Gaussian distribution with a

standard deviation (σ_g). For the calculation, we adopted the model proposed in Ref. [5], which assumes global constant quasi-Fermi levels for the valence and conduction bands. The best fit is achieved with σ_g = 95 meV, an optical confinement factor Γ = 0.006, and an internal loss of 10/cm.

To assess the improvement of inhomogeneous broadening, Fig. 4.6 compares previously reported inhomogeneous broadening determined by analyzing the gain spectra. Inhomogeneous broadening of the present green LD is well suppressed compared with those in an earlier report [1], but is similar to those of recent paper, and on the line of the recent LDs [6].

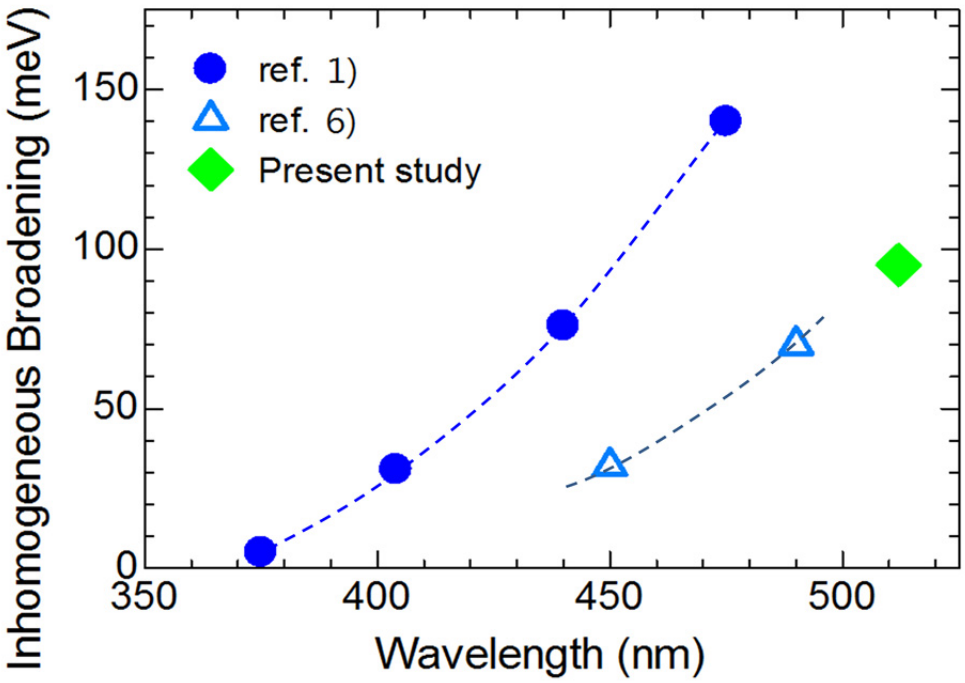

Figure 4.6 Inhomogeneous broadening reported in Refs. [1] and [6] and that estimated in the present study.

In Chapter 3, inhomogeneous broadening is evaluated from the PL temperature dependence of an undoped green laser structure with the same layered structure as the LD in this study. The "S-shape" behavior of the PL peak as a function of temperature allowed us to determine the standard deviation (σ) of a Gaussian distribution of DOS, which was ~20 meV.

Although both PL and gain analyses assume a Gaussian distribution, different deviations (σ and σ_g) are extracted. Currently, the reason remains unclear, but possible causes are discussed. Firstly, the standard deviation derived from the ‘‘S-shape’’ analysis represents a short-range potential fluctuation within an area in which each exciton/carrier is mobile, while the line width is a convolution of short-range and long-range fluctuations. [8] Therefore, the latter may be larger than the former. Secondly, the excitation conditions differ; PL is weakly excited, whereas Fig. 4.4 corresponds to a highly carrier injected condition. Under a strong excitation like lasing, excitons/carriers may delocalize, spreading over a wider spatial area compared with weakly excitation conditions. Because there are long-range fluctuations [7], delocalized excitons/carriers may experience those fluctuations as well, making $\sigma_g > \sigma$. Thirdly, the contribution of the electron LO-phonon interaction may broaden the gain spectra, as indicated in Ref. [6].

The fitting to the gain spectra allows the injection current density (J) to be correlated with carrier density (n), as shown in Fig. 4.6. The observed relationship is not proportional, suggesting some nonlinear processes. This relationship can be expressed as

$$n \propto \frac{\tau(\eta J)}{e}, \tag{4.7}$$

where τ is the recombination lifetime, η is the efficiency of the current injection into the active region, and e is the elementary charge. (τ and η are important param eters that determine the device efficiency.) Both τ and η depend on the injection current (i.e. $\tau(J)$ and $\eta(J)$, precisely), and cause the nonlinear relationship between J and n_{2D}. Their product, $\eta\tau$, can be estimated using Eq. (4.7), which is also shown in figure 4.6. The estimated $\eta\tau$ decreases monotonically.

Generally, η decreases as the injection current increases due to current overflow. The current dependence of τ may be more complicated; τ can be further resolved into

$$\frac{1}{\tau} = \frac{1}{\tau_r} + \frac{1}{\tau_{nr}} \tag{4.8}$$

where τ_r and τ_{nr} are the radiative and nonradiative lifetimes, respectively. Increasing the injection current may cause the following variations. Radiative recombination processes become faster due to, for example, the contribution of light amplified by a stimulated emission of radiation. On the other hand, nonradiative recombination centers, which are filled as the current increases, may increase τ_{nr}, whereas the density-activated defect recombination [9] and Auger process [10] may decrease τ_{nr}. Presently, the contributions of τ_r, τ_{nr}, and η to the current-dependent carrier density remains unanswered. It should be noted that although the simple Shockley–Read–Hall (SRH) model can reproduce the results for a UV laser [11], the model cannot reproduce the experimental results in Fig. 4.6, indicating that the recombination processes and current overflow are not that simple in the state-of-the-art green LD structure.

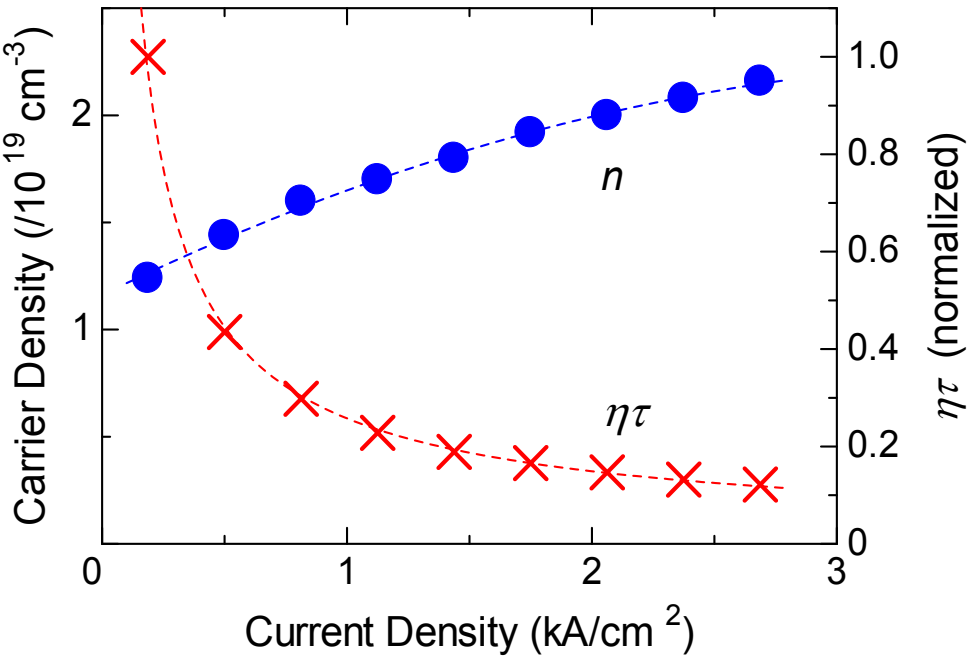

Figure 4.7 Carrier density and ητ as functions of injection current density estimated from the fitting to the gain spectra. Lines are to guide the eye.

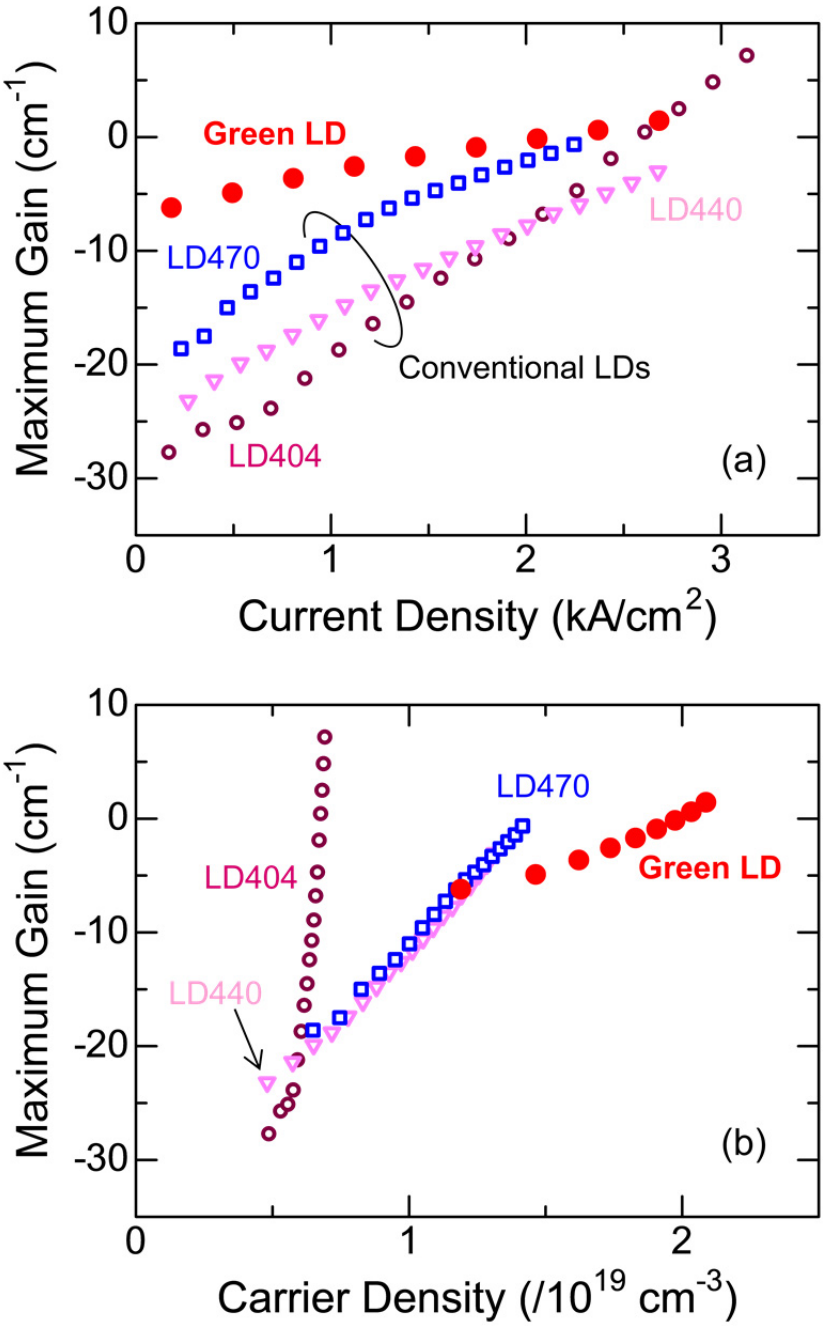

Figure 4.8 Variation of maximum gain as a function of (a) injection current density and (b) carrier density. LD404, LD440, and LD470 represent conventional LDs emitting at 404, 440, and 470 nm, respectively.

Figure 4.8(a) shows the variations of the maximum gain values as a function of the injection current density. For comparison, the properties of conventional LDs emitting at 404, 440, or 470 nm are also plotted [1]. Because the gain fitting correlates the injection current density and carrier density (n) like in Fig. 4.7, the maximum gain values are re-plotted in Fig. 4.8(b) as a function of the carrier density. The slope provides the differential mode gain values of 2.4×10^{-17}, 2.4×10^{-18}, 2.4×10^{-18}, and 8.6×10^{-19} cm^2 for LD404, LD440, LD470, and the present green LD, respectively. One characteristic feature of the green LD is the small differential mode gain. To understand the cause of this observation, recall that the estimated mode gain (g) can be expressed as eq. (2.27, $g = \Gamma G - \alpha (1 - \Gamma)$), where G is the material gain and α is the loss outside the QW region.

As pointed out in Ref. [13], the difference in the refractive indices of the guiding and cladding layers becomes smaller for longer wavelength ranges, resulting in a small Γ. Furthermore, a thinner well in the green LD may contribute to a smaller Γ. In fact, the fitting to the gain spectra reveals $\Gamma = 0.006$ (Fig. 4.5), which is much smaller than the conventional UV to blue-green LDs ($\Gamma = 0.016$ -0.03) Taking Γ into account, the differential material gain (dG/dn) values are estimated to be 8.0×10^{-16}, 1.5×10^{-16}, 1.5×10^{-16}, and 1.4×10^{-16} cm^2 for LD404, LD440, LD470, and green LD, respectively.

Therefore, although G of the green LD increases with injection carrier similar to the shorter wavelength LDs (except for LD404), the apparent g has a smaller slope due to the smaller Γ. It is also noteworthy that the relatively high linearity of the gain increase against the carrier density may also suggest the suppression of potential inhomogeneity, which has been reported to suppress a gain increase [12].

4.2 Peak energy comparison as functions of current density and carrier density

Current injection is an important issue for optoelectronic devices such as LEDs and LDs. Numerous researchers are studying the efficiency droop phenomena. In the calculation, a built-in electric field is not considered, and carrier density is used as opposed to current density. Therefore, the relation between both quantities is extracted from the gain fit in Fig. 4.5. The measured values of EL and gain peak are plotted as functions of current density in Fig. 4.9(a). Figure 4.9(b) plots these values as functions of carrier density for comparison. After such an operation, the measured data could be compared using same physical quantity

of carrier density. Furthermore, the plotted peak energy shifts are compared to the calculated results as in Fig. 4.9(b).

In the low carrier (or current) density regime, EL peak energies show 'V' shape shift. This can be explained by the contribution of the built-in electric field (E_{bi}), and the internal electric field (E_{pz}) caused by piezoelectric polarization.

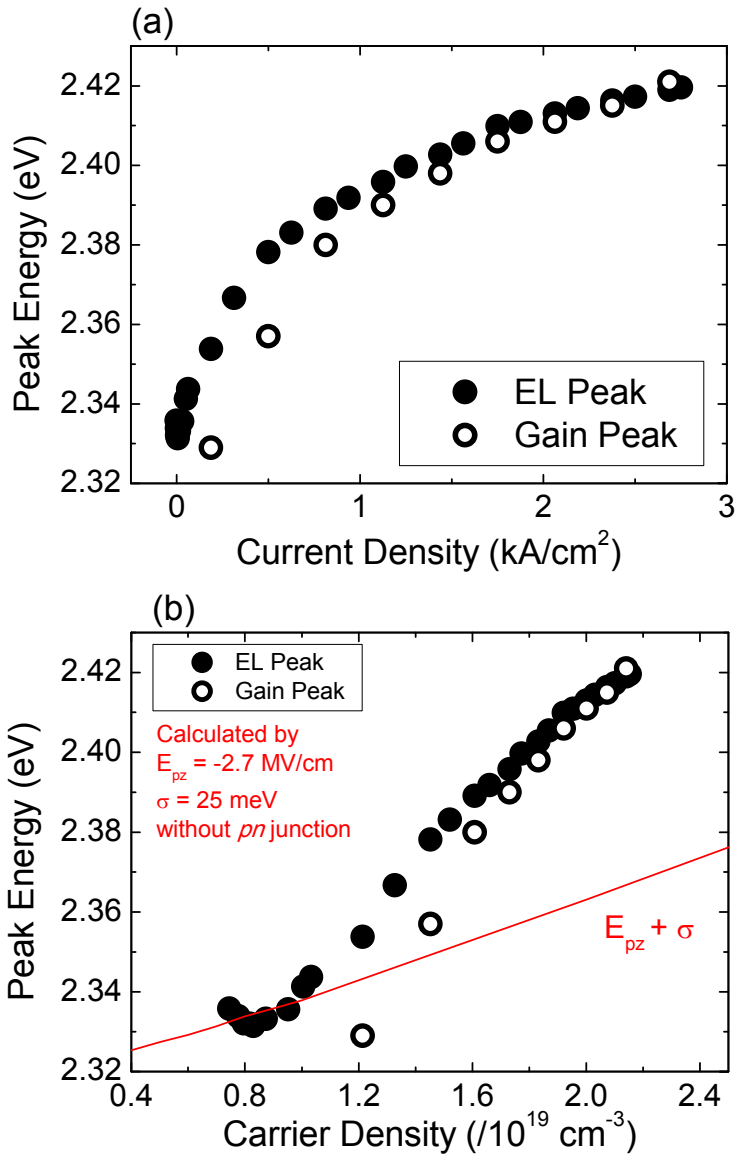

Figure 4.9 Gain and EL peak energy plotting as a function of (a) current density (kA/cm^2) and (b) carrier density (/10^{19} cm^{-3}).

Note that the direction of E_{pz} is opposite to that of E_{bi}. Thus, both the fields nearly cancel each other and small electric field remains pointing in the direction opposite to the growth direction. This is because the internal electric field caused by P_{pz} is larger than the built-in field. As injection carriers increase, the electric field E_{bi} becomes smaller and the peak energy shifts towards the lower energy end. If the injection carriers increase beyond the flat band condition, which is about 3-4mA based on the I-V curve of LDs (not shown here), the carrier screening effect appears. Therefore, the peak energy shift, known as QCSE, occurs almost linearly. It is not clear why the peak energy shift observed is higher than the calculated value. This requires further investigation.

.

4.3 Summary

We investigated the optical properties of the state-of-the-art green LDs fabricated on (0001) GaN substrates. The inhomogeneous potential fluctuations are drastically suppressed, compared with conventional QWs. In addition, the use of thinner QWs with higher In compositions leads to lower threshold current densities. The gain spectroscopy revealed a quite low internal loss of 10/cm. The low differential gain was attributed to a low confinement factor. The linearity of gain increase with the injection current was also confirmed, and was attributed to minimized potential fluctuations.

References

1) K. Kojima, M. Funato, Y. Kawakami, S. Nagahama, and T. Mukai, *Opt. Exp.* **15**, 7330 (2007).

2) B. W. Hakki and T. L. Paoli, *J. Appl. Phys.* **44**, 4113 (1973).

3) E. Kioupakis, P. Rinke, and C. G. Van de Walle, *Appl. Phys. Exp.* **3**, 082101 (2010).

4) B. Witzigmann, V. Laino, M. Luisier, U. T. Schwarz, H. Fischer, G. Feicht, W. Wegscheider, C. Rumbolz, A. Lell, and V. Härle, *IEEE Photon. Technol. Lett.* **18,** 1600 (2006).

5) A. A. Yamaguchi, M. Kuramoto, M. Nido, and M. Mizuta, *Semicond. Sci. Techonol.* **16,** 763 (2001).

6) T. Lermer, A. Gomez-Iglesias, M. Sabathil, J. Müller, S. Lutgen, U. Strauss, B. Pasenow, J. Hader, J. V. Moloney, S. W. Koch, W. Scheibenzuber, and U. T. Schwarz, *Appl. Phys. Lett.* **98**, 021115 (2011).

7) M. Funato, Y.-S. Kim, T. Hira, A. Kaneta, Y. Kawakami,T. Miyoshi, and S. Nagahama, *Appl. Phys. Exp.* **6**, 111002 (2013).

8) K. Kazlauskas, G. Tamulaitis, P. Pobedinskas, A. Zukauska, M. Springis, C.-F. Huang, Y.-C. Cheng, and C. C. Yang, *Phys. Rev. B* **71**, 085306 (2005).

9) J. Hader, J. V. Moloney, and S. W. Koch, Appl. Phys. Lett. **96**, 221106 (2010).

10) Y. C. Shen, G. O. Mueller, S. Watanabe, N. F. Gardner, A. Munkholm, and M. R. Krames, *Appl. Phys. Lett.* **91**, 141101 (2007).

11) B. Witzigmann, V. Laino, M. Luisier, U. T. Schwarz, G. Feicht, W. Wegscheider, K. Engl, M. Furitsch, A. Leber, A. Lell, and V. Härle, *Appl. Phys. Lett.* **88**, 021104 (2006).

12) K. Kojima, M. Funato, Y. Kawakami, S. Nagahama, T. Mukai, H. Braun, and U. T. Schwarz, *Appl. Phys. Lett.* **89**, 241127 (2006).

13) K, Okamoto, T. Tanaka. M. Kubota, and H. Ohta, *Jpn. J. Appl. Phys.* **46**, L820 (2007).

Chapter 5.

Carrier Dynamics and Nanoscopic Optical Properties of Semipolar {20$\bar{2}$1} Green InGaN QWs

5.1 Introduction

It is important to understand the nanoscopic emission behavior of longer wavelength LEDs and LDs. As described in Chapter 3, restrained inhomogeneity of the InGaN layer contributed to the development of green LDs. To identify in-plane inhomogeneity confocal nanoscope PL was very useful to obtain spatial resolution over 360 nm, as discussed in chapter 3. However, methods with higher spatial resolution are necessary when the distribution of luminescence centers is smaller than the system resolution. In this chapter, we report the method and results of the investigation of nanoscopic optical properties by scanning near-field optical microscope (SNOM). An SNOM was used because the luminescence centers are distributed at length scales smaller than the spatial resolution of the confocal nanoscopic system, as indicated by preliminary measurements (not reported here). SNOM-PL is promising characteristic tool with high spatial resolution. We compare macroscopic temperature dependent PL results with those from SNOM-PL. These comparisons help us in understanding the kind of luminescent process that occurs. This chapter also details the comparison between results of atomic force microscopy (AFM) morphology and SNOM mapping data. Note, some orientations are preferred along the different orientations of [$\bar{1}$2$\bar{1}$0] and [$\bar{1}$014]. Furthermore, the semipolar plane can have advantages over the conventional polar plane, such as the suppression of compositional inhomogeneity [10] and enhancement of In incorporation [11]. In fact, InGaN-based light emitting devices have been fabricated on various planes, including the {10$\bar{1}$0} (m) plane [12], {11$\bar{2}$0} (a) plane, {11$\bar{2}$2} plane [13], {20$\bar{2}$1} plane [14-17], and (30$\bar{3}$1) plane

[18]. Recently, room temperature (RT) continuous-wave (CW) operation of pure-green LDs was realized by using InGaN QWs on $\{20\bar{2}1\}$ GaN substrates [15]. Since then, device performances have improved significantly [16,17].

5.2 Experiments

The sample used in this study is the same InGaN/GaN SQW as in Ref. [10], On a semipolar $\{20\bar{2}1\}$ GaN substrate produced by hydride vapor phase epitaxy, an LD structure, including a green-emitting InGaN QW active region, was grown by metal organic vapor phase epitaxy [10,11]. Threading dislocation densities of the substrate are less than 1×10^6 cm^{-2}. The thicknesses of the InGaN well and the GaN cap layer are 3 and 10 nm, respectively. The In composition is approximately 30%. The macroscopic PL peak wavelength is 530 nm at RT. To superimpose atomic force microscope (AFM) images and SNOM-PL maps, reference metal markers composed of Ni (10 nm)/Au (50 nm) were deposited on the sample surface.

To determine the fundamental properties of these QWs, we have assessed the macroscopic optical properties of $\{20\bar{2}1\}$ InGaN single QWs (SQWs) by means of CW and time-resolved photoluminescence (PL) [10], as well as the gain properties [19]. We found that potential fluctuations are suppressed in this semipolar plane. Herein, to study local PL characteristics in detail, we perform scanning near-field optical microscopy (SNOM) for a green-emitting $\{20\bar{2}1\}$ InGaN SQW. Figure 5.1 shows a schematic of SNOM.

SNOM-PL measurements were performed at RT using a double-taper fiber probe with an aperture diameter of 150 nm. A CW InGaN LD emitting at 405 nm was used to selectively excite the InGaN well. The excitation power density was about 7 kW/cm^2, which corresponded to a photogenerated carrier density of about 1×10^{18} cm^{-3}. PL signals were introduced into a 50-cm monochromator and were detected by a liquid nitrogen cooled charge coupled device detector. To assess carrier/exciton diffusion, we performed multimode SNOM, in which PL data were concurrently acquired in illumination (*I*) and illumination-collection (*I*-*C*) modes [20].

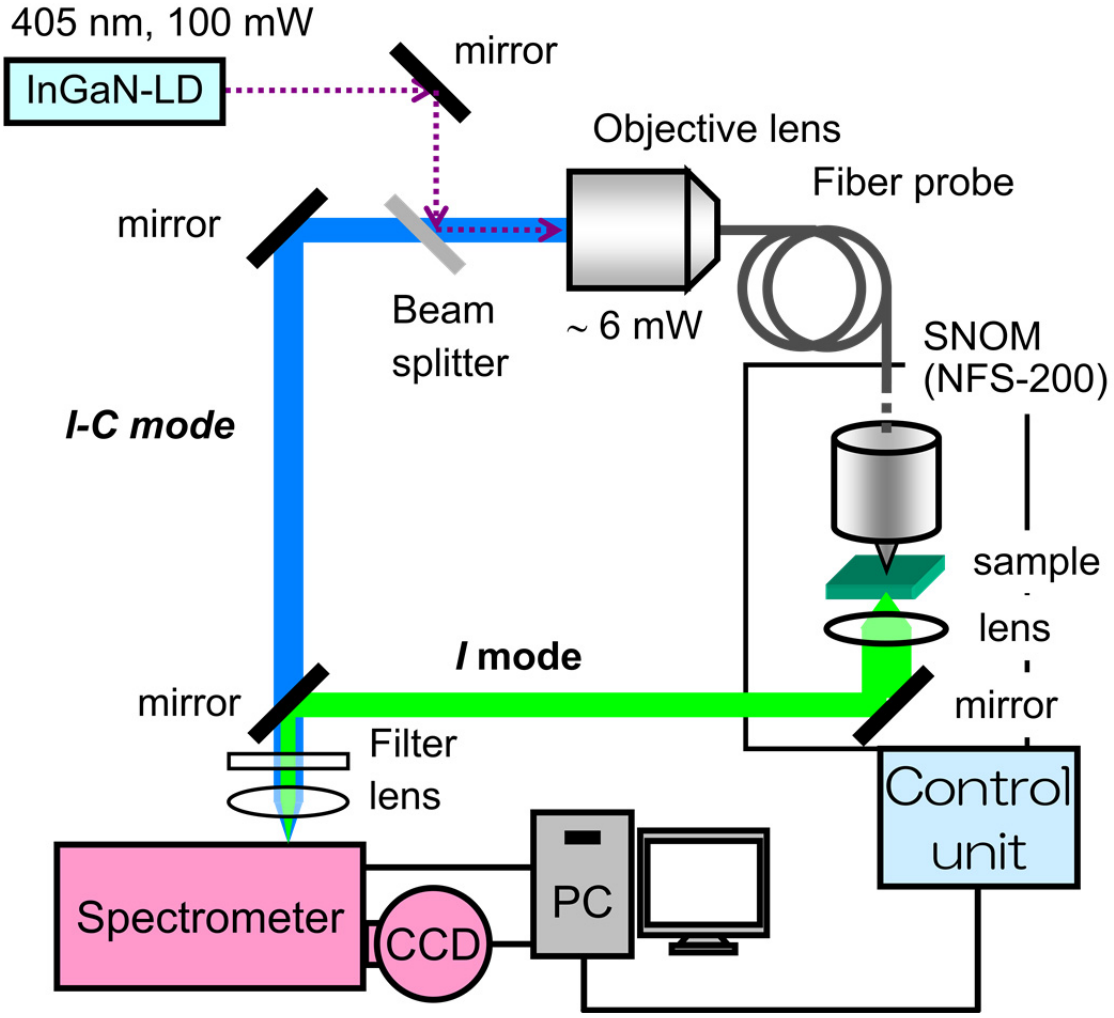

Figure 5.1 Experimental setup for SNOM-PL.

5.3 Results and discussions

Figure 5.2 summarizes temperature dependence of macroscopic PL. In this particular case, the excited carrier density was 1.6×10^{16} cm^{-3}. The FWHM exhibited plateau structures at low and high temperatures, while the peak energy showed an S-shape behavior. These properties were typical for polar (0001) InGaN QWs, where carriers/excitons were thermally re-distributed within the sea of potential fluctuations [21]. That is, Fig. 5.2 suggests that

carriers/excitons in the $\{20\bar{2}1\}$ SQW are also mobile, as described below. To discuss the exciton motion, the important parameters that can be extracted from Fig. 5.2 are an FWHM at RT of 180 meV and a standard deviation of 35 meV representing the potential fluctuation with a Gaussian distribution.

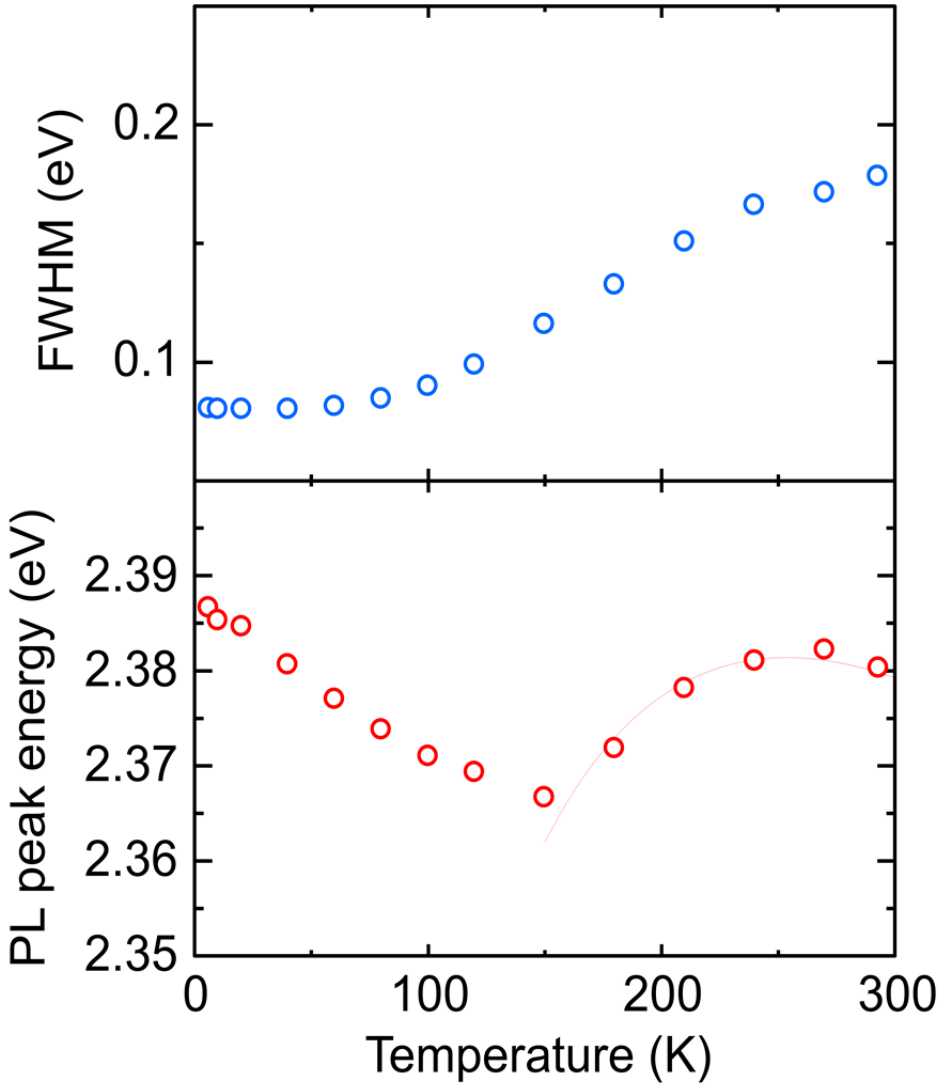

Figure 5.2 Temperature (T) dependences of PL FWHM and emission peak energy [$E(T)$] acquired macroscopically for a $\{20\bar{2}1\}$ SQW. The curve for the peak energy is the result of a fit with $E(T) = E(0) - \alpha T^2/(T+\beta) - \sigma^2/kT$, where α and β are parameters for describing the temperature dependence of the band gap, σ is the standard deviation representing potential fluctuation, and k is the Boltzmann constant.

Figure 5.3 displays the results of a SNOM PL mapping of the $\{20\bar{2}1\}$ SQW under the *I-C* mode. Figures 5.3(a) and (b) show the spatial distributions of the integrated intensity and peak wavelength, respectively. A y-shaped weak PL domain observed at the top center of Fig. 5.3 (a) does not have any physical meaning, but was used as an additional marker for pinpointing the precise location of the measurement area. The integrated PL intensity was distributed with island-like structures whose diameters were typically a few hundred nanometers. These sizes were almost comparable to the aperture diameter (150 nm) of the SNOM fiber probe. The ratio between the maximum and minimum integrated PL intensities was 4—much smaller than a previously reported value of about 200 for a (0001) SQW [22]. Furthermore, the spatial variation of PL peak wavelength was about 5 nm (Fig. 5.3(b))—much smaller than that in the (0001) SQW [22]. These results clearly indicate that the $\{20\bar{2}1\}$ SQW has a spatially more uniform potential distribution than the (0001) SQW. However, the PL peak wavelength shows stripe-like distributions along the $[\bar{1}2\bar{1}0]$ direction. Such a feature was not observed in the (0001) SQW, where the distribution was rather random, independent of the in-plane crystal direction. The origin of this distribution will be discussed below.

Although Figs. 5.3(a) and (b) do not imply correlation between the integrated PL intensity and the peak wavelength, Fig. 5.3(c) demonstrates the clear correlation between them, where the intensity decreases with increasing emission wavelength. This result suggests that In-rich InGaN areas accommodate more nonradiative recombination centers (NRCs), similar to the case in the (0001) QWs [22]. We have not, however, identified which defects are responsible for NRCs—line or point defects.

Figure 5.3(d) shows PL spectra acquired at positions A, B, C, and D, as marked in Fig. 5.3(a). Each spectrum is composed of a single emission peak, irrespective of the integrated PL intensity and the PL peak wavelength at the measurement position. The FWHMs range from 150 to 160 meV (30 to 35 nm), and are less than the macroscopic one (~180 meV), suggesting that potential fluctuations exist on the order of few hundreds nm and may cause carrier/exciton diffusion.

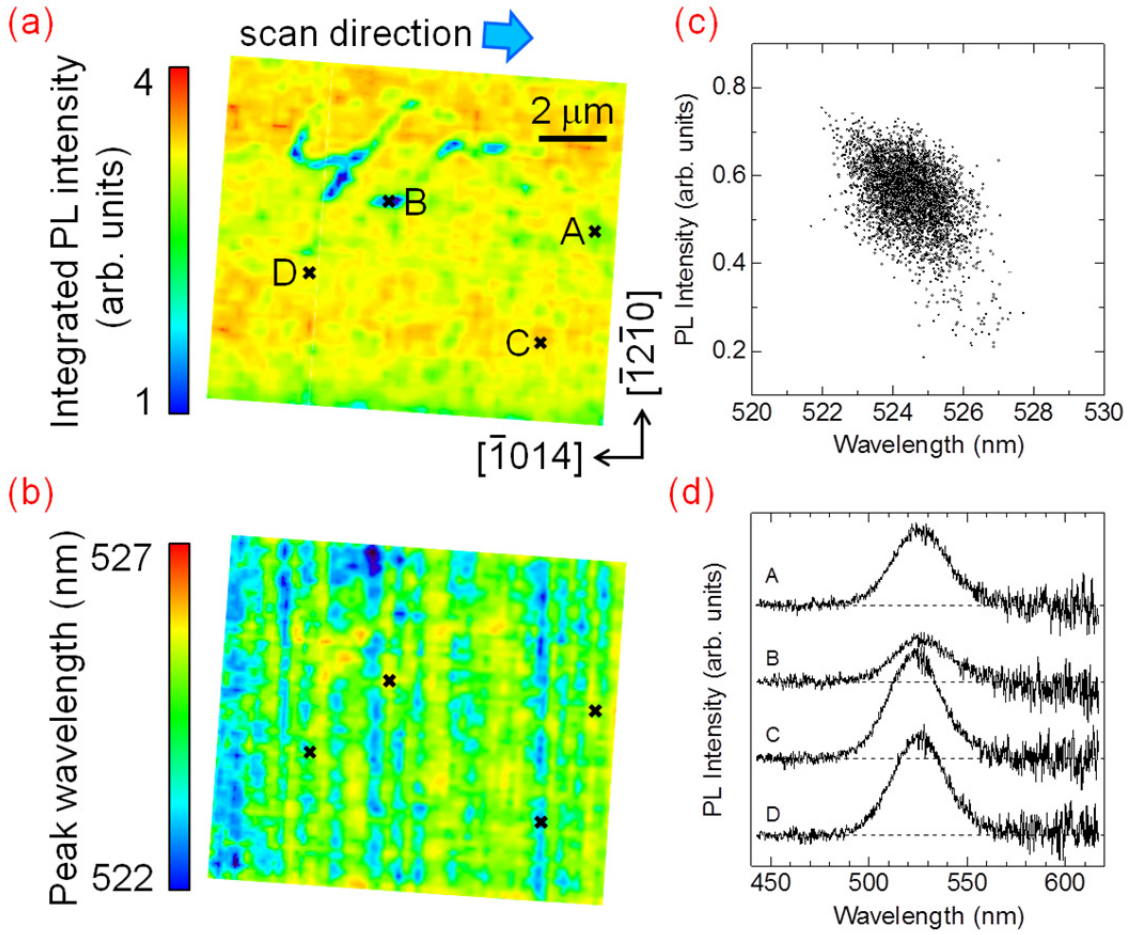

Figure 5.3 Spatial distributions of (a) integrated PL intensity and (b) PL peak wavelength in the {20$\bar{2}$1} InGaN SQW. (c) Integrated PL intensity as a function of the emission wavelength, and (d) PL spectra acquired at positions A, B, C, and D.

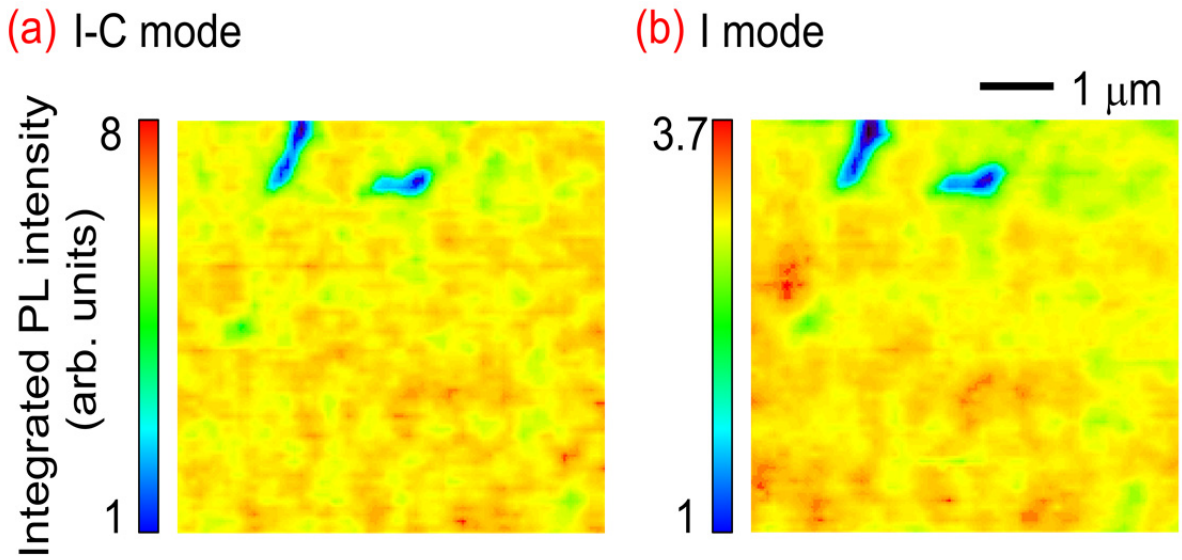

Figure 5.4 Integrated PL intensity maps taken by SNOM under the (a) *I-C* mode and (b) *I* mode.

To visualize lateral carrier diffusion directly in the $\{20\bar{2}1\}$ SQW, we performed multimode SNOM-PL measurements. Figures 5.4 (a) and (b) compare the spatial distribution of the integrated PL intensity in the $\{20\bar{2}1\}$ SQW acquired by the *I-C* and *I* modes, respectively. The size of the island-like structures in the *I-C* mode is ~300 nm in averaged diameter with a standard deviation of 120 nm [Fig. 5.4 (a)], whereas in the *I* mode, the island structures expand slightly, and consequently, fine structures observed in the *I-C* mode tend to disappear [Fig. 5.4 (b)]. This is due to the diffusion of carriers/excitons outside the probe aperture, where PL is detected in the far field by an objective lens in the *I* mode [20]. To quantify the diffusion length, we compared line profiles of the PL intensities taken under the *I-C* and *I* modes, and evaluated the difference. (See ref. [20] for the detailed procedure.) The

estimated diffusion lengths were ~70 nm along the $[\bar{1}014]$ direction and ~50 nm along the $[\bar{1}2\bar{1}0]$ direction. The anisotropic diffusion may originate from the anisotropic crystallographic geometry. PL FWHMs averaged over the maps in Figs. 5.4 (a) and (b) were 160 meV for the *I-C* mode and 150 meV for the *I* mode. The difference in the FWHMs in the *I-C* and *I* modes suggests that many of carriers/excitons diffuse outside the aperture toward lower energy potential minima. This is supported by a finding that the averaged PL energy is higher for the *I-C* mode (2.374 eV) than the *I* mode (2.338 eV). During the diffusion, carriers/excitons experience potential fluctuations with a standard deviation of 35 meV, as shown in Fig. 5.2. (A standard deviation of 35 meV corresponds to an FWHM of ~80 meV.)

It is interesting to note that the observed diffusion length is much shorter than that in a green-emitting (0001) SQW, which is a few hundred nm [22]. This finding is reasonable because, due to the reduced internal electric field, the PL lifetimes at RT are ~1 ns for the $\{20\bar{2}1\}$ SQW and ~40 ns for the (0001) SQW emitting at 520 nm. On the other hand, another semipolar QW of a $(11\bar{2}2)$ SQW has the shortest lifetime of ~200 ps at RT due to reduced electric fields, and consequently, shows the absence of carrier/exciton diffusion outside the probe aperture [23]. We have thus demonstrated that the carrier/exciton diffusion is governed by the carrier/exciton lifetime, and the $\{20\bar{2}1\}$ QWs exhibit intermediate properties, between polar (0001) and semipolar $(11\bar{2}2)$ QWs.

Finally, we discuss the origin of the characteristic distribution of PL peak wavelength of the $\{20\bar{2}1\}$ SQW shown in Fig. 5.3(b). Figure 5.5 shows (a) an AFM image, (b) spatial distribution of PL peak wavelength taken by the *I-C* mode SNOM in the identical area, and (c) the cross-sectional profiles of topography and PL peak wavelength extracted from black dashed lines in Figs. 5.5 (a) and (b). In the AFM topographic image, ridge structures are observable along the $[\bar{1}2\bar{1}0]$ direction. Similar topography has already been reported for $(20\bar{2}1)$ InGaN; it has been pointed out that the surface is composed of the $(10\bar{1}1)$ and $(10\bar{1}0)$ microfacets with widths of ~50 nm [24]. Note that $(10\bar{1}1)$ and $(10\bar{1}0)$ planes form angles of 13° and 15°, respectively, with respect to the $(20\bar{2}1)$ surface. In our SQW, on the other hand, although ridge structures are observed, the surface is quite smooth with a root mean square roughness of 0.74 nm, and is not likely to be composed of specific facets because tilting angles of the ridges are smaller than 0.5° with respect to the $\{20\bar{2}1\}$ surface,

as shown in Fig. 5.5 (c). A previous TEM observation supports this assertion [14]. Therefore, ridge structures along the $[\bar{1}2\bar{1}0]$ direction may be peculiar to the $\{20\bar{2}1\}$ plane, but their structure, such as heights and widths strongly depends on growth conditions.

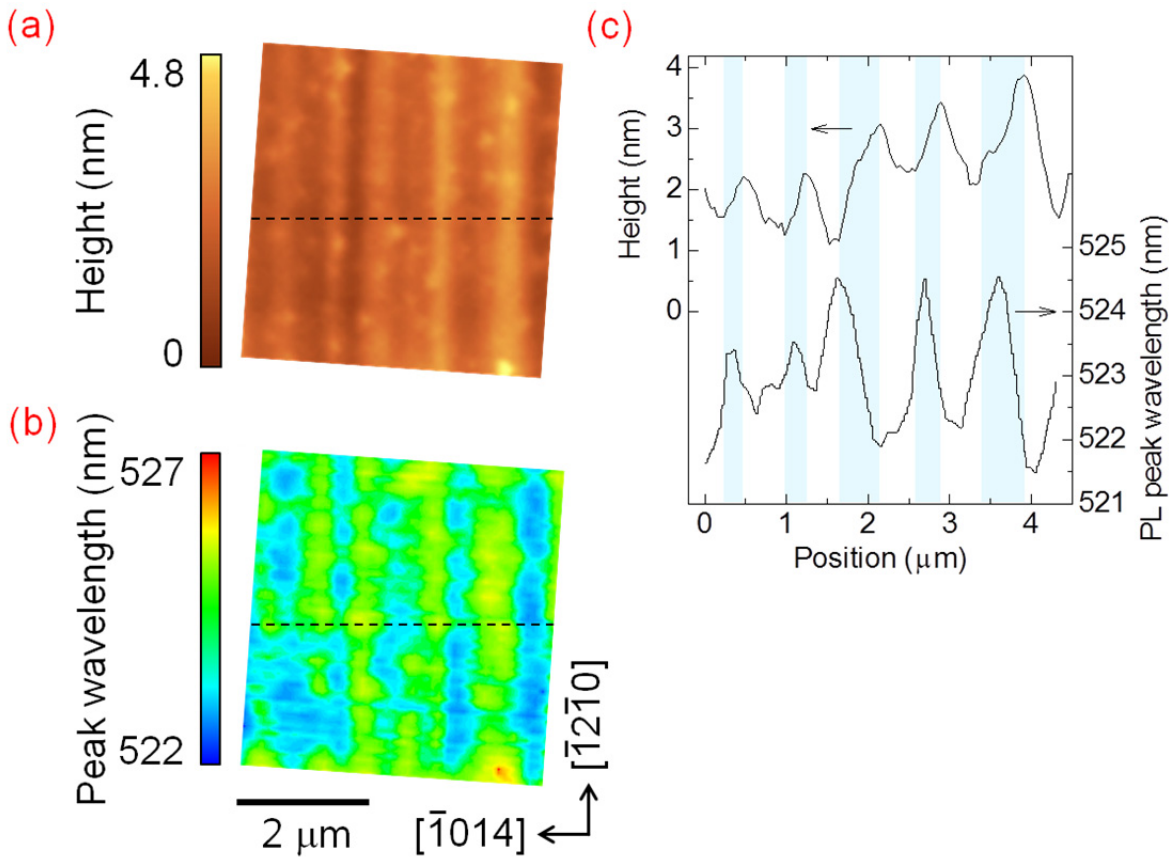

Figure 5.5 (a) An AFM image and (b) the spatial distribution of PL peak wavelength of the $\{20\bar{2}1\}$ InGaN SQW acquired over the same area. (c) A cross-sectional profile of the surface morphology and PL peak wavelength in the $\{20\bar{2}1\}$ InGaN SQW extracted from the dashed lines in (a) and (b). Blue shaded areas correspond to the *c*-plane side of the ridge structures.

Figures 5.5 (a) and (b) were acquired at the same position. The clear correlation is confirmed between them; the areas emitting at longer wavelengths almost correspond to the *c*-plane side of ridge structures. Therefore, the spatial variation of emission wavelength may be attributed to the difference of the In incorporation probability due to the small difference of the plane directions. Although such a variation of the emission wavelength exists, the quantified variations are as small as 4.2 meV along the $[\bar{1}014]$ direction and 2.6 meV along the $[\bar{1}2\bar{1}0]$ direction in terms of the standard deviation. Therefore, this does not worsen the homogeneity of the distribution of the PL peak wavelength, as well as the PL intensity, as demonstrated in Fig. 5.3 (a).

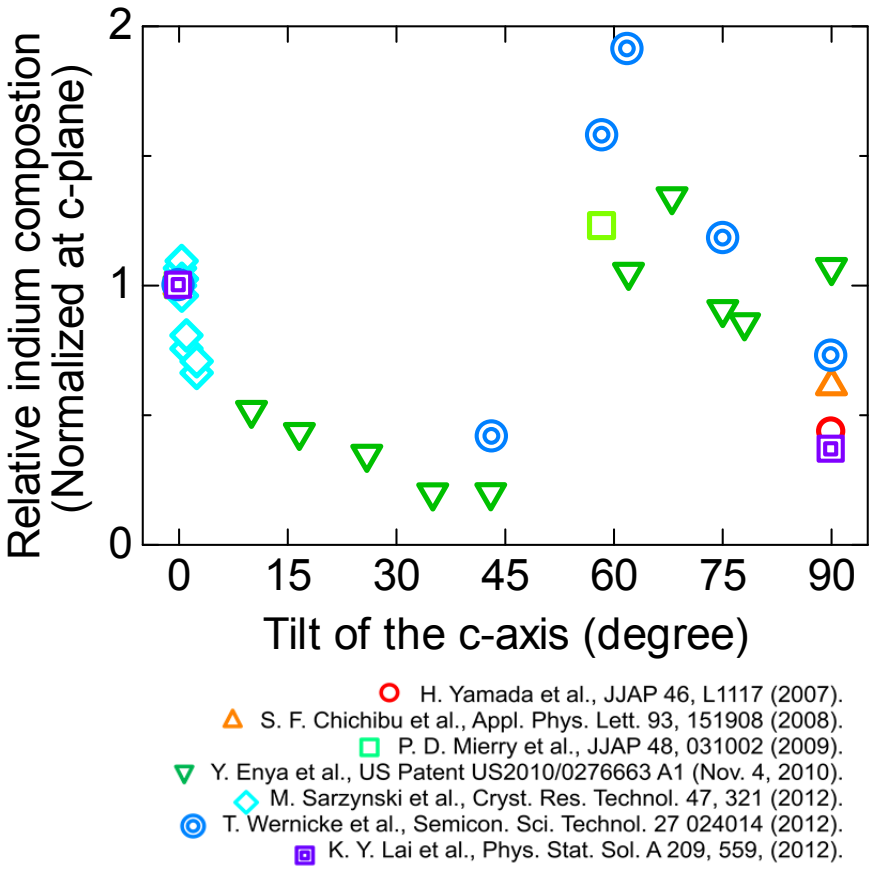

Figure 5.6 In incorporation efficiency with respect to tilt angles from c-orientation.

5.4 Summary

In summary, we have studied local PL characteristics in the $\{20\bar{2}1\}$ InGaN SQW by SNOM, detecting carrier/exciton diffusion from the fiber aperture of 150 nm. The estimated diffusion length is a few tens of nanometers—between those in $(11\bar{2}2)$ and (0001) InGaN QWs—and is well accounted for by the difference in carrier/exciton lifetimes. Furthermore, superimposing the SNOM-PL image with AFM image, clear correlation was observed between the spatial distributions of PL peak wavelength and surface morphology in the $\{20\bar{2}1\}$ SQW, where red-shifted PL peaks corresponded to the *c*-plane side of ridge structures.

References

1) S. Nakamura, S. Pearton, and G. Fasol, The Blue Laser Diode, 2nd ed. (Springer-Verlag, Heidelberg, 2000).

2) Y. Narukawa, M. Ichikawa, D. Sanga, M. Sano, and T. Mukai, *J. Phys. D* **43**, 354002 (2010).

3) Y. Narukawa, M. Sano, T. Sakamoto, T. Yamada, and T. Mukai, *Phys. Stat. Sol. A* **205**, 1081 (2008).

4) M. R. Krames, O. B. Shchekin, R. Mueller-Mach, G. O. Mueller, L. Zhou, G. Harbers, and M. G. Craford, *J. Disp. Techonol.* **3**, 160 (2007).

5) T. Miyoshi, S. Masui, T. Okada, T. Yanamoto, T. Kozaki, S. Nagahama, and T. Mukai, *Appl. Phys. Exp.* **2**, 062201 (2009).

6) I.-h. Ho and G. B. Stringfellow, *Appl. Phys. Lett.* **69**, 2701 (1996).

7) S. Chichibu, T. Azuhata, T. Sota, and S. Nakamura, *Appl. Phys. Lett.* **69**, 4188 (1996).

8) T. Takeuchi, S. Sota, M. Katsuragawa, M. Komori, H. Takeuchi, H. Amano, and I. Akasaki, *Jpn. J. Appl. Phys.* **36**, L382 (1997).

9) T. Takeuchi, H. Amano, and I. Akasaki, *Jpn. J. Appl. Phys.* **39**, 413 (2000).

10) M. Funato, A. Kaneta, Y. Kawakami, Y. Enya, K. Nishizuka, M. Ueno, and T. Nakamura, *Appl. Phys. Exp.* **3**, 021002 (2010).

11) T. Wernicke, L. Schade, C. Netzel, J. Rass, V. Hoffmann, S. Ploch, A. Knauer, M. Weyers, U. Schwarz, and M. Kneissl, *Semicond. Sci. Technol.* **27**, 024014 (2012).

12) K. Okamoto, J. Kashiwagi, T. Tanaka, and M. Kubota, *Appl. Phys. Lett.* **94**, 071105 (2009).

13) M. Funato, M. Ueda, Y. Kawakami, Y. Narukawa, T. Kosugi, M. Takahashi, and T. Mukai, *Jpn. J. Appl. Phys.* **45**, L659 (2006).

14) Y. Enya, Y. Yoshizumi, T. Kyono, K. Akita, M. Ueno, M. Adachi, T. Sumitomo, S. Tokuyama, T. Ikegami, K. Katayama, and T. Nakamura, *Appl. Phys. Exp.* **2**, 082101 (2009).

15) Y. Yoshizumi, M. Adachi, Y. Enya, T. Kyono, S. Tokuyama, T. Sumitomo, K. Akita, T. Ikegami, M. Ueno, K. Katayama, and T. Nakamura, *Appl. Phys. Exp.* **2** 092101 (2009).

16) S. Takagi, Y. Enya, T. Kyono, M. Adachi, Y. Yoshizumi, T. Sumitomo, Y. Yamanaka, T. Kumano, S. Tokuyama, K. Sumiyoshi, N. Saga, M. Ueno, K. Katayama, T. Ikegami, T. Nakamura, K. Yanashima, H. Nakajima, K. Tasai, K. Naganuma, N. Fuutagawa, Y. Takiguchi, T. Hamaguchi, and M. Ikeda, *Appl. Phys. Exp.* **5**, 082102 (2012).

17) K. Yanashima, H. Nakajima, K. Tasai, K. Naganuma, N. Fuutagawa, Y. Takiguchi, T. Hamaguchi, M. Ikeda, Y. Enya, S. Takagi, M. Adachi, T. Kyono, Y. Yoshizumi, T. Sumitomo, Y. Yamanaka, T. Kumano, S. Tokuyama, K. Sumiyoshi, N. Saga, M. Ueno, K. Katayama, T. Ikegami, and T. Nakamura, *Appl. Phys. Exp.* **5**, 082103 (2012).

18) I. L. Koslow, J. Sonoda, R. B. Chung, C. -C. Pan, S. Brinkley, H. Ohta, S. Nakamura, and S. P. DenBaars, *Jpn. J. Appl. Phys.* **49**, 080203 (2010).

19) Y. S. Kim, A. Kaneta, M. Funato, Y. Kawakami, T. Kyono, M. Ueno, and T. Nakamura, *Appl. Phys. Exp.* **4**, 052103 (2011).

20) A. Kaneta, T. Mutoh, G. Marutsuki, Y. Narukawa, T. Mukai, Y. Kawakami, and Sg. Fujita, *Appl. Phys. Lett.* **83**, 3462 (2003).

21) K. Kazlauskas, G. Tamulaitis, P. Pobedinskas, A. Žukauskas, M. Springis, C.-F. Huang, Y.-C. Cheng, and C. C. Yang, *Phys. Rev. B* **71**, 085306 (2005).

22) A. Kaneta, M. Funato, and Y. Kawakami, *Phys. Rev. B* **78**, 125317 (2008).

23) Y. Kawakami, K. Nishizuka, D. Yamada, A. Kaneta, M. Funato, Y. Narukawa, and T. Mukai, *Appl. Phys. Lett.* **90**, 261912 (2007).

24) S. Ploch, T. Wernicke, J. Thalmair, M. Lohr, M.Pristovsek, J. Zweck, M. Weyers, and M. Kneissl, *J. Cryst. Growth,* **356**, 70 (2012).

25) H. Yamada, K. Iso, M. Saito, K. Fujito, S. P. DenBaars, J. S. Speck, and S. Nakamura, *Jpn. J. Appl. Phys.* **46**, L1117 (2007).

26) S. F. Chichibu, H. Yamaguchi, L, Zhao, M. Kubota, T. Onuma. K. Okamoto, and H. Ohta, *Appl. Phys. Lett.* **93**, 151908 (2008).

27) Y. Enya, Y. Yoshizumi, M. Ueno, K. Akita, T. Kyono, T. Sumitomo, T. Nakamura, US Patent Us2010/0276663 A1 (Nov. 4, 2010).

28) M. Sarzynski, M. Leszczynski, M. Krysko, J. Z. Domagala, R. Czernecki, and T. Suski, *Cryst. Res. Technol.* **47**, 321 (2012).

29) K.Y. Lai, T. Paskova, V. D. Wheeler, T. Y. Chung, J. A. Grenko. M. A. L. Johnson, K. Udwary, E. A. Preble, and K. R. Evans, *Phys. Stat. Sol. A* **209**, 509 (2012).

Chapter 6.

Optical Gain Properties of Semipolar {20$\bar{2}$1} Green InGaN Laser Diodes

6. 1 Introduction

As discussed in Chapter 5, green QWs on semipolar {20$\bar{2}$1} plane show good homogeneous luminescence properties and anisotropy as suggested by comparison of AFM and SNOM measurements. In this chapter, we characterize optical gain properties of semipolar {20$\bar{2}$1} green LDs. Reaching the green spectral region without degrading the performance remains a challenge because higher In compositions are necessary for longer emission wavelengths. Higher In compositions strengthen the internal electric fields owing to piezoelectric polarization [3,4] and make the uniform growth of InGaN QWs difficult [5]. Although InGaN QWs grown on semipolar planes may reduce the internal electric fields,[3,4,6,7] these QWs require higher In compositions than the conventional (0001) QWs to achieve the same emission wavelength. These conditions give rise to a competition between the planes. In fact, green LDs have been demonstrated on the polar (0001) [8,9] and semipolar {20$\bar{2}$1} planes [10,11]. Remarkably, the threshold current density (J_{th}) of {20$\bar{2}$1} LDs was found to be lower [11] because of the reduced internal electric fields and increased uniformity of the semipolar InGaN QW [10,12].

Another important factor is current injection. For LEDs, an “efficiency droop” under a high injection current has often been reported [13]. Although the mechanism is uncertain, the droop is stronger in longer-wavelength emitters and may affect gain formation in green LDs because the material gain is proportional to the radiative recombination probability. Furthermore, gain suppression under a high injection current has been observed for (0001)

blue-green and cyan LDs [14-16]. In this study, we investigate the current dependence of the gain spectra in a semipolar $\{20\bar{2}1\}$ green LD.

6.2 Experiments

An epitaxial wafer was processed into ridge-stripe LDs with a 600-μm-long cavity and a 2-μm-wide ridge. The optical gain spectra were extracted from the EL spectra using Hakki and Paoli's scheme [17,18]. This scheme requires the longitudinal modes in our green LD, which have a period of ~80 pm, to be well resolved. Therefore, we dispersed the EL with a 1 m monochromator with a resolution of 10 pm. The LD was driven by a 10 kHz pulsed current with a duty of 5%. A boxcar gate integrator was employed to detect EL, and to extract the stable current region within each pulse. Its gate width was 20% of the pulse width. Pulse operation sometimes causes instable longitudinal modes and increases noise levels in the extracted gain spectra. However, preliminary experiments using conventional (0001) LDs confirmed that the present measurement conditions provide gain spectra almost identical to those obtained by CW operation when the gate width, gate position, and integration time are appropriately adjusted. All measurements were performed at room temperature.

6.2.1 Gain measurement under pulsed operation

As explained in Chapter 4, since the Hakki-Paoli method requires stable lasing operation for higher accuracy, it is desirable to perform measurements under CW operation. However, we would want to know the gain of the diode during development stage. For such cases, LDs are usually operated under pulsed condition because of their low stability, and issues with thermal dissipation. Generally, the electron density in not constant under the pulsed current injection condition, and the longitudinal modes of LDs are not clear. Therefore, the optical gain determined from EL spectrum is also significantly influenced. Figure 6.1 displays a schematic of the gain reduction model. In this study, we have demonstrated that even under pulsed current operation optical gain can be measured successfully by introducing a boxcar

gate integrator. The working principle of a boxcar gate integrator is simple. We can adjust its gate width to obtain the signal from the detector only within the desired temporal region.

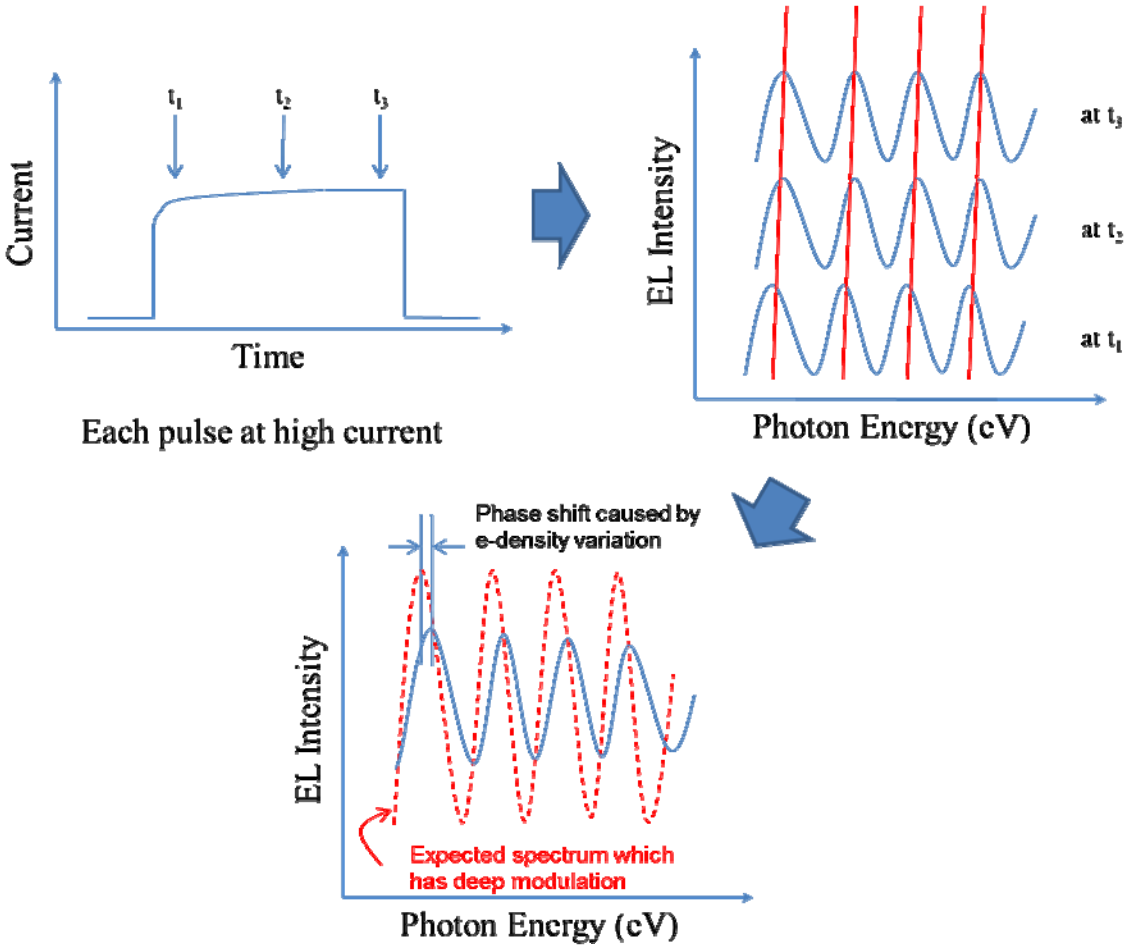

Figure 6.1 Schematic model for gain reduction under pulsed operation.

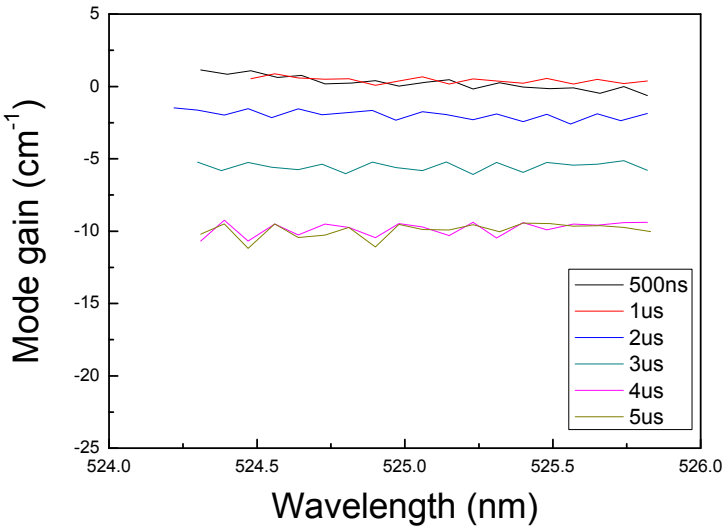

Figure 6.2 Gate width optimization for optical mode gain measurement.

Thus, undesirable non-uniform signal originating from the instability of the pulsed current source can be eliminated. Experimental results used to determine the optimized gate width for gain measurement, are shown in Fig. 6.2. The EL spectrum is measured near peak gain, just below the threshold current. Consequently, optical mode gain is 0 if the measurement is performed as usual. Thus, gain measurement under pulsed operation is setup by optimizing the width and position of the boxcar gate integrator.

6.3 Lasing property and the current dependent optical mode gain

Fig. 6.3 shows the EL spectra for spontaneous and stimulated emissions at $0.003J_{th}$ and $1.12J_{th}$, respectively, where J_{th} is 5.4 kA/cm^2. These spectra were acquired using another low-resolution spectrometer without resolving the longitudinal modes. Narrow and strong lasing was confirmed at 527 nm above J_{th}. The peak energy difference between the spontaneous and stimulated emissions was found to be ~190 meV. Three major factors contribute to the energy shift: QCSE due to the built-in potential in the *pn* junction, filling of tail states, and free-carrier screening of the polarization-induced electric field. Unlike (0001) LDs, which have a

greater contribution from the state-filling effect [14], the observed peak shift in the $\{20\bar{2}1\}$ LD is mainly derived from the *pn* built-in potential, as discussed below.

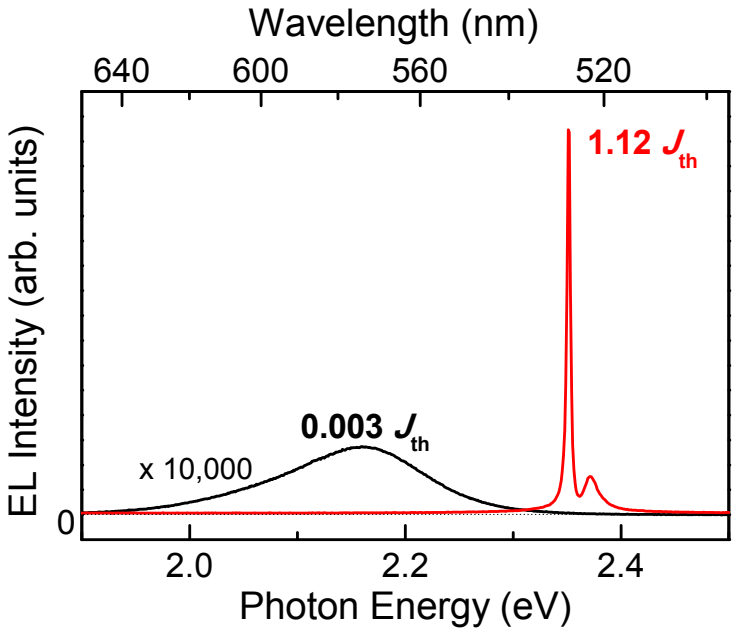

Figure 6.3 EL spectra of spontaneous ($0.003J_{th}$) and stimulated ($1.12J_{th}$) emissions for the $\{20\bar{2}1\}$ green LD.

Figure 6.4(a) shows the measured high-resolution EL spectrum at 65 mA just below the threshold current. Longitudinal modes with a period of ~80 pm are clearly resolved. These fine structures, which are observed for different driving currents, enable us to evaluate the current dependence of mode gain spectra. Figure 6.4(b) displays the obtained mode gain spectra. On the lower energy side, the gain is constant and corresponds to the internal loss. The reason for the variation of the estimated internal loss due to the injection current is unclear and we simply conclude that the internal loss of the $\{20\bar{2}1\}$ green LD is 20±5 cm^{-1},

which is comparable to that of an LD on the (0001) plane lasing at 470 nm [15]. (hereafter, this (0001) LD is referred to as 470LD).

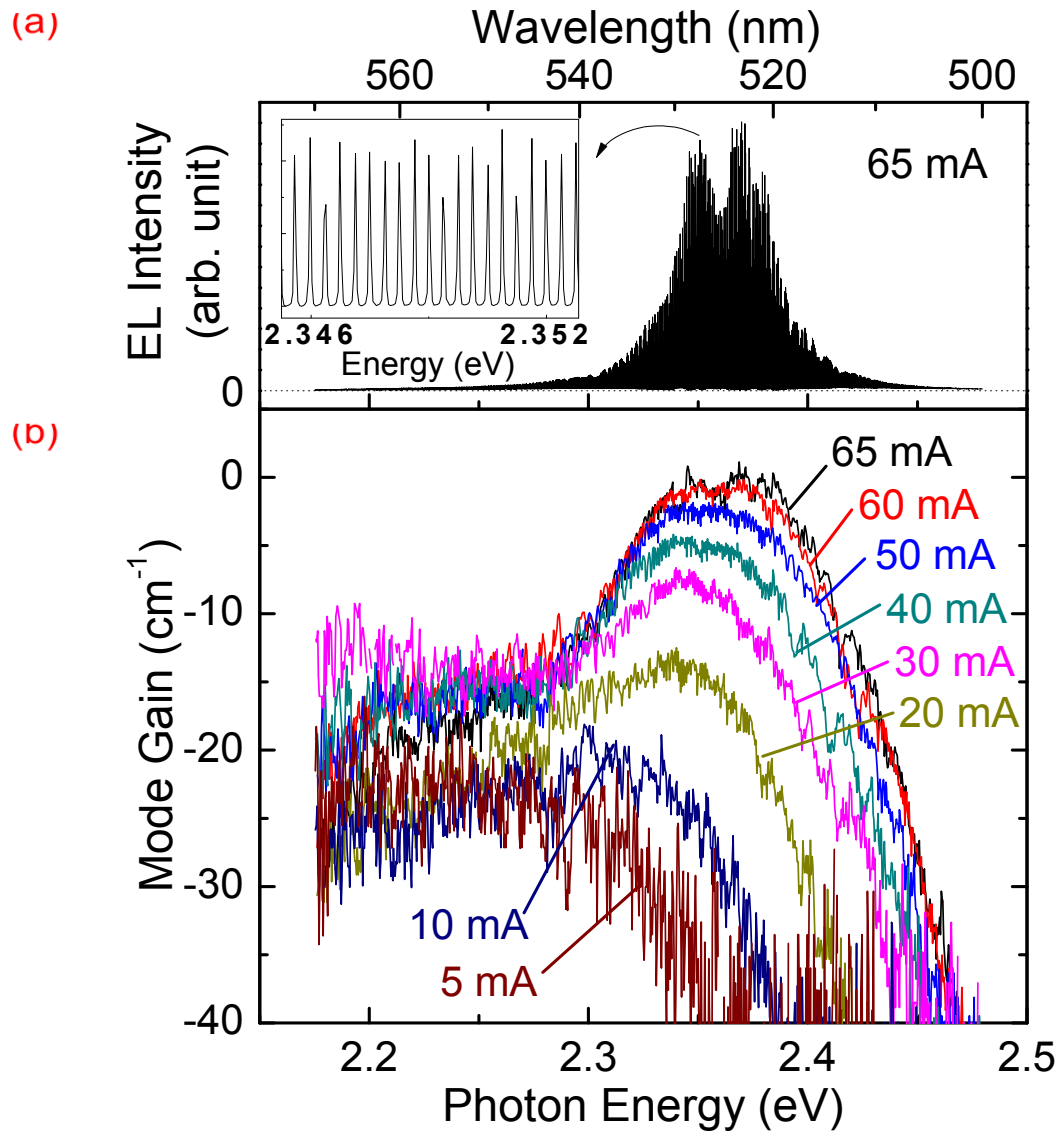

Figure 6.4 (a) EL spectrum of the $\{20\bar{2}1\}$ green LD acquired just below the threshold current with a high spectral resolution. Inset indicates well-resolved longitudinal modes used to extract the gain spectra. (b) Current-dependent gain spectra obtained from the EL spectra.

6.4 Gain suppression and carrier density dependence of EL and gain peak energy

From the gain spectra, the maximum gain and gain peak are analyzed as functions of the injection current density. Figure 6.5(a) shows the variation of the maximum mode gain where the reported results for LDs on the (0001) planes [15] are plotted for comparison. For the (0001) LD emitting at 404 nm (404LD), the maximum gain linearly increases with injection current, but becomes saturated for LDs emitting at a longer wavelength of 440 (440LD) or 470 nm (470LD). This observation suggests the presence of gain suppression mechanisms such as potential fluctuations [14], non-radiative recombination [19], Auger recombination, and current overflow, which are key factors for the efficiency droop phenomena in LEDs [13].

The $\{20\bar{2}1\}$ green LD behaves similar to 440LD and 470LD, but its gain saturation is not so significant as a cyan LD (490 nm) on the (0001) plane reported in Ref. [16]. It should be noted that, although potential fluctuations are considered to be responsible for the gain saturation in (0001) LDs, [14,16] those may have minor effects in $\{20\bar{2}1\}$ LDs, as discussed below. Therefore, to lower J_{th}, the cause of this saturation must be clarified and addressed by, for example, further optimization of epitaxial layer structures in future studies. Figure 6.5(b) compares the gain peak shift of the $\{20\bar{2}1\}$ green LD to that of 470LD on the (0001) plane. The energy shift is much smaller for the $\{20\bar{2}1\}$ green LD.

To analyze the peak shift due to injection current, inhomogeneous broadening is initially estimated from the photoluminescence (PL) of undoped InGaN QWs. The (0001) QW is identical to 470LD but without a *pn* junction, while the $\{20\bar{2}1\}$ QW was grown on a GaN substrate under the same condition as that for the active region of the $\{20\bar{2}1\}$ green LD. Thus, a contribution from the *pn* built-in potential can be excluded. PL is excited by a frequency-doubled Ti:sapphire laser emitting at 400 nm with a pulse width of 1.5 ps. Figure 6.6 shows the PL peak shift as a function of the photoexcited initial carrier density. To reproduce the experimental results, both state-filling and screening of the polarization field are considered.

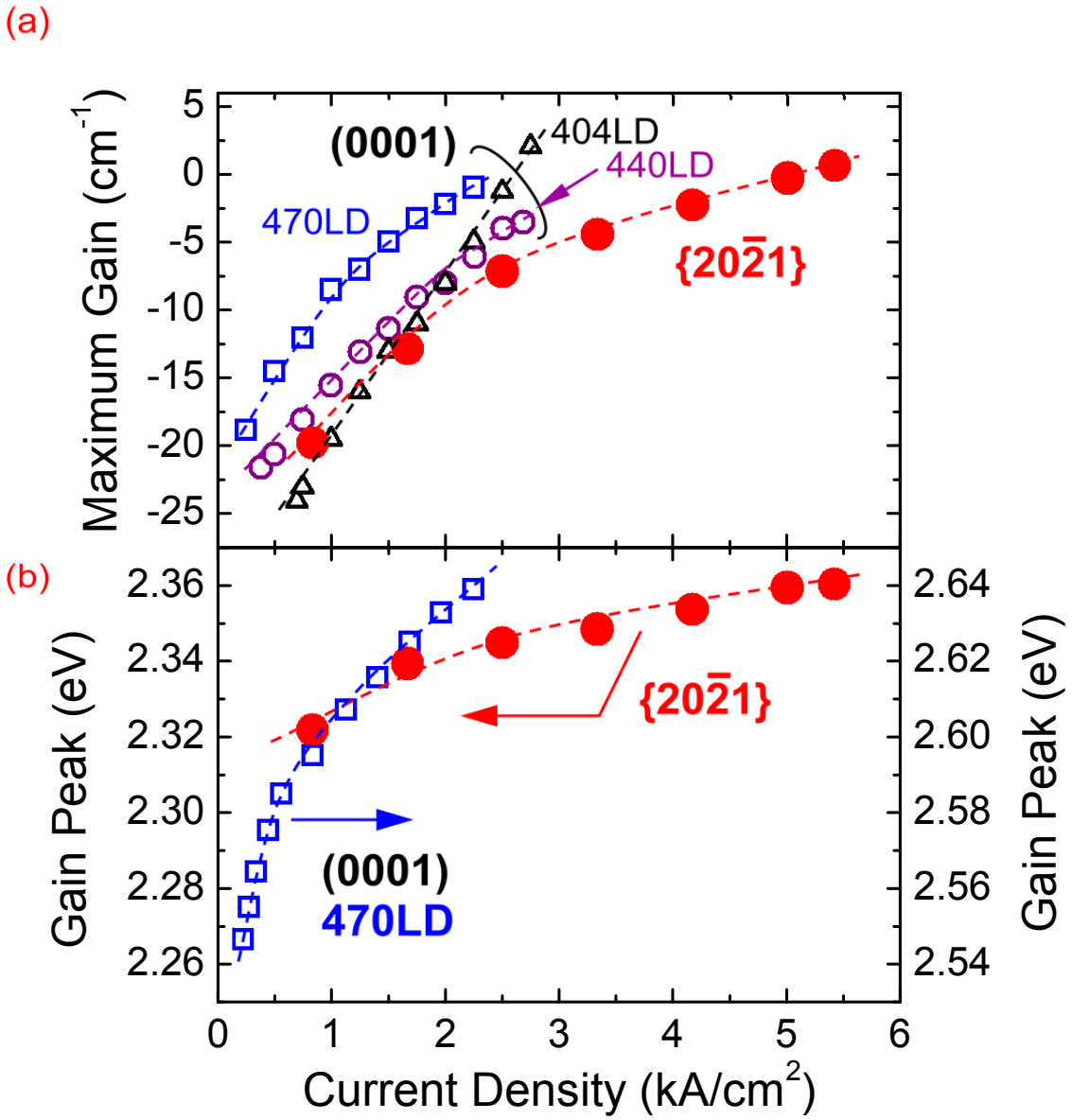

Figure 6.5 (a) Maximum gain and (b) gain peak position of the {20$\bar{2}$1} green LD and reference (0001) LDs as functions of injection current density. All lines are guides to the eyes.

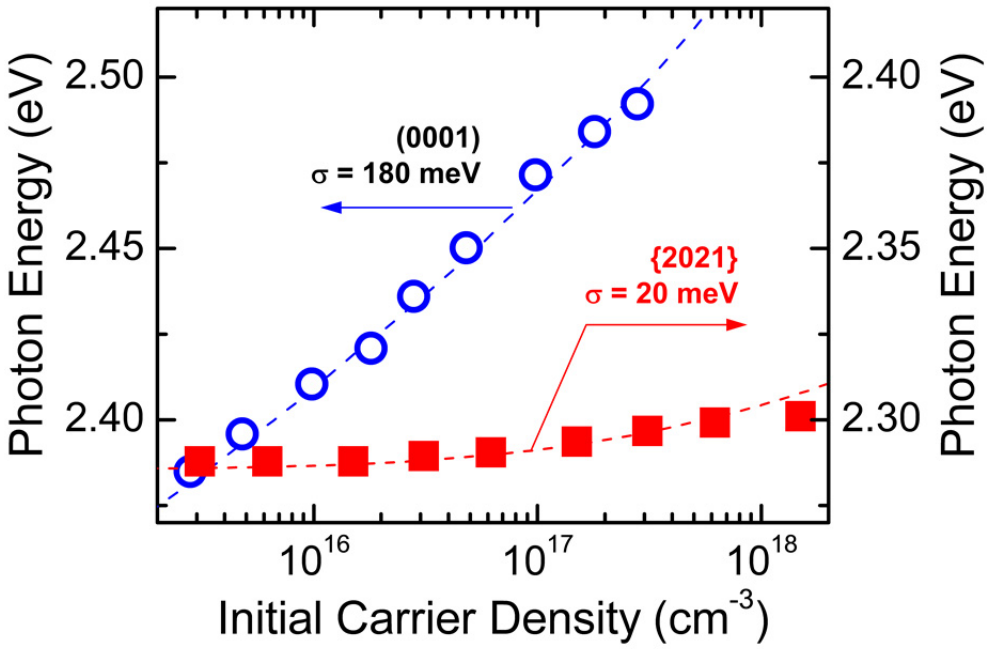

Figure 6.6 PL peak shifts in QWs frown on the $\{20\bar{2}1\}$ and (0001) planes as functions of photoexcited initial carrier density. The QWs are undoped, so that the effects of *pn* junctions are excluded. Symbols represent experimental results (open circle: 470 nm LD structure, closed square: semipolar $\{20\bar{2}1\}$ green QW), while dashed lines indicate the fitting results, σ is the estimated inhomogeneous broadening.

To quantify the state-filling effect, the potential fluctuations are expressed by convoluting the density of states of ideal QWs (that is, a step function) with a Gaussian distribution. One fitting parameter is the standard deviation (σ) of the Gaussian distribution, which defines inhomogeneous broadening. On the other hand, to quantify the screening effect, one-dimensional Schrödinger and Poisson equations are solved self-consistently, assuming that the internal piezoelectric fields (E_{pz}) are 0.77 MV/cm for the $\{20\bar{2}1\}$ QW and –2.1 MV/cm for the (0001) QW [21]. The total peak shift is evaluated by summing those two contributions.

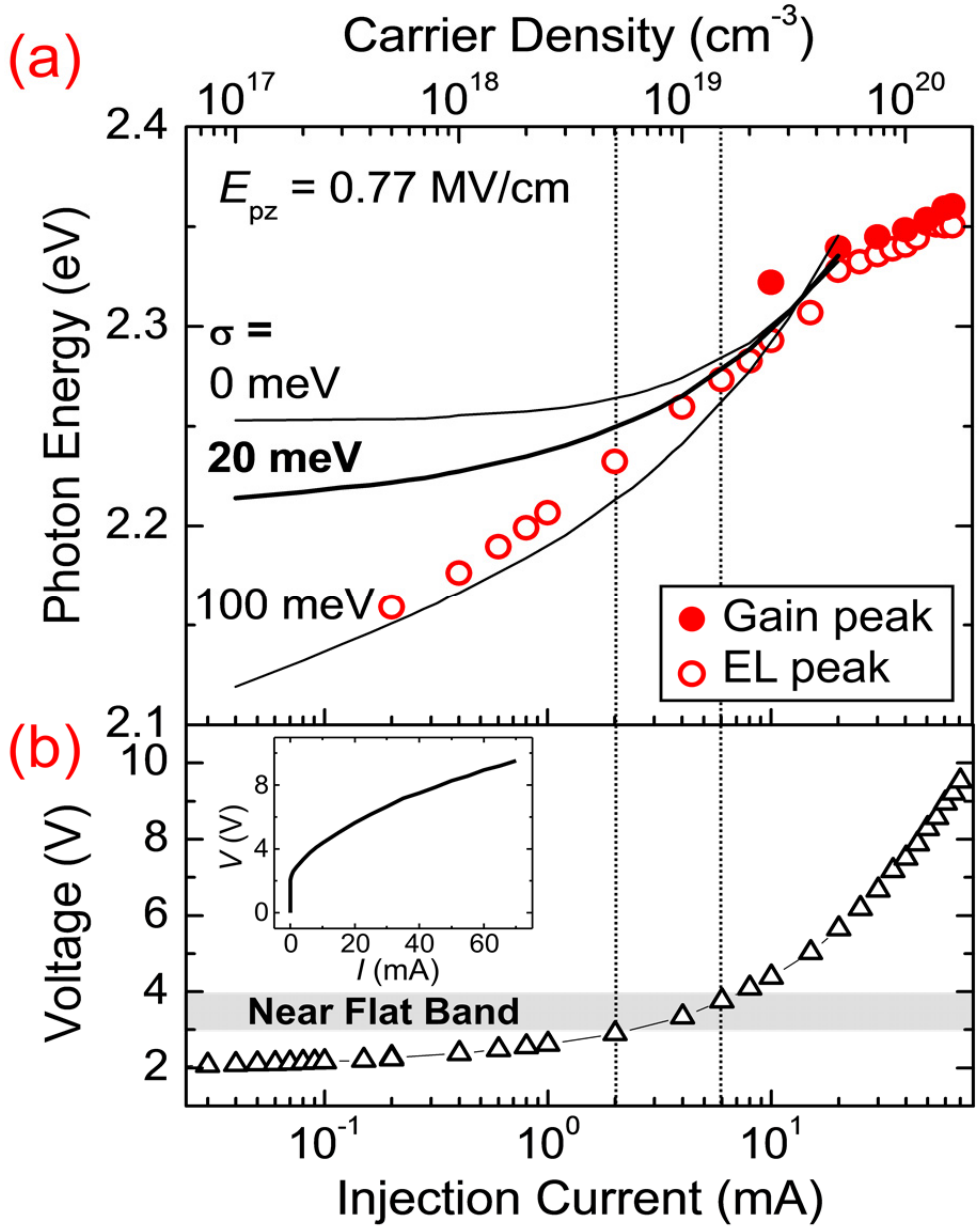

Figure 6.7 (a) EL (open circle) and gain (closed circle) peak shifts as functions of the injection current, and comparison with calculation after considering inhomogeneous broadening and screening of the piezoelectric polarization. (b) I-V curve fir the $\{20\bar{2}1\}$ green LD. Inset is that on the linear scale.

The dashed lines in Fig. 6.6 indicate that the σ values are 20 meV for the $\{20\bar{2}1\}$ green QW and 180 meV for the (0001) blue QW. The inhomogeneous broadening in the $\{20\bar{2}1\}$ QW is well suppressed, which is suitable for better differential gain properties [15] and consistent with earlier reports [10,12]. By using the estimated σ value, the gain and EL peak energy shifts due to the injection current are examined for the $\{20\bar{2}1\}$ green LD. Figure 6.7 plots the experimental results using closed (gain) and open (EL) circles. The shifts behave quite similarly, suggesting they are governed by the same physics. The lines in Fig. 6.7(a) are calculated using the same procedure as in Fig. 6.6. For the calculation, carrier density, not current, is necessary. To relate the carrier density and current density to each other, time-resolved PL measurements are performed using the same laser as in Fig. 6.3 and a streak camera. For initial photoexcited carrier densities between 1×10^{18} and 1×10^{20} cm^{-3}, an almost constant carrier lifetime of 1.5 ns is estimated, while the internal quantum efficiency derived from PL intensity ratio between room and low temperatures is ~30%. Therefore, the carrier density is simply assumed to be the product of the carrier lifetime (1.5 ns) and injection current density. It is noteworthy that the obtained carrier density can be overestimated because properties peculiar to the current injection are not involved in PL. For a more accurate estimate, EL lifetime measurements are in progress.

Figure 6.7(a) shows that σ = 20 meV and E_{pz} = 0.77 MV/cm provide a fairly good fit in a current regime of 3 to 20 mA. Above 20 mA, the experimental peaks are at lower energies than the theoretical prediction. One possible interpretation is a sublinear increase in the net carrier density in the QW with the injection current, and may be related to the gain suppression observed in Fig. 2. Bandgap renormalization is another possible factor [21].

For injection currents below 3 mA, the experimental and calculated peak shifts drastically differ due to the built-in potential of the *pn* junction. Figure 6.7(b) shows the current-voltage (*I-V*) characteristic. The turn-on voltage (3-4 V) determined in the inset suggests that an injection current of ~4 mA realizes a nearly flat band condition. Therefore, when the injection current is less than ~4 mA, which is the current regime of interest, the *pn* built-in potential remains, leading to the QCSE. On the $\{20\bar{2}1\}$ plane, the QCSE under a forward bias induces a blue shift because the polarization field is in the same direction as the *pn* built-in field. A preliminary device simulation predicts that the blue shift due to the QCSE is ~50 meV when the current is increased from 0.2 and 5 mA (not shown). The predicted shift of ~50 meV superimposes on those due to state filling and free-carrier screening and

reasonably explains the difference between the experiments and calculation revealed in Fig. 6.7(a).

It is noteworthy that the direction of the polarization-induced electric field is opposite for devices on the (0001) plane. Therefore, the QCSE under forward bias induces a "red shift" for (0001) devices [22]. In fact, unlike the $\{20\bar{2}1\}$ LD, the EL peak energy of the 470LD is higher than the theoretical prediction under a low bias condition. This finding further supports the present interpretation of a peak shift in the low current regime. In spite of the red shift due to the QCSE, the total blue shift of the (0001) LDs is more significant than that of the $\{20\bar{2}1\}$ green LD as demonstrated in Figs. 6.5 and 6.6 due to the much greater inhomogeneous broadening.

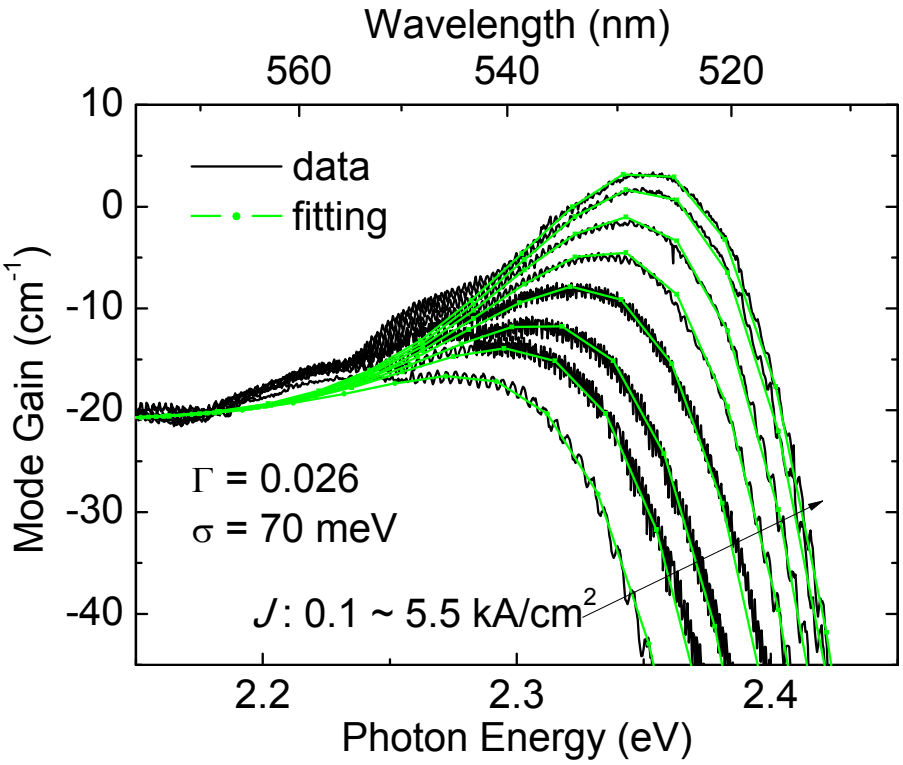

Figure 6.8 Current dependent optical mode gain spectra and fitting results.

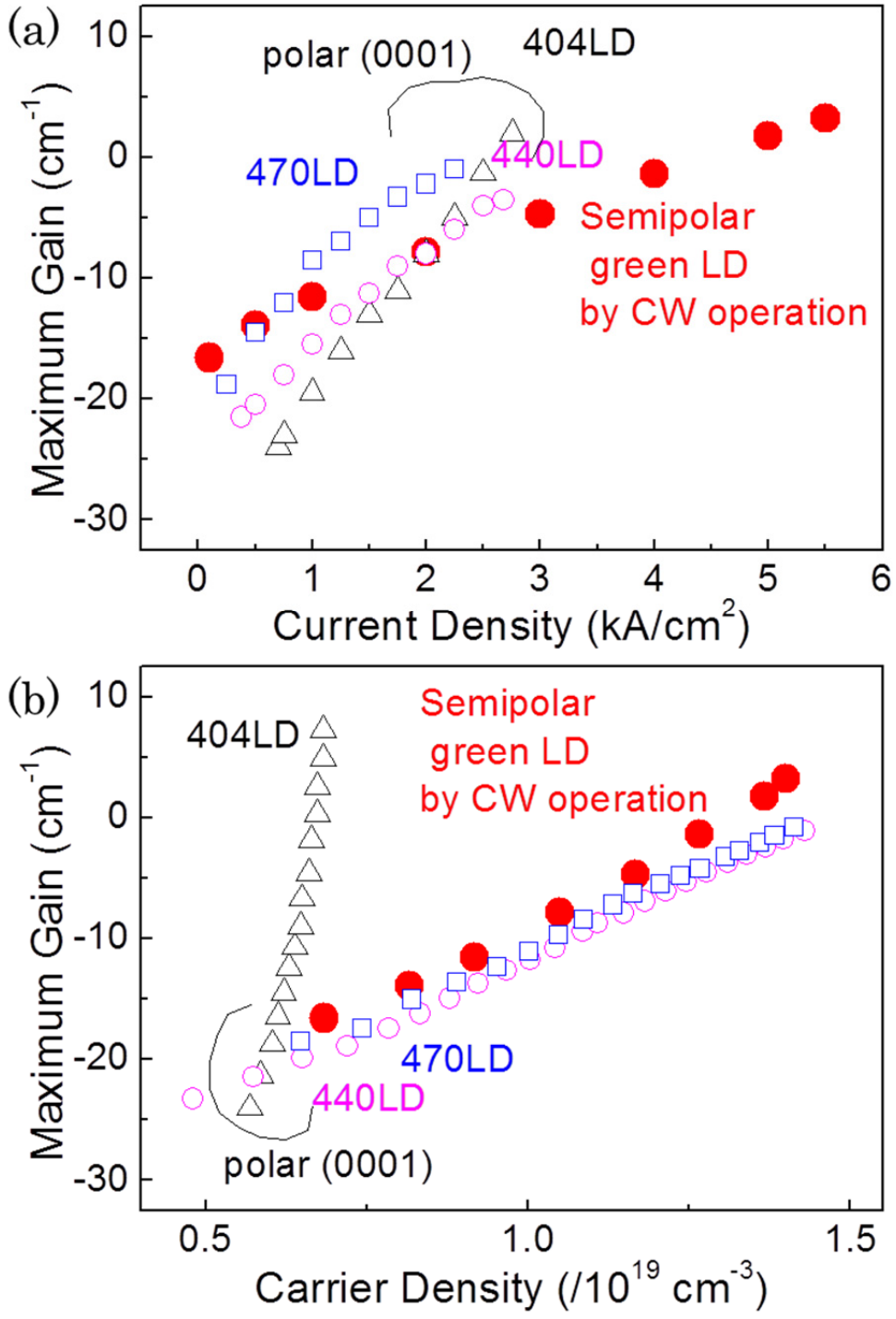

Figure 6.9 (a) maximum gain plots as functions of current density (kA/cm^2), and (b) as functions of carrier density (/10^{19} cm^{-3})

6.5 Recent achievement: CW operation and gain measurement

Semipolar $\{20\bar{2}1\}$ green LDs until section 6.4 are still under development so their characterization was performed under pulsed current operation. Recently advanced device have been developed by the improvement in epitaxial techniques and processes. These can be operated by CW current injection. This section introduces recent results for these devices.

The threshold current density is approximately 5.6 kA/cm^2. Figure 6.8 shows the current dependent mode gain measured with a CCD detector, which has 1024 pixels.

Comparing with Fig. 6.4 the signal to noise ratio of the new device shows improvement and the internal loss is seen to have decreased to ~20/cm. To compare maximum gain with the same physical quantity of carrier density, the relation between the injection current density and carrier density was determined using the gain fit in Fig. 6.8, similar to the discussion in Chapter 4. Figure 6.9(a) displays the results as functions of current density measured data. On the other hand, Fig. 6.9(b) represents the results as functions of carrier density. As we can notice in the Fig. 6.9 the slope of maximum gain is not saturated in semipolar $\{20\bar{2}1\}$ green LD. Note, although operating current density of semipolar $\{20\bar{2}1\}$ green LD is higher than those of shorter wavelength LDs on polar (0001) planes, carrier density is similar to those of shorter wavelength LDs and smaller than that of polar (0001) green LD. This presents that the gain of semipolar $\{20\bar{2}1\}$ green LD is larger than that of polar (0001) green LD most likely due to improved overlap between electron and hole wavefunctions. [See Eqs. (2.23) and (2.24).]

6.6 Summary

The optical gain characteristics are assessed for the $\{20\bar{2}1\}$ green LD. The estimated internal loss (20 ± 5 cm^{-1}) is comparable to those of the matured (0001) LDs. Similarly to conventional (0001) LDs emitting blue or longer wavelengths, as the injection current increases, the maximum gain becomes saturated, suggesting gain suppression mechanisms. The gain and emission peak shifts are reasonably explained on the basis of the QCSE due to the *pn* built-in potential, state filling, and screening of polarization-induced electric fields. Particularly, tail states in the $\{20\bar{2}1\}$ LD are much less than those in (0001) LDs, and therefore, to suppress the gain saturation, other mechanisms have to be considered.

References

1) S. Nagahama, T. Yanamoto, M. Sano, and T. Mukai, *Jpn. J. Appl. Phys.* **40**, 3075 (2001).

2) Y. Narukawa, M. Ichikawa, D. Sanga, M. Sano, and T. Mukai, *J. Phys. D: Appl. Phys.* **43**, 354002 (2010).

3) T. Takeuchi, S. Sota, M. Katsuragawa, M. Komori, H. Takeuchi, H. Amano, and I. Akasaki, *Jpn. J. Appl. Phys.* **36**, L382 (1997).

4) S.-H. Park and S.-L. Chuang, *Phys. Rev. B* **59**, 4725 (1999).

5) I.-h. Ho and G. B. Stringfellow, *Appl. Phys. Lett.* **69**, 2701 (1996).

6) K. Nishizuka, M. Funato, Y. Kawakami, S. Fujita, Y. Narukawa, and T. Mukai, *Appl. Phys. Lett.* **85**, 3122 (2004).

7) M. Funato, M. Ueda, Y. Kawakami, Y. Narukawa, T. Kosugi, M. Takahashi, and T. Mukai, *Jpn. J. Appl. Phys.* **45**, L659 (2006).

8) T. Miyoshi, S. Masui, T. Okada, T. Yanamoto, T. Kozaki, S. Nagahama, and T. Mukai, *Appl. Phys. Exp.* **2**, 062201 (2009).

9) A. Avramescu, T. Lermer, J. Müller, C. Eichler, G. Bruederl, M. Sabathil, S. Lutgen, and U. Strauss, *Appl. Phys. Exp.* **3**, 061003 (2010).

10) Y. Enya, Y. Yoshizumi, T. Kyono, K. Akita, M. Ueno, M. Adachi, T. Sumitomo, S. Tokuyama, T. Ikegami, K. Katayama, and T. Nakamura, *Appl. Phys. Exp.* **2**, 082101 (2009).

11) M. Adachi, Y. Yoshizumi, Y. Enya, T. Kyono, T. Sumitomo, S. Tokuyama, S. Takagi, K. Sumiyoshi, N. Saga, T. Ikegami, M. Ueno, K. Katayama, and T. Nakamura, *Appl. Phys. Exp*. **3**, 121001 (2010).

12) M. Funato, A. Kaneta, Y. Kawakami, Y. Enya, K. Nishizuka, M. Ueno, and T. Nakamura, *Appl. Phys. Exp.* **3**, 021002 (2010).

13) M. R. Krames, O. B. Shchekin, R. Mueller-Mach, G. O. Mueller, L. Zhou, G. Harber, and M. G. Craford, *J. Disiplay Technol.* **3**, 160 (2007).

14) K. Kojima, M. Funato, Y. Kawakami, S. Nagahama, T. Mukai, H. Braun, and U. T. Schwarz, *Appl. Phys. Lett.* **89**, 241127 (2006).

15) K. Kojima, U. T. Schwarz, M. Funato, Y. Kawakami, S. Nagahama, and T. Mukai, *Optics Exp.* **15**, 7730 (2007).

16) T. Lermer, A. Gomez-Iglesias, M. Sabathil, J. Müller, S. Lutgen, U. Strauss, B. Pasenow, J. Hader, J. V. Moloney, S. W. Koch, W. Scheibenzuber, and U. T. Schwarz, *Appl. Phys. Lett.* **98**, 021115 (2011).

17) B. W. Hakki and Paoli, *J. Appl. Phys.* **44**, 4113 (1973).

18) B. W. Hakki and Paoli, *J. Appl. Phys.* **46**, 1299 (1975).

19) J. Hader, J. V. Moloney, and S. W. Koch, *Appl. Phys. Lett.* **96**, 221106 (2010).

20) E_{pz} was calculated by the method described in Chap. 2. The positive sign represents vectors toward the growth direction.

21) D. Ahn and S. L. Chuang, *IEEE J. Quantum Elec.* **30**, 350 (1994).

22) M. Funato and Y. Kawakami, *MRS Bull.* **34**, 334 (2009).

Chapter 7.

General Summary

7.1 Introduction

This thesis is focused on the optical properties of green laser diodes. To achieve higher performance for green LDs it is necessary to overcome some physical obstacles. Many research groups are competing to fabricate higher performance green LDs and excellent results are regularly obtained. Two techniques are commonly used to fabricate green LDs; one involves growing the device on polar (0001) planes and the other involves growing it on the semipolar planes. In this thesis, optical properties including gain of fabricated green LDs and QWs are discussed.

7.2 Summary of each chapter

7.2.1 Summary of chapter 2

Theoretical understandings is preceded for the physical limitations of III-nitrides light emitters such as internal electric field and inhomogeneity, and then gain formation including effects of material parameters is explained in chapter 2. There are several factors contributing to optical gain such as transition dipole moment, square of overlap integral, effective mass and line width function. Dipole transition moment is particularly important in semipolar or nonpolar systems due to their anisotropic characteristics of valence band. The square of the overlap integral is related to the tilted crystal angle, and semipolar or nonpolar systems can have larger values of the overlap integral. Further, the effective mass for semipolar/nonpolar

systems is lighter than that of the polar (0001) due to their small DOS. This is conductive to population inversion.

7.2.2 Summary of chapter 3

In chapter 3, nanoscopic PL mapping results of LD structure sample are compared with conventional green emitting QW grown on ELOG template for polar (0001) system. The green LD structure shows improved in-plane uniformity and has small wavelength distribution of ~2nm, while the conventional green QW has a wavelength distribution of more than 20 nm. Furthermore, the intensity distribution in the green LD structure is also superior to the conventional green QW. Further, the calculated and measured value of σ (=25 meV) supports the case for homogeneity, since the conventional QW have σ=180 meV. The overlap integral of the green LDs is 2.1 times that of the conventional QW, as confirmed by carrier lifetimes measured by time resolved PL. Polar (0001) green LDs have the advantage of thinner InGaN well layer, which drastically improves the homogeneity of the InGaN layer. However, this leads to an increase in the internal electric field. Therefore, a trade-off between electric field and inhomogeneous broadening is necessary.

7.2.3 Summary of chapter 4

In chapter 4, results of the optical gain measurements are discussed. Internal loss of the green LD on the polar (0001) plane is estimated to be ~10 cm^{-1}, which is much lower in comparison with conventional shorter wavelength LDs with a typical internal loss of ~25cm^{-1}. However, even though the internal loss is low, the differential gain of the LD is lower than the shorter wavelength LDs. There are two possible reasons for the low differential gain. First is the limited net volume of the InGaN well layer, since the well layer gets slightly thinner for better in-plane homogeneity. The second reason is the difficulty in obtaining the difference in refractive indices between InGaN guiding and AlGaN cladding layer. Consequently, the confinement factor of the green laser diode becomes smaller.

7.2.4 Summary of chapter 5

Chapter 5, reports the results of nanoscopic PL mapping by scanning near field optical microscope (SNOM) for a semipolar $\{20\bar{2}1\}$ green LD structure sample. The spatial resolution was as high as 150 nm, corresponding to the diameter of double tapered fiber. Thus, the fine structure of the active layer of LD was well resolved. Comparison between SNOM-PL mapping and AFM measurement, allowed us to investigate the different luminescence properties along each orientation of $[\bar{1}014]$ and $[\bar{1}2\bar{1}0]$, as there exists a strong relation between luminescence and morphology. More uniform luminescence was confirmed by the SNOM-PL result along $[\bar{1}2\bar{1}0]$ than along $[\bar{1}014]$ orientation. Diffusion lengths along each orientation were also obtained by comparison between I-C and I mode measurements. The wavelength differences were analyzed by comparing AFM images. Off angles near c- and m-plane showed different In incorporation yield and so their distributions were found to be different.

7.2.5 Summary of chapter 6

In chapter 6, the results of the optical gain measurement are discussed. The internal loss of green LD on semipolar $\{20\bar{2}1\}$ plane was estimated to be ~20±5 cm^{-1}, which is comparable to loss of ~25 cm^{-1}. Green LD on $\{20\bar{2}1\}$ plane shows gain suppression phenomenon similar to 440 and 470 nm LDs on (0001) plane. However, inhomogeneous broadening of the green LD is ~20 meV, the gain suppression mechanism is suspected to be different from LDs on (0001) plane. Current injection is also an important issue in both of LEDs and LDs. Comparison between calculation and measured results of EL and gain peak are reasonably explained by QCSE due to the *pn* built-in potential, state filling, and screening of polarization-induced electric fields.

Recent results obtained under CW current injection are reported. The signal to noise ratio was improved and internal loss decreased as compared to pulsed operation with ~20cm^{-1}.

7.3 Future prospective of green laser diodes

7.3.1 Green LDs on polar (0001) plane

As described in Chapter 4, a problem with green LDs on polar (0001) plane is that the differential gain is relatively smaller than shorter wavelength LDs. Two reasons for this are the reduced net volume of active layers and the smaller confinement factor in green spectral region owing to the difficulty in obtaining the difference in refractive indices between InGaN guiding layer and AlGaN cladding layer. The former one is due to the optimization of high quality epitaxial layer such that there is a trade-off between in-plane homogeneity and critical thickness of the InGaN well layers. As the In composition increases, the critical thickness decreases. Thus, there appears to be a limitation on InGaN well thickness in polar (0001) system. The latter issue of obtaining the difference in refractive indices is related to the nature of light. This is an issue not only for polar (0001) system but also for different crystal angles such as several semipolar planes. Nonetheless, it seems more difficult to make excellent performance green LDs on polar (0001) plane.

7.3.2 Green LDs on semipolar plane

As detailed in Chapter 2, semipolar green LDs have several merits such as transition dipole moment, square of the overlap integral, and effective mass near the topmost valence band. However, extensive research on semipolar plane LDs is not feasible due to rareness of high quality freestanding GaN substrate. Therefore, several research groups are limited in their work. Moreover, as the crystal angle varies, the material parameters are changed. To fabricate good performance green LDs, accurate information about the changes in these parameters is required. This information can be obtained if the availability of high quality freestanding GaN substrate can be increased. Increased availability will also allow more researchers to contribute to the fabrication of high performance semipolar InGaN green LDs.

Table 7.1 Comparison of representative properties with respect to crystal orientation for green LDs

	GaN Substrate	Growth	Potential Inhomogeneity	Optical Anisotropy	Operating carrier density	Internal Electric field	Internal loss	Max. gain increase as a function of carrier density
Polar (0001)	reasonable	well established	large → small (improving) 470LD: 180 meV (2006) 512LD: 25 meV (2009)	random	2 times higher than {20-21} device	Strong < -2MV/cm	10/cm (even smaller than shorter λ LDs)	High linearity
Semipolar {20-21}	pretty expensive size limitation	established	small 20 meV in {20-21}	Nearly linear polarization		Weak +0.77 MV/cm	~ 20/cm (improving)	High linearity

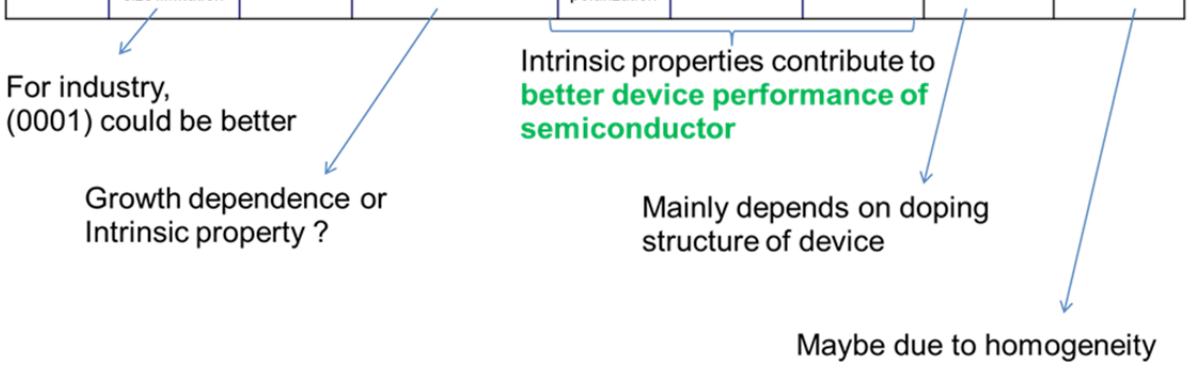

Acknowledgements

I would like to express my sincere gratitude to Professor Yoichi Kawakami for his excellent supervision, continuous guidance, and encouragement. He has advised me extensively throughout this research and on private matters. He has become my ultimate role model for my life.

I would like to thank Professor Shizuo Fujita for his kind encouragement during the discussion and defense of thesis. I acknowledge Associate Professor Jun Suda for his particular concern regarding the theme of my thesis. He gave me many suggestions for my doctoral thesis work through his vast professional insight.

I would also like to thank Associate Professor Mitsuru Funato for his delicate guidance during my research and study in Japan. His insight into our research field is always a step ahead than anyone else. I deeply express my respect to him. I was lucky to be supervised by Assistant Professor Akio Kaneta during the course of my Ph. D. Through these five years, professor Kaneta has offered comfort and extensive knowledge. I would like to express my deep gratitude to him for this.

As a professor in our department and senior alumni of Kawakami laboratory, associate Professor Kazunobu Kojima, has provided me advice, encouragement, and warm humor. Just gratitude would not suffice, so I wish to express my sincere respect towards Prof. Kojima.

I would like to thank all the former and current Kawakami laboratory members. Associate Professor Koichi Okamoto currently enrolled in Kyushu University gave me many hint during his stay here in Kyoto. Associate Professor Ruggero Michelleto of Yokohama City University always made me feel comfortable in this foreign country. I sincerely appreciate his warm heart.

Sumitomo Electric Industries offered me valuable samples based on semipolar GaN such as prototype green laser diodes developed for the first time in the world. Hereby, I would like to express sincere gratitude to Mr. Takao Nakamura, Mr. Masaki Ueno, and Mr. Takashi Kyono.

Nichia Corporation also offered valuable devices for my experiment. For this I express sincere gratitude to Mr. Takashi Miyoshi and Mr. Shin-ichi Nagahama.

Dr. Richard Bardoux and Dr. Ryan Ganipan Banal have been with me at Kyoto University for a long time. I cherish memories of the times spent with them. I appreciate their friendship and consideration.

Dr. Ryota Ishii spent five years of his graduate course with me. I am lucky to meet someone who is highly talented in his field. I am both happy and grateful on receiving my Ph.D degree. I appreciate the cooperation and encouragement of the current Ph.D candidates, Mr. Pedro Favuzzi, Mr. Junichi Nishinaka, Mr. Takao Oto, Miss Pei-tsen Wu, and Mr. Yoshiya Iwata.

Mr. Ken Kataoka has joined as Ph.D candidate during his company. I feel he is preparing for higher goals in life. I hope his Ph.D is completed soon.

I do not know how to express my gratitude for Mrs. Miki Watanabe; words would not suffice. My life in Japan, from alpha to omega, was possible due to her devotion and concern. Thank you very much Ms. Watanabe.

Owing to limited space, I cannot name everyone; however, I am grateful to all the members of the laboratory. Thank you very much for your cooperation and friendship.

I required substantial help regarding financial support and preparation after graduation for my study in Japan. Dr Jong Hyoub Baek of KOPTI has offered me an opportunity for settlement after graduation.

My study in Japan would not have been possible without the emotional and financial support of my brother and my mother. They have been my emotional shelter and support. Thank you and lot of love to you both.

When I joined Kyoto University I was alone, but my wife came to me so I could bear living in a foreign country. Thank you and love you, sweetheart. I am greatly thankful for the birth and existence of my lovely children, Kyu Min and Ji Yu! . I love you so much.

Lastly, I appreciate the support of my parents-in-law. Thank you.

February, 2014 in Kyoto University
Yoon Seok Kim

List of Publications

A. Scientific Articles

1. Yoon Seok Kim, Akio Kaneta, Mitsuru Funato, Yoichi Kawakami, Takachi Kyono, Masaki Ueno, and Takao Nakamura, "Optical Gain Spectroscopy of A Semipolar $\{20\bar{2}1\}$ oriented green laser diode", *Applied Physics Express*, **4**, 052103 (2011).
2. Akio Kaneta, Yoon Seok Kim, Mitsuru Funato, Yoichi Kawakami, Yohei Enya, Takashi Kyono, Masaki Ueno, Takao Nakamura, "Nanoscopic PL properties of a green emitting InGaN single quantum well on $\{20\bar{2}1\}$ GaN substrate probed by scanning near field optical microscopy", *Applied Physics Express*, **5**, 102104 (2012).
3. Mitsuru Funato, Yoon Seok Kim, Takayuki Hira, Akio Kaneta, Yoichi Kawakami, Takashi Miyoshi, Shin-ichi Nagahama, "Remarkably Suppressed Luminescence Inhomogeneity in a (0001) InGaN Green Laser Structure", *Applied Physics Express*, **6**, 111002 (2013).
4. Mitsuru Funato, Yoon Seok Kim, Yoshiaki Oichi, Akio Kaneta, Yoichi Kawakami, Takashi Miyoshi, Shin-ichi Nagahama, "Optical Gain Specra of a (0001) InGaN Green Laser Diode", *Applied Physics Express*, **6***,* 122704 (2013).

B. Proceedings

1. Yoon Seok Kim, Akio Kaneta, Mitsuru Funato, Yoichi Kawakami, Takachi Kyono, Masaki Ueno, and Takao Nakamura, "Optical gain spectra in semipolar $\{20\bar{2}1\}$ oriented green LDs in comparison with (0001) LDs", 電気情報通信学会 IEICE Technical Report, LQE2011-115, p99-102.
2. Yoon Seok Kim, Akio Kaneta, Mitsuru Funato, Yoichi Kawakami, Takashi Miyoshi, Shin-ichi Nagahama, "Contribution of low inhomogeneous broadening and well layer thickness to the optical gain of a (0001) oriented InGaN-based green laser diode", 電気情報通信学会 IEICE Technical Report, LQE2012-109, pp.71-74.

Conferences Attended

A. International Conferences

1. Yoon Seok Kim, Akio Kaneta, Mitsuru Funato, Yoichi Kawakami, Takashi Miyoshi, Shin-ichi Nagahama, "Optical gain properties of (0001) oriented InGaN-based green laser diodes with low threshold current density", ICMOVPE-XVI, May 2012, Busan Korea, Oral Presentation TuB3-5 as Late News.
2. Akio Kaneta, Yoon Seok Kim, Mitsuru Funato, Yoichi Kawakami, Yohei Enya, Takashi Kyono, Masaki Ueno, Takao Nakamura, "Nanoscopic PL properties in green emitting InGaN single quantum well on $\{20\bar{2}1\}$ GaN substrate probed by scanning near field optical microscopy", International Workshop on Nitride semiconductor 2012, J1-5, Sapporo, Japan, October 14-19, 2012.
3. Akio Kaneta, Takayuki Hira, Yoon Seok Kim, Mitsuru Funato, Yoichi Kawakami, Takashi Miyoshi, Shin-ichi Nagahama, "Local photoluminescence properties of InGaN green laser structure on (0001) GaN substrate"' CLEO-PR2013, WH3-2, Kyoto Japan, Oral Presentation. **Awarded Best Paper**.

B. Local conferences

1. Yoon Seok Kim, Akio Kaneta, Mitsuru Funato, Yoichi Kawakami, Takachi Kyono, Masaki Ueno, and Takao Nakamura, "Optical gain spectra in semipolar $\{20\bar{2}1\}$ oriented green LDs in comparison with (0001) LDs", 30th Electronic Materials Symposium, Laforet Biwako Siga, We1-15 (2 min. oral + Poster).
2. Yoon Seok Kim, Akio Kaneta, Mitsuru Funato, Yoichi Kawakami, Takachi Kyono, Masaki Ueno, and Takao Nakamura, "Optical gain spectra in semipolar $\{20\bar{2}1\}$ oriented green LDs in comparison with (0001) LDs", 電気情報通信学会 Laser and Quantum Electronics (LQE), November 17-18, 2011, Katsura Hall Kyoto university, LQE2011-115, pp.99-102.
3. Yoon Seok Kim, Akio Kaneta, Mitsuru Funato, Yoichi Kawakami, Takashi Miyoshi, Shin-ichi Nagahama, "Contribution of low inhomogeneous broadening to the optical gain of a (0001) oriented InGaN-based green laser diode", the 73th Fall meeting: Applied Physics Conference, 12p-H10-12, September 10-14, 2012, Eihime University, Japan (oral presentation).

4. 金田昭男、金潤碩、船戸　充、川上養一、塩谷陽平、京野孝史、上野昌紀、中村孝夫, “緑色発光{20$\bar{2}$1} GaN 基板上 InGaN 量子井戸の近接場顕微発光測定, the 73th Fall meeting: Applied Physics Conference, 12p-H10-12September 10-14, 2012, Eihime University, Japan (oral presentation).
5. Yoon Seok Kim, Akio Kaneta, Mitsuru Funato, Yoichi Kawakami, Takashi Miyoshi, Shin-ichi Nagahama, “Contribution of low inhomogeneous broadening and well layer thickness to the optical gain of a (0001) oriented InGaN-based green laser diode”, 電気情報通信学会　Laser and Quantum Electronics (LQE), November 29-30, 2012, Osaka City University.